AD-A285 928

ASC--TR--94-5027

# OPEN SKIES PROJECT COMPUTATIONAL FLUID DYNAMIC ANALYSIS

JAMES C. SLAVEY
MARK S. JURKOVICH
ROBERT M. WEYER
JOSEPH C. ZUPPARDO

Flight Technology Branch
Flight Systems Engineering Division
Integrated Engineering and Technical Management Directorate
Aeronautical Systems Center
Air Force Materiel Command
Wright-Patterson Air Force Base, OH 45433-7126

MARCH 1994

Final Report for Period 16 November 1992 to 20 May 1993
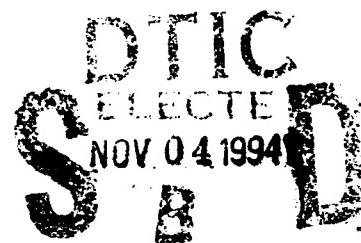
94-34310

Experimental Flight Test Division
4950th Test Wing and Modification Facility
Air Force Materiel Command
Wright-Patterson Air Force Base, OH 45433-7126
United States Air Force

NOTICE

When Government drawings, specifications, or other data are used for any purpose other than in connection with a definitely Government-related procurement, the United States Government incurs no responsibility or any obligation whatsoever. The fact that the government may have formulated or in any way supplied the said drawings, specifications, or other data, is not to be regarded by implication, or otherwise in any manner construed, as licensing the holder, or any other person or corporation; or as conveying any rights or permission to manufacture, use, or sell any patented invention that may in any way be related thereto.

This report is releasable to the National Technical Information Service (NTIS). At NTIS, it will be available to the general public, including foreign nations.

This technical report has been reviewed and is approved for publication.
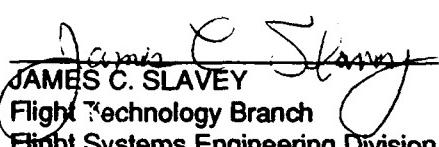
JAMES C. SLAVEY
Flight Technology Branch
Flight Systems Engineering Division

MARK S. JURKOVICH
Flight Technology Branch
Flight Systems Engineering Division

ROBERT M. WEYER
Flight Technology Branch
Flight Systems Engineering Division

JOSEPH C. ZUPPARDO
Flight Technology Branch
Flight Systems Engineering Division

TIMOTHY P. SWEENEY, Chief
Flight Technology Branch
Flight Systems Engineering Division

WILLIAM F. IMFLED, GM-15
Chief, Flight Systems Engineering Division
Integrated Engineering and
Technical Management

DISCLAIMER NOTICE
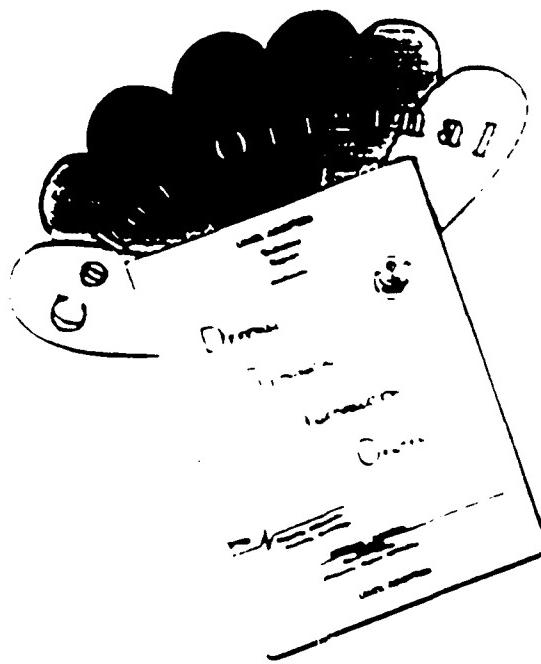
THIS DOCUMENT IS BEST QUALITY AVAILABLE. THE COPY FURNISHED TO DTIC CONTAINED A SIGNIFICANT NUMBER OF COLOR PAGES WHICH DO NOT REPRODUCE LEGIBLY ON BLACK AND WHITE MICROFICHE.

REPORT DOCUMENTATION PAGE

Form Approved
OMB No. 0704-0188

1. AGENCY USE ONLY (Leave blank)	2. REPORT DATE Mar 94	3. REPORT TYPE AND DATES COVERED Final November 1992-May 1993

4. TITLE AND SUBTITLE

Open Skies Project Computational F   Dynamic Analysis

5. FUNDING NUMBERS

6. AUTHOR(S)

James C. Slavey, Mark S. Jurkovich,
Robert M. Weyer, Joseph C. Zuppardo

7. PERFORMING ORGANIZATION NAME(S) AND ADDRESS(ES)

ASC/ENFT (Flight Technology Branch)
Flight Systems Engineering Division
Integrated Engineering and
Technical Management
Wright-Patterson AFB OH 45433-7809

8. PERFORMING ORGANIZATION REPORT NUMBER

9. SPONSORING/MONITORING AGENCY NAME(S) AND ADDRESS(ES)

Experimental Flight Test Division
4950 Test Wing and Modification Facility
Aeronautical Systems Center
Air Force Materiel Command
USAF, Wright-Patterson AFB OH 45433-5111

10. SPONSORING/MONITORING AGENCY REPORT NUMBER

ASC-TR-94-5027

11. SUPPLEMENTARY NOTES

12a. DISTRIBUTION/AVAILABILITY STATEMENT

Approved for Public Release; distribution is unlimited

12b. DISTRIBUTION CODE

13. ABSTRACT (Maximum 200 words)

A Computational Fluid Dynamic (CFD) analysis has been performed on a WC-135B aircraft that has been modified at Wright-Patterson AFB (WPAFB) forming the first Open Skies aircraft designated OC-135B. The studies included the use of panel method, full potential, and Navier-Stokes methods utilizing 2-D/axisymmetric, and 3-D. While providing information useful to the Open Skies program, the studies also provide a good example of how lower order and higher order computational aerodynamic methods can be used together to obtain the maximum benefit from CFD at a minimum cost. Flight test tufting and accelerometer data confirmed the results of the 3-D Full Navier-Stokes results.

14. SUBJECT TERMS

Aerodynamic Analysis	Open Skies Aircraft
Computational Fluid Dynamics	Flight Test Production
Turbulence Modeling	

15. NUMBER OF PAGES
120

16. PRICE CODE

17. SECURITY CLASSIFICATION OF REPORT UNCLASSIFIED	18. SECURITY CLASSIFICATION OF THIS PAGE UNCLASSIFIED	19. SECURITY CLASSIFICATION OF ABSTRACT UNCLASSIFIED	20. LIMITATION OF ABSTRACT

TABLE OF CONTENTS

LIST OF FIGURES

LIST OF TABLES

ACKNOWLEDGMENTS

LIST OF SYMBOLS

C_f	Skin friction coefficient
C_L	Lift coefficient
C_p	Pressure coefficients, or specific heat at constant pressure
$\hat{C}_p$	Instantaneous pressure coefficient (Appendix B only)
$C_{p''}$	Pressure fluctuation coefficient
E	Total internal energy
$\mathcal{f}$	Driest's factor
H	Boundary layer shape factor
I	First grid index
J	Second grid index
K	Third grid index
K	Specific turbulent kinetic energy (Figure 66 only)
M	Mach number
N	Amplification ratio exponent
Re or Rn	Reynolds number (Rn used in figures only)
Re_k	Reynolds number based on sand grain roughness
Re_t	Turbulent Reynolds number
Re_x	Reynolds number at station x
Re_{xtr}	Transition Reynolds number
Re_θ	Momentum boundary layer height Reynolds number
R_q	y^+ derived Reynolds number (q is a function of y^+)
R_{y^+}	Reynolds number based on y^+
T	Temperature, or Turbulent intensity
T''	Mass averaged temperature fluctuation
V	Velocity
V''	Mass averaged velocity fluctuation
k	Specific turbulent kinetic energy
k	Equivalent sand grain roughness
k_{tr}	Equivalent sand grain roughness value at transition
p	Pressure
q	Dynamic pressure
s	Relative specific entropy
u	Boundary layer edge velocity
y^+	Boundary layer height, dimensionless parameter
α	Angle of attack
γ	Ratio of specific heats
ε	Turbulent dissipation rate
ρ	Density
μ_t	Turbulent viscosity
μ	Molecular viscosity
ν	Kinematic viscosity

LIST OF ABBREVIATIONS/ACRONYMS

2-D	Two-Dimensional
3-D	Three-Dimensional
AOA	Angle of Attack
B-L	Baldwin-Lomax
CAD	Computer Aided Design
CFD	Computational Fluid Dynamics
CFL	Courant-Friedrichs-Lewy
EN	Integrated Engineering and Technical Mangement Directorate
ENFT	Flight Technology Branch
ENFTA	Aerodynamics and Performance Section
FNS	Full Navier-Stokes
GASP	General Aerodynamic Simulation Program
IBL	Iterative Boundary Layer
KAFB	Kirtland Air Force Base
NASTD	NAvier-Stokes Time Dependent program
PNS	Parabolized Navier-Stokes
SGI	Silicon Graphics Inc.
SLNS	Slender-Layer Navier-Stokes
TESTW/FFX	4950th Test Wing's Experimental Flight Test Division
TFI	TransFinite Interpolation
TLNS	Thin-Layer Navier-Stokes
WB	Wing-Body
WL	Wright Laboratory
WPAFB	Wright-Patterson Air Force Base

1. INTRODUCTION

One of the benefits, and challenges, of the subsequent warming of East/West relations that came with the breakup of the former Soviet Union has been the opening of airways over formerly restricted territory. The changing political environment precipitated the signing of the Open Skies treaty. The treaty, signed by 25 NATO and former Soviet bloc countries in March 1992, enables unarmed observation aircraft from one country to fly over another. In response to this treaty, a WC-135B aircraft has recently undergone modifications at the 4950th Test Wing Aircraft Modification Facility at WPAFB. In particular, modifications have been made to what was the refueling boom operator's pod on a former KC-135 to accommodate look-down cameras, thus forming the first Open Skies aircraft, the OC-135B. Panel methods, full potential, and Navier-Stokes analyses were performed to assess the aerodynamic impacts of the Open Skies modifications.

The analyses of the modification arose when Mr Larry A. Roberts, of the 4950th Test Wing's Experimental Flight Test Division (TESTW/FFX), took an action item from Colonel Tipton, Director of the Modification Facility, during the Open Skies Configuration Control Board. This action item was to address the concerns of any potential problems that might result from flow separation around the modification. Specific concerns included: vibration that could affect the camera image-quality, skin fatigue downstream of separation caused by buffeting and acoustic noise, and pressure fluctuations or shocks that could create significant optical diffractions. The analysis was to be performed only at the "worst case flight-condition" to keep down costs.

Specific tools used are noted as follows: Analytical Methods Inc.'s **VSAERO** (version E.4) panel code run on Silicon Graphics Inc. (SGI) workstations; the Boeing/NASA Ames **TRANAIR** (version 2.0) full potential solver run on the WPAFB Cray **XMP2/16**; the General Aerodynamic Simulation Program (**GASP**) version 2.2 Full Navier-Stokes (FNS) code obtained from AeroSoft, run on the Kirtland Air Force Base (KAFB) **Cray II**; the NAvier-Stokes Time Dependent (**NASTD**) FNS program (version 14.51) received from McDonnell-Douglas, run on the WPAFB Cray

XMP2/16; NASTD version 15.96 run on the Aerodynamics and Performance Section (ASC/ENFTA) SGI **Crimson50**.

The grid generation, transition prediction, and coarse resolution three-dimensional (3-D) **GASP** analyses were performed by Mr James C. Slavey. The axisymmetric and fine resolution 3-D **NASTD** Navier-Stokes analyses, and turbulence model selection were accomplished by J. Slavey and Mr Robert M. Weyer. All **VSAERO** panel code analyses were executed by Mr Mark S. Jurkovich. The **TRANAIR** full potential code analysis was conducted by Mr Joseph C. Zuppardo.

2. MODELING OF THE MODIFICATION

The modification investigated in this study involves cutting off a portion of the bottom part of the WC-135B boom pod and installing a flat surface with two observation windows for the camera mountings (Figures 1 & 2). Figure 3 illustrates a centerline cut of the modification. Note that the windows are recessed, the front window by 0.6" (15.mm) and the aft window by 0.7" (18.mm). They were not made flush to avoid added cost. The window recesses were included in all the Navier-Stokes runs, but were left out of the panel method and full potential runs. The axisymmetric and two-dimensional (2-D) grids were generated off the vehicle lower centerline geometry (nose to tail). The axisymmetric grid was simply the 2-D grid rotated 10 deg. from the symmetry plane. The window indentations were modeled for the coarse 2-D and axisymmetric grids, but the corners were not modeled because the grid resolution was too coarse to capture those details. The corners were approximately 60 deg. for the fine axisymmetric grid partly because of streamwise grid resolution, and because preliminary designs included aero-sealant in the corners. The final design did not include aero-sealant in the corners, therefore 90 deg. was used in the fine 3-D grid. In the coarse 3-D grid, the panel density in the modification region was about 8" x 8" (0.203m square), which didn't permit precise modeling of the corners, but the affected points were indented. Only the two fine grids have the actual window recess heights, because both windows were originally designed to be set 0.75" (19.mm) deep into the modified surface.

One key feature that further complicated the design problem is the presence of a bulkhead that extends below the flat plate at the back end (Station 1319, Figure 3). Because of time and cost constraints, cutting the bulkhead was reserved as a solution, if absolutely necessary. Aerodynamic sealant was used to fair in the protruding bulkhead as smooth as possible. As will be shown, this bump is the source of rapid flow changes resulting in recirculation behind the plate.

In addition, a drain mast is located to the side of the bulkhead. It protrudes a half foot (0.152m), and is located 16" (0.406m) to the left of the centerline near the bulkhead station. The mast is 13" (0.330m) long at the base and 15" (0.381m) long at the tip. It has sharp edges and

3
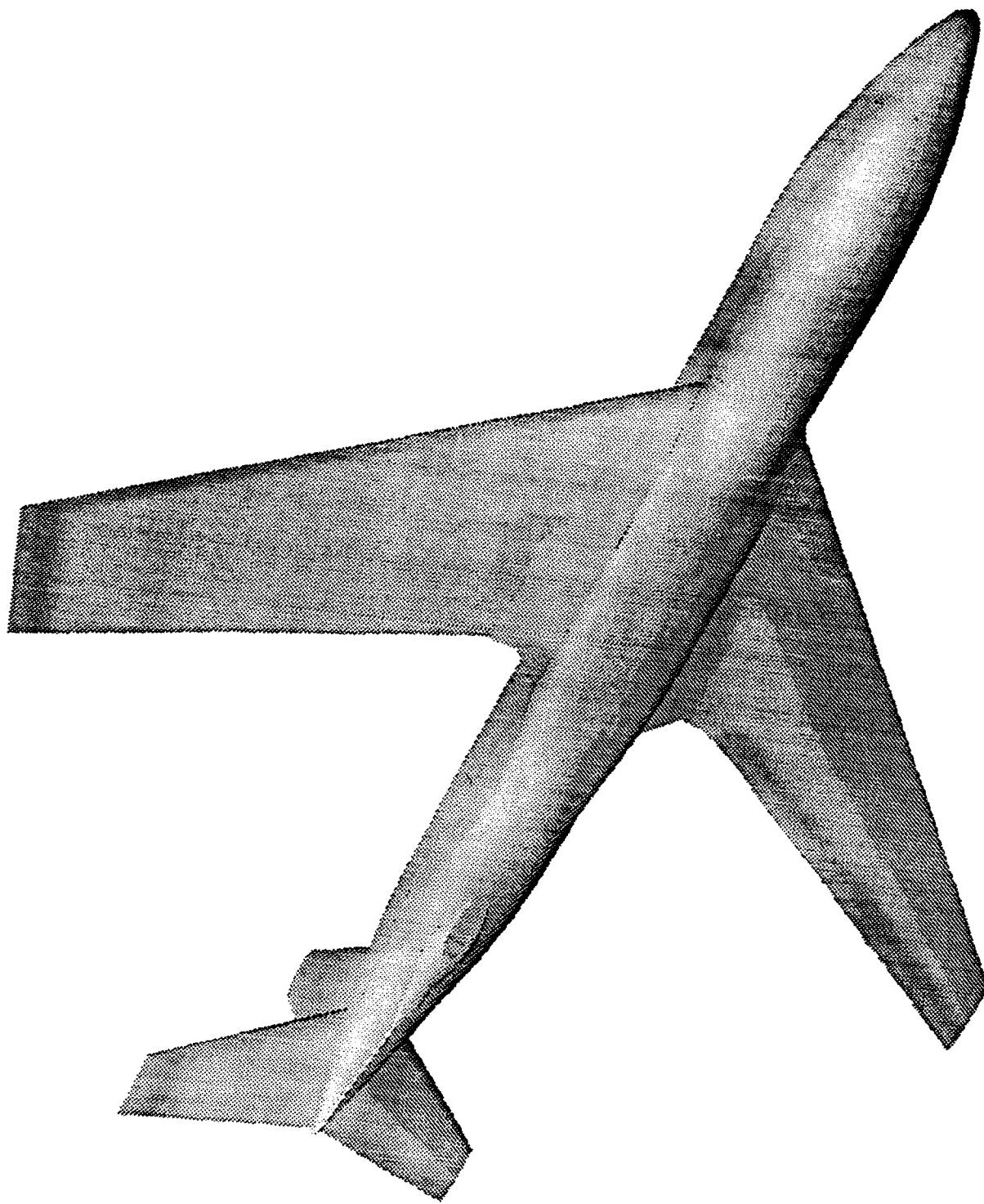
Figure 1: Model of OC-135 with Open Skies Modification

4

Figure 2: Close-up of Open Skies Pod Showing Windows

5
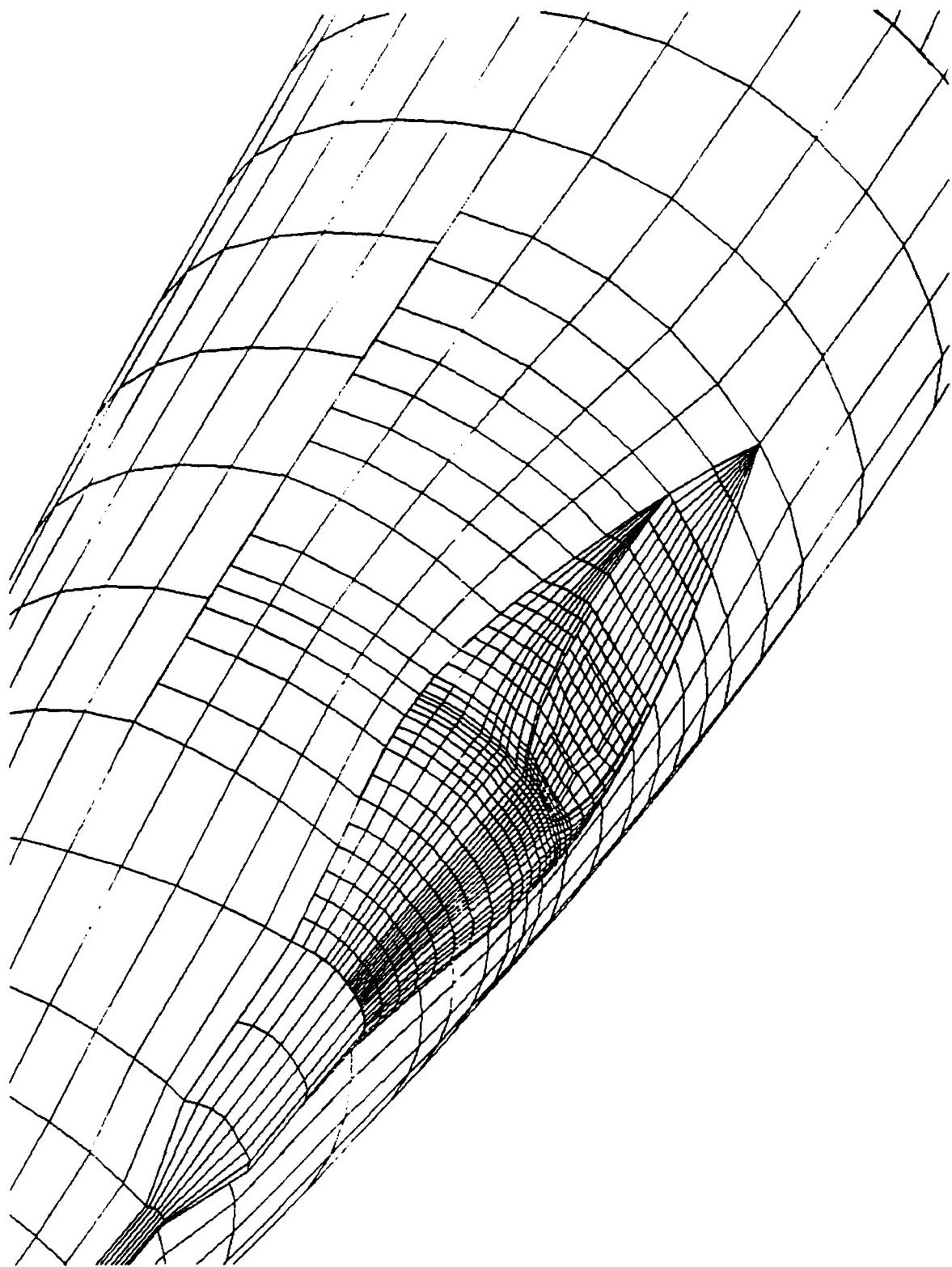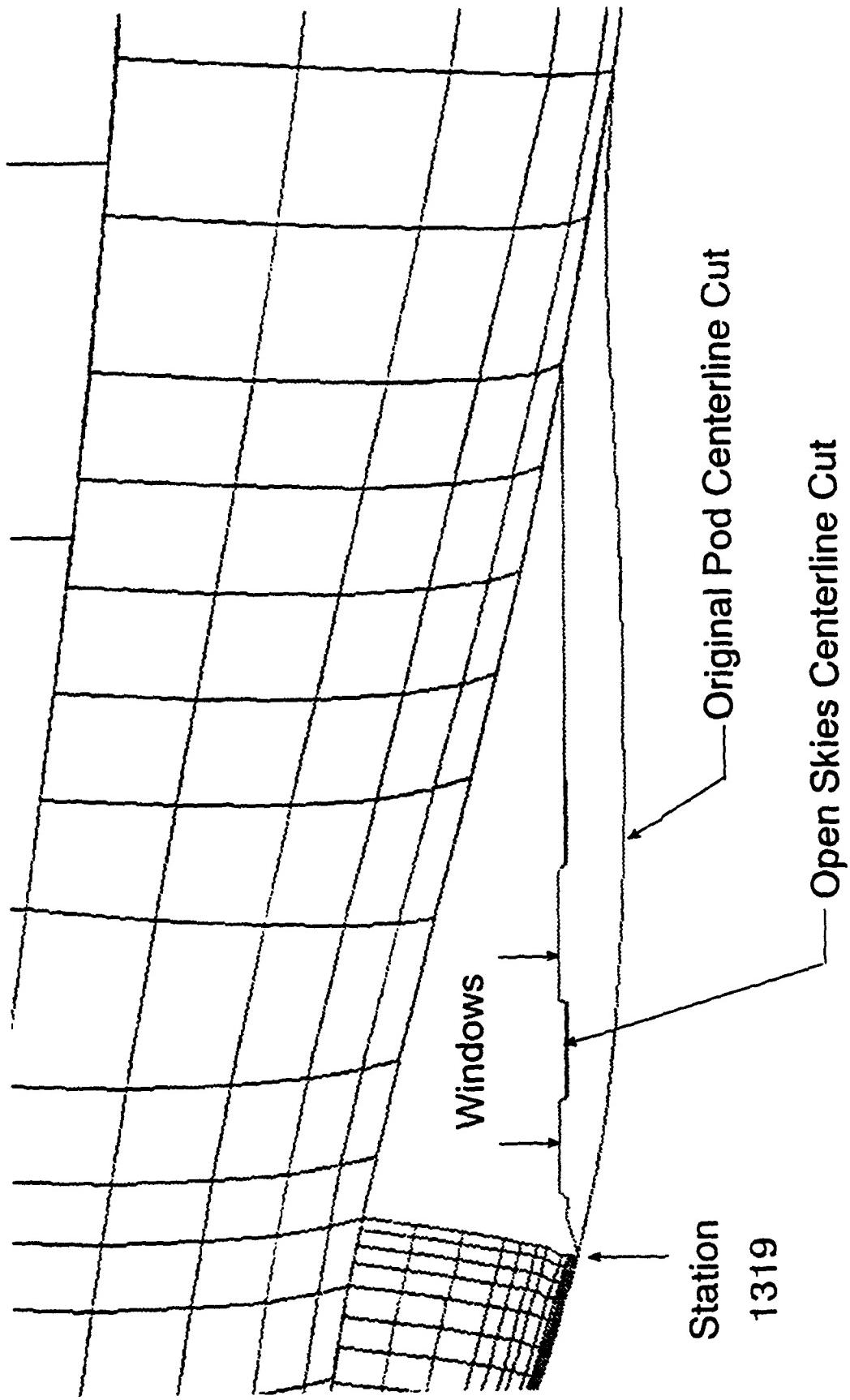
Figure 3: Centerline Profiles of Original WC-135 Pod and Open Skies Modification

6

irregular welding. It was not modeled because it was thought to have small influence on the area of interest. Its inclusion would have also precluded the use of symmetry and doubled the computational cost.

The initial geometry from the Modification Facility was a WC-135 panel model. It was compared to and merged with the ENFTA C-135 model for better fidelity. The geometry provided was verified as being representative of a -135B series aircraft (Ref. 1).

3. TECHNICAL APPROACH

It was known that the flowfield about the modification involved a thick turbulent boundary layer, sharp corners (probably causing separated or recirculation flow regions), and possible shock waves. Therefore, it was clear a full 3-D Navier-Stokes Computational Fluid Dynamics (CFD) solution was necessary to predict any potential problems for the modification flight-test program. There was also, however, a severe time constraint of needing answers as soon as possible. To manage this challenge, a multi-path approach was decided upon. A potential flow code would be used to provide early indications of any potential aerodynamic design problems and enable various rapid trade studies, while a full 3-D Navier-Stokes grid was being generated. The panel method selected for the study was **VSAERO** version E.4 (Ref's 2 & 3). This code was chosen because of the added features of being able to perform wake relaxations and iterative boundary layer (IBL) calculations. One of the key trade studies performed with **VSAERO** was to design contour changes behind the flat plate region to minimize the potential for shock formation and/or flow separation. Two candidate configurations were paneled and analyzed. Analyses were also performed with **VSAERO** on the unmodified WC-135B baseline configuration. Finally, the panel code was used to obtain preliminary effects of the wing influence on the pressure field over the modification region by running the configuration with and without a wing.

As another source of providing early indications for potential shocks, runs were also performed using the **TRANAIR** version 2.0 full potential code (Ref's 4 & 5). This code was also used to supplement the wing-body versus body alone trade study performed using **VSAERO**. **TRANAIR** solves the full potential equation subject to a set of general boundary conditions. Therefore, it includes the nonlinearities associated with transonic aerodynamics in its modeling. The boundary value problem is discretized using the finite element method on a locally refined rectangular background grid. The nonlinear discrete system arising from the finite element method is solved using a preconditioned Krylov subspace method embedded in an inexact Newton method (Ref. 4). The solution was obtained on a sequence of successively refined grids that were constructed

adaptively based on estimated solution errors. It should be noted that there was no need to perform an Euler analysis in this multilevel approach, since there is nothing ahead of the modification region that would generate significant vortical effects. The full potential results, therefore, should be identical to any Euler solutions that may be performed.

For lessons learned purposes, the Navier-Stokes approaches that were tried but proved impractical will be included in this discussion. To minimize computational costs and analysis time, the initial objective was to obtain output from the panel code at a station upstream of the pod and use it to define initial conditions for the Navier-Stokes study. However, even though **VSAERO** can calculate boundary layers, it was not designed to provide the fidelity needed for a Navier-Stokes code. Small discontinuities were present in the boundary layer and a slope discontinuity occurred at the edge of the boundary layer. These anomalies were considered too great to be used as input conditions for the Navier-Stokes solutions.

The next approach in the Navier-Stokes study was to run the calculation on either a full wing-body (WB) or body alone geometry with a relatively coarse grid to provide initial conditions for a fine grid on just the region of interest. The coarse body alone grid was generated with relative ease, but it was impossible to develop a good wing-body Navier-Stokes grid within the time available (1 man month). **VSAERO** was, therefore, used to run a quick study on the surface geometries developed for the coarse wing-body and body alone Navier-Stokes cases. As will be discussed later, the results showed little difference in the pressures over the area of interest. It was, therefore, decided the Navier-Stokes runs could be performed without the wing.

The prerelease **GASP** version 2.2 (Refs 6, 7 & 8) was chosen as the primary tool for performing the Navier-Stokes study. The coarse 3-D grid was also run with **NASTD** version 15.96 (Refs 9 & 10) in a parallel approach, since at the time the analysis was initiated some uncertainties existed as to code availability (due to a limited freeware license length), and the affordability of the CRAY II.

Upon completion of the 3-D coarse grid simulations, analyses were performed over 2-D and axisymmetric representations of the aircraft lower centerline using **NASTD** version 14.52, while the

9

3-D fine grid was being developed. Because of the aforementioned concerns with the availability of the **GASP** code, the remaining part of the study had to be completed with the **NASTD** code alone. The final steps consisted of running the fine 3-D grid with **NASTD** and performing an axisymmetric study on the alternate fairing designed to minimize the adverse flowfield behind the bulkhead.

An appropriate flight condition to perform CFD calculations was chosen through the use of an overall flight-condition severity-index which blends the structural loads severity (both static and dynamic), and steady-state aerodynamic severity. Structural load gradients are maximized with Mach number. The dynamic loads are maximized with dynamic pressure (q). The steady-state aerodynamic separation sensitivity to surface angularity scales with Reynolds number (Re). The maximum Re, and maximum q conditions occur at the minimum altitude, which for photography will be either 3000 ft (0.914 km) or 5000 ft (1.524 km). The derived index, however, needed to increase with all three parameters, therefore the product of Mach number, dynamic pressure and Reynolds number was selected as the appropriate weighting (M·q·Re). Emergency operating conditions were used instead of structural limits. According to Ref. 11, the maximum Mach number that will operationally be flown with KC-135s (at the corner of the envelope at 29,500 feet (ft) (8.992 km)) is 0.84, not the structural limit of Mach number 0.90. From calculations with an in-house code, along the high speed border of the Mach-altitude envelope, the worst operational flight-condition lies somewhere between 20,000 ft (6.096 km) and 26,000 ft (7.925 km). By interpolating limit knots indicated air speed (Ref. 12), corrected to knots calibrated air speed, and including a position correction (Ref. 13), conditions were calculated for every thousand foot. The overall worst case calculated in this manner was Mach number 0.8323 at 23,000 ft (7.010 km), which was rounded up to Mach number 0.84. Finally, a cruise angle of attack (AOA) at the above condition was determined. The lift coefficient required for level flight at a nominal weight of 200,000 lb (90700 Kg), 23,000 ft (7.010 km), 0.84 Mach number is: C_L=0.198, which corresponds to an AOA of 1.4 degrees (Ref. 14). It was found after the study that Ref. 14 was really using a wing AOA instead of referencing to a fuselage AOA. Therefore the 3-D simulations were actually performed at 3.4 deg., since the wing incidence is listed as 2 degrees. This corresponds to a climb attitude since straight

and level flight at this altitude requires fuselage reference-line AOAs between -0.6 and 0.0 degrees over the valid ranges for center of gravity and weights. Sideslip was assumed zero to keep the computational costs affordable. The axisymmetric and two-dimensional runs were conducted at an AOA of 2.288 degrees. This is the angle of the panel-model fuselage-axis (from the nose tip through the tail end) relative to the fuselage reference-line. The TRANAIR runs were conducted at an AOA of zero ss.

4. GRID GENERATION

The proposed modifications were blended into the existing panel model from drawings and a finite element file provided by the Test Wing. Care was used to ensure the geometry model was representative of the real vehicle modification lines. This included a few meetings with the Computer Aided Design (CAD) technicians and engineers involved in the project, carefully reviewing the drawings, and viewing the aircraft modification in-progress at the Modification Facility hangar.

The initial panel geometry, including the wing, was re-paneled with I3G/Virgo (Ref. 15) to have one-to-one panel network matching. This was necessary because **GASP** requires one-to-one volume grid blocks. Repaneling was also essential, because the model provided consisted of many small networks of widely varying panel density. Each time a file was written out from Virgo it was run through an in-house code to filter out the truncation and round-off problems inherent with the code; the same was true with the EagleView grid symmetry planes. The paneling definition was smoothed for better volume grid quality.

In preparation for the volume gridding the transition location was determined (see Appendix A). The next step in the grid generation process was the generation of the volume grid around the paneling. An "O-O" topology (Ref. 16), using symmetry in the Y direction, was selected to minimize the number of grid points in order to keep down computational costs. This topology is similar to normal lines radiating out from the fuselage. This part of the project was the most time consuming, as usual. A quick hyperbolic marching off the entire geometry using EagleView (Ref's 17, 18, 19, & 20) proved infeasible due to the wing-body juncture shape. Several other schemes were attempted which proved ineffective. An initial wing-body Navier-Stokes grid was generated using Wright Laboratory's (WL) Poisson solver (Ref. 21), but negative cells detected by the **Qbert** grid quality checker (Ref. 22) were resistant to being smoothed out with a Laplace method. The position, dihedral, and sweep of the wing posed some problems in blending it smoothly with the

nose and tail blocks. Since the schedule of the modification was so aggressive, the wing-body generation was stopped, and alternatives were evaluated.

Wing-body Navier-Stokes grids are being done in industry, but they require a few to a dozen man-months. Complex grids have been performed by ENFTA in the past: the F-15E Seek Eagle wing-body Euler grid, and the YA-7+ forebody and inlet duct FNS grids both required several man-months. The Flight Dynamics Directorate KC-135 wing-body Euler grid also required several man-months to generate. A complete wing-body Navier-Stokes grid has yet to be developed in EN or WL. It is still a very time intensive process even with the latest structured software. At this point, it was decided to perform the Navier-Stokes calculations on a body alone geometry.

Since only exponential and hyperbolic tangential stretchings were available, too many points were being packed near the surface in the preliminary grids to match a $y^+=1$ height, regardless of selected spacing options. The $y^+=1$ height was calculated to be 2.086×10^{-4} in. (5.298×10^{-6} m), based upon a reliable turbulent correlation from Lockheed (Ref. 16). The hyperbolic grid generator (HypGen 1.1 in EagleView2.3) was rapidly enhanced in-house to employ geometric spacing, which enabled generation of suitable modified fuselage grids. This hyperbolic grid generator gives smooth, highly orthogonal grids. The coarse grid was dimensioned 172 in the streamwise direction, 39 in the circumferential, and 69 in the normal direction.

The entire fine grid had an identical topology, and was dimensioned 263 x 51 x 71. The fine grid was broken up into three streamwise sections, then these were broken in half in the normal direction. This enabled the simulation to fit on the WPAFB Cray XMP, as well as increasing the vectorization. The two upstream blocks were not used to save costs, only the aft four equal sized blocks (88 x 51 x 36) were used, using the coarse grid results as an initial condition.

Of the remaining four zones, zone 1 was the inner upstream grid-block and zone 2 was wrapped around zone 1. Zone 3 was the inner downstream grid-block, and zone 4 was around zone 3 (Figure 4). The parameters used in the generation of the fine grid, selected by systematic variation, are as follows: region size 5100" (129.5 m), geometric exponent 1.24, axis boundaries in both J directions,
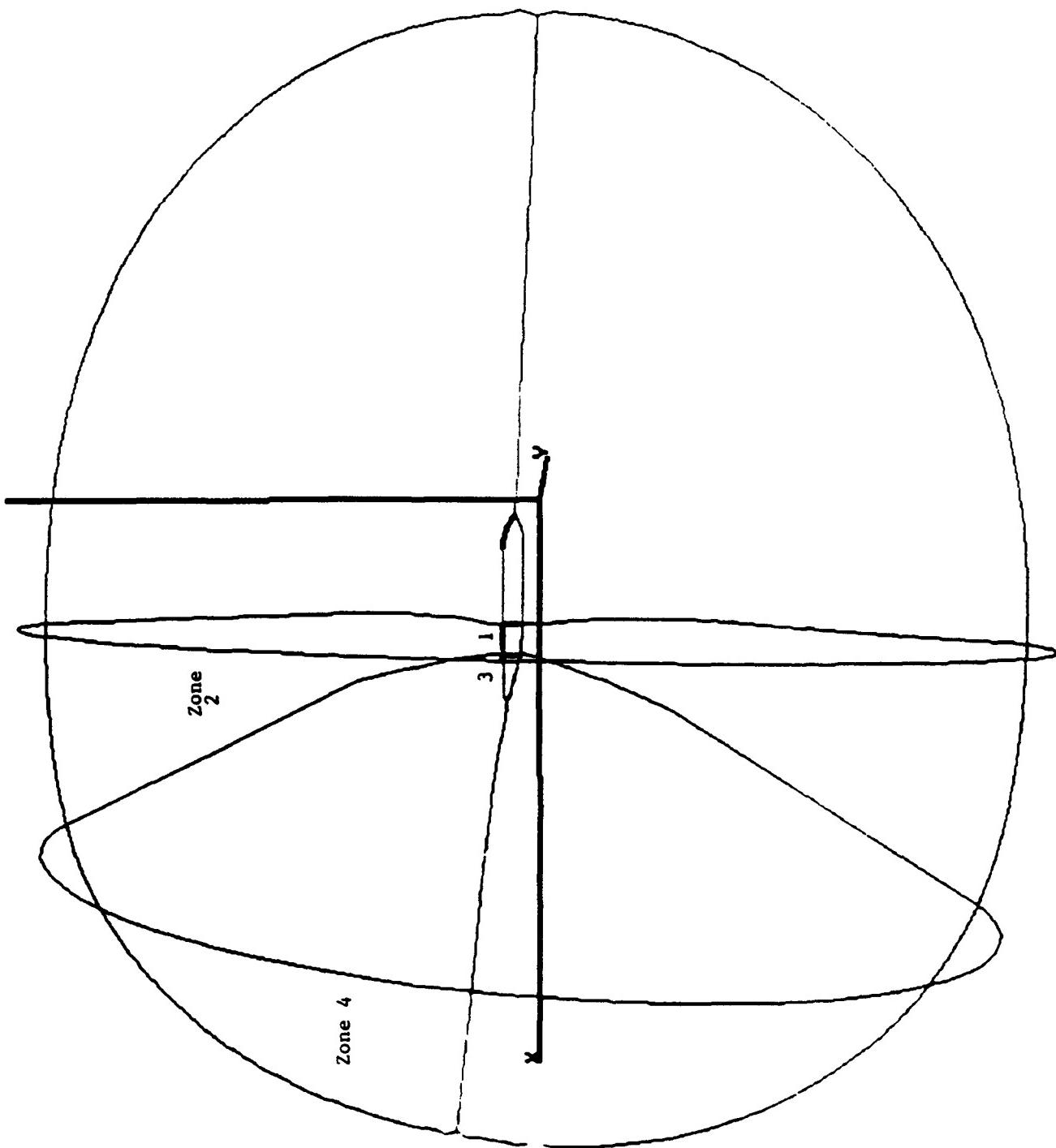
Figure 4: Fine 3-D Grid Zonal Boundaries

Zone 2

Zone 4

14

Y constant boundaries in both K directions, 1500 smoothing iterations, and the other seven parameters were defaulted.

There were a few negative cells indicated in the fine 3-D grid, near the window corners, that the Lockheed TransFinite Interpolation (TFI), and EagleView's TFI could not remove by patching in new grid in the problem areas. A FORTRAN program was written to extract out the boundaries of the crossed grid cells, for diagnostic visualization in Plot3D. Since the problem appeared to be solvable algebraically, an in-house TFI grid generator was rapidly programmed which eliminated the negative cell region indicated in EagleView. Another code was written to patch the correction over the original grid.

A second problem that arose was that the grid would fold in upon itself in EagleView after almost marching out to the desired outer boundary. To address this problem, another in-house grid generator was written to scale the final good grid wrap using geometric spacing. The outer wraps were quickly generated in this manner and appended to the EagleView grid.

As part of the grid generation process, grid quality checkers are used to quantitatively grade the volume grid in terms of anticipated truncation error and resulting accuracy of the solution. The better codes also provide diagnostics to facilitate correcting problem areas in the grid. If necessary, parts of the volume grid would then be regridded until an acceptable grid quality is obtained. When the user is experienced with a "class of geometry," extensive regridding is typically not necessary. For Euler codes a program (such as Qbert) can be used to quantify the probable truncation error of a grid, but no such quantification programs are known for Navier-Stokes grids. Qbert judges the smoothness and orthogonality so it can be used as a relative scale of Navier-Stokes grids, though it doesn't represent the truncation error in such cases. The FAST code (Refs 23 & 24) calculates and visualizes the following grid quality metrics: cell volumes, skewness (cell edge, diagonals, face, and normals), cell face nonplanarity, orthogonality, point distribution stretching, aspect ratio, face normals, and cell Jacobians. The assessment of the grids were performed in-house using both Qbert and FAST.

15

The coarse and fine centerline geometries were extracted from the 3-D surface definitions to provide a starting point for the axisymmetric and 2-D grid generation process. This work was done solely in I3G/Virgo. On the coarse grid, the tighter spacing where the wing root chord leading edge meets the fuselage was smoothed over. Then the centerlines were broken into several pieces, at inflection points or slope discontinuities, and each piece was redistributed using geometric spacing to gain better smoothness than the paneling had because of 3-D considerations. The polar axis lines where generated using a Vinokur cubic spacing. Then a half circle was generated, rotated, and translated into place for the outer boundary. After the 2-D surfaces were generated with TFI, various smoothing options were run for various iterations, and the results were compared with Qbert. Smoothing using Laplace's method for just 10 iterations gave the best results. The coarse grid was dimensioned 172 x 71, and the fine was 254 x 71. The alternative design grid was dimensioned 255 x 71.

5. PANEL STUDY RESULTS

The panel studies were performed at a high altitude cruise condition (Mach number 0.784, 35,000 ft (10,670 m)). This condition was chosen as being the highest Mach number that will be typically seen by the Open Skies aircraft. Runs were also performed at a low altitude condition and at the worse case condition chosen for the follow-on Navier-Stokes runs. Since VSAERO is not a true viscous code, the window recesses were not modeled in these studies. Figures 5 and 6 show the panel study results for the unmodified WC-135B pod and the baseline Open Skies plate with aft bulkhead bump. These data are displayed as an equivalent Mach number from the surface pressure values to give a clearer indication of the region of supersonic flow. Figure 5 shows the flow over the original pod remains subsonic throughout, but over the Open Skies modification significant supersonic flow is seen (Figure 6). Since VSAERO is a panel method it is unable to predict shock waves, but the results can imply that a shock wave would occur over the bulkhead.

The VSAERO results on the baseline Open Skies pod prompted an investigation into ways to make minor contour changes to the pod aft of the plate to minimize the chance for buffeting resulting from shock or separation. Candidate designs with an aft tertiary skin were paneled and evaluated with VSAERO, using the viscous options. This work was documented in a separate memorandum to the customer, 4950 TESTW/ FFX (Ref. 25). Figure 7 shows centerline cuts of the basic contour and the selected alternate fairing design. The alternate fairing was an attempt to move the location of maximum Mach number aft while minimizing the magnitude of the peak Mach number. Figure 8 shows the results of the alternate fairing study, and Figure 9 shows a comparison of pressure coefficients along the centerline of the pods. When compared to the baseline (Figure 6), it can be seen that the fairing could meet the objectives of decreasing the supersonic region and moving the peak Mach number aft. As a result, the alternate fairing was modeled in the Modification Center's CAD system in case flight test showed the need for it.

An important side study was performed with VSAERO to determine the effects of the wing on the flow over the Open Skies modification. Two versions of the coarse 3-D Navier-Stokes surface

17
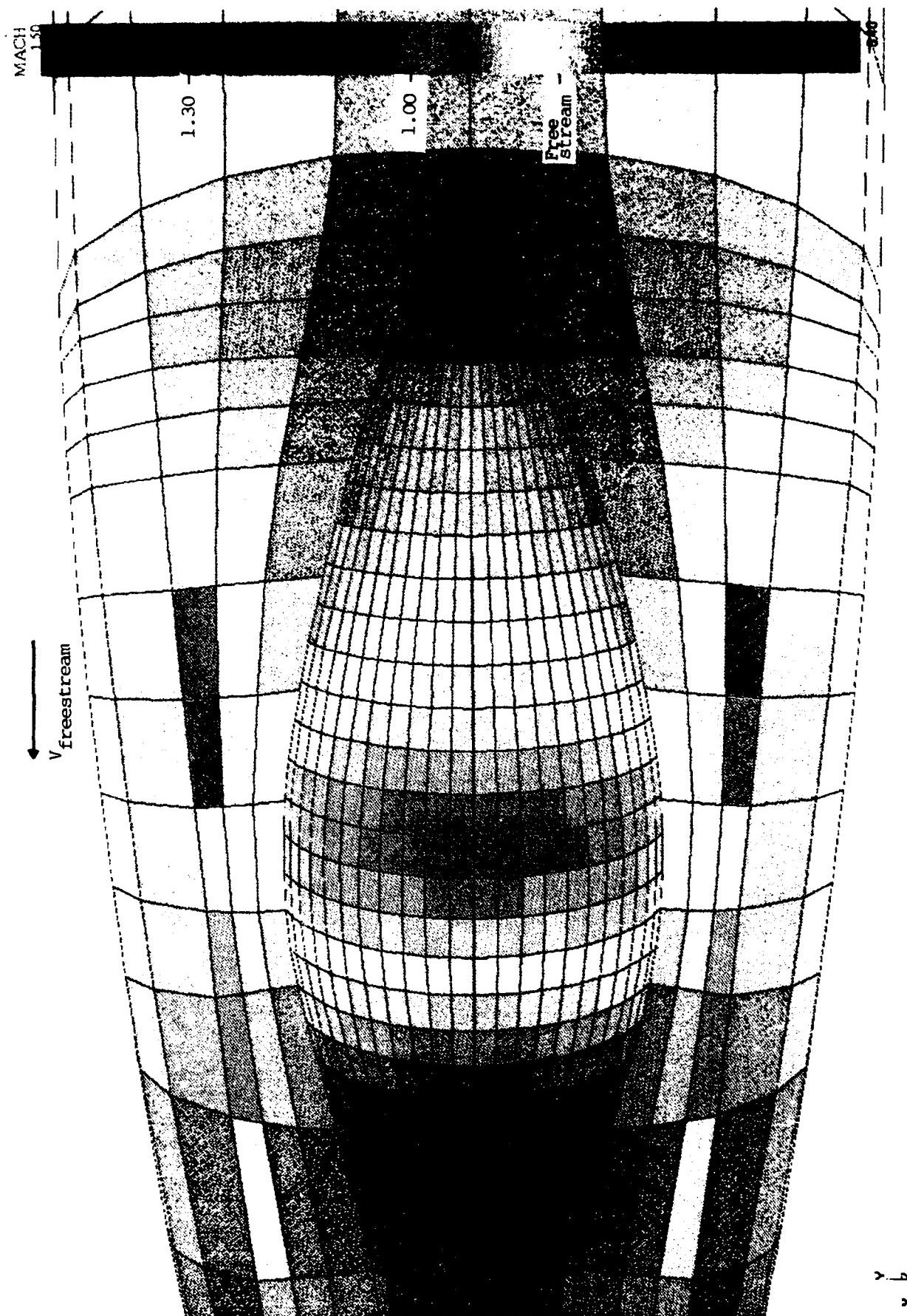
Figure 5: **VSAERO** Mach Contours, Unmodified Pod
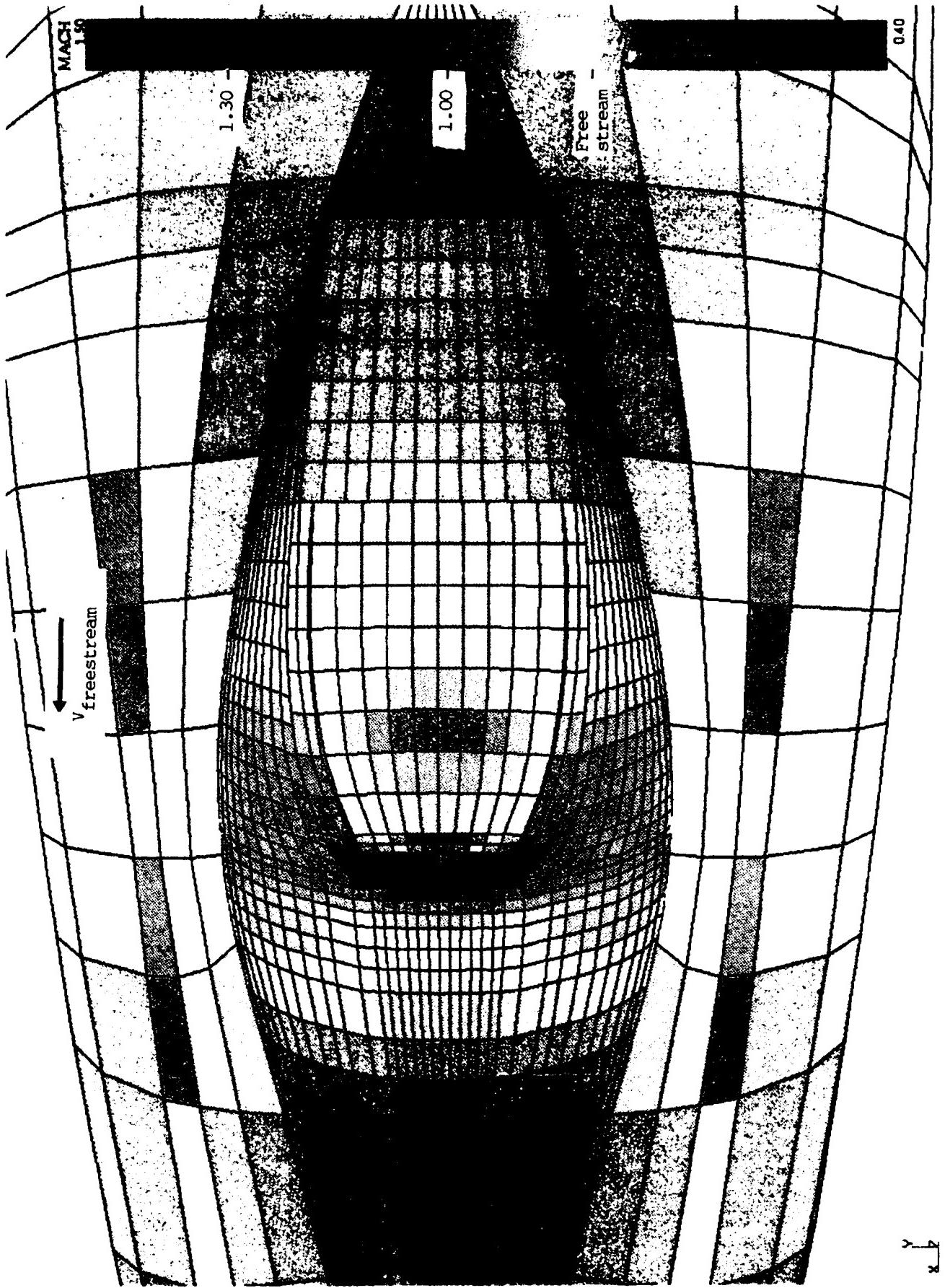
Figure 6: **VSAERO** Mach Contours, Open Skies Pod

19

Station 1319

Station 1344

Existing Aft Pod
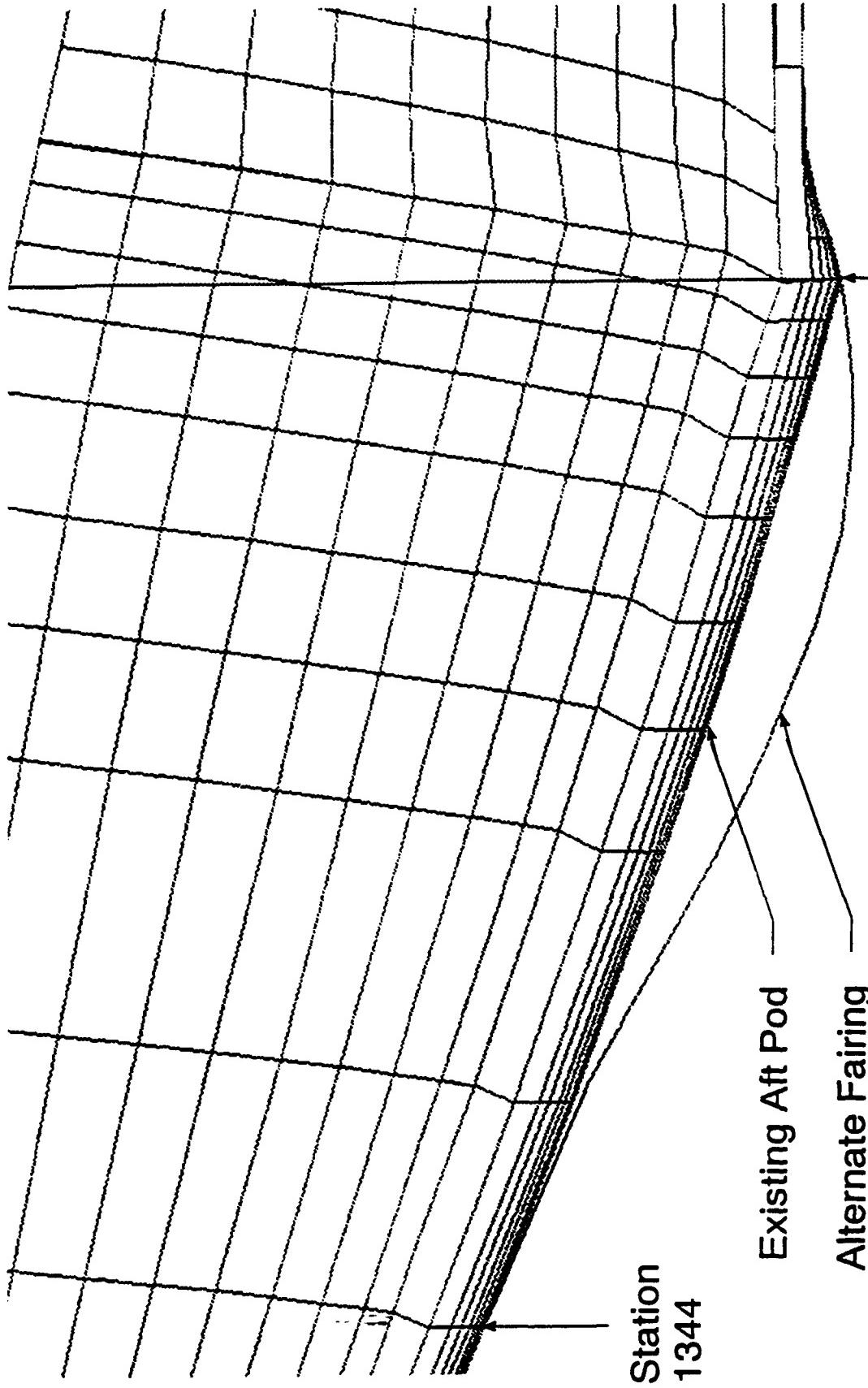
Alternate Fairing

Figure 7: Centerline Cut of the Alternate Fairing Behind the Open Skies Plate

20
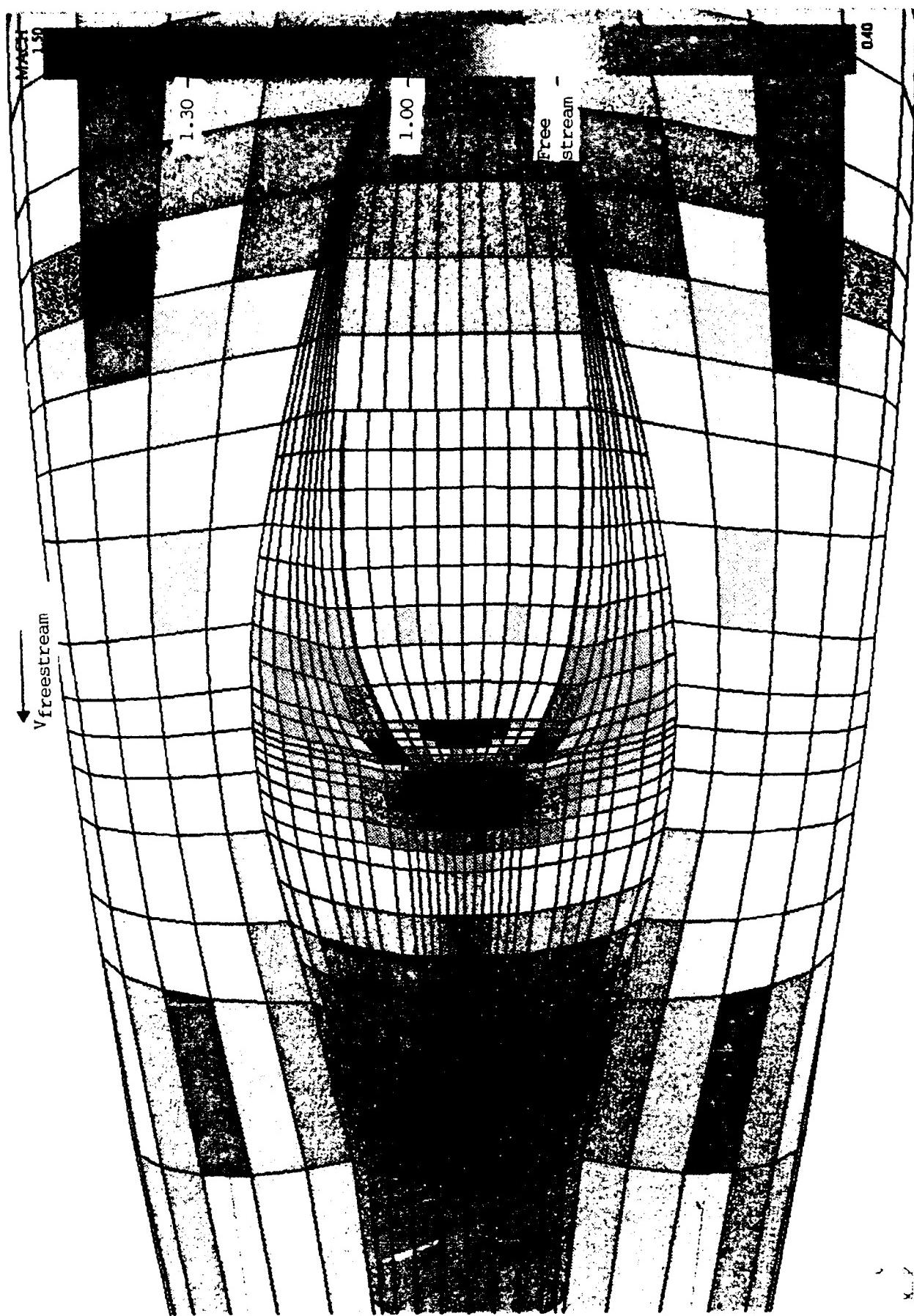
Figure 8: **VSAERO** Results on the Alternate Fairing
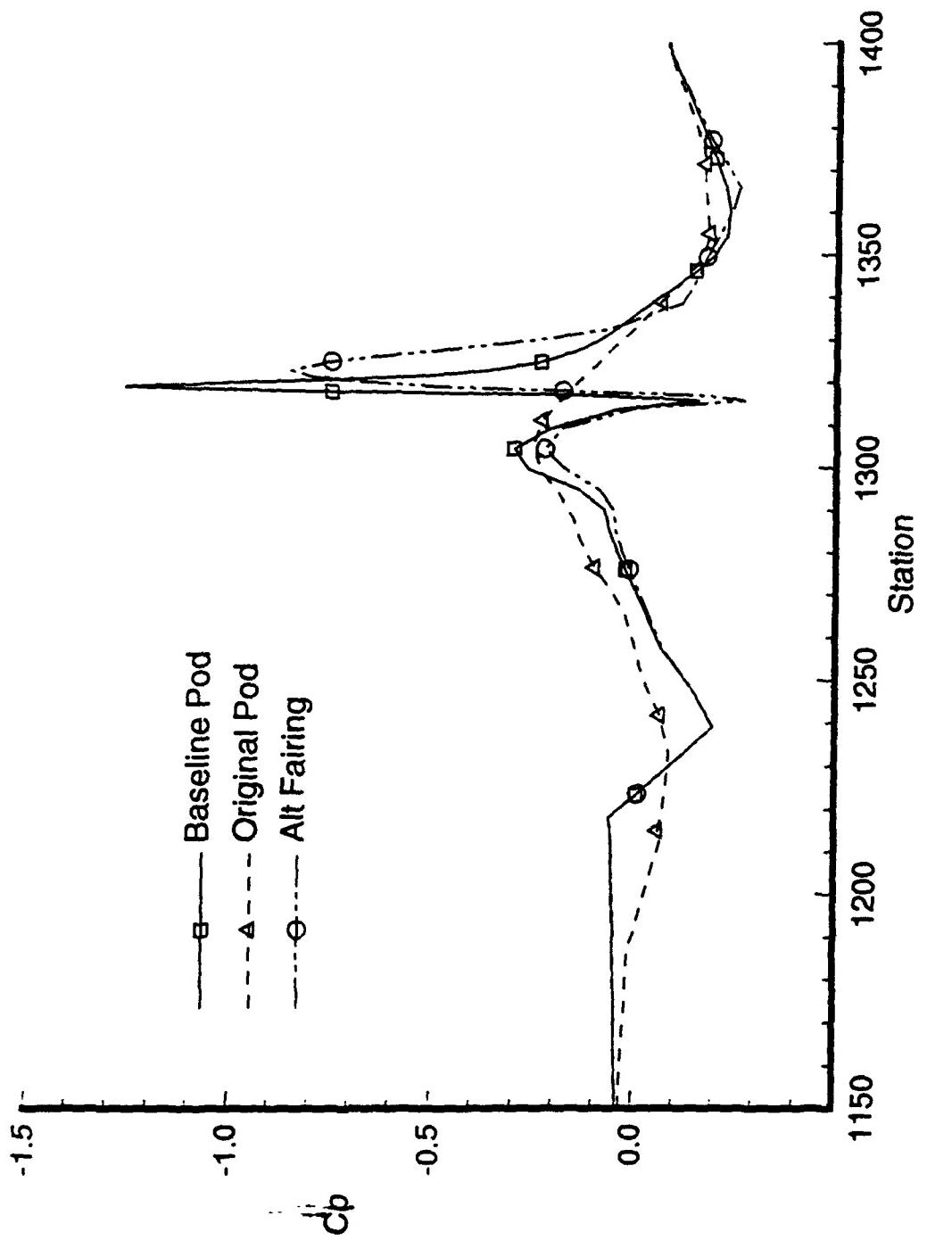
Figure 9: Centerline Cp Comparisons

Baseline Pod
Original Pod
Alt Fairing

Cp

Station

definition were initially paneled; a wing-body and a body alone model. When the difficulty arose in obtaining a good 3-D grid around the wing-body model within the time available, the surface geometries were run with **VSAERO** to determine the necessity of including the wing in the Navier-Stokes runs. Although it was initially expected that the loss of the effects of the wing would lower the peak Mach number over the pod, the results actually showed a slight increase. This is reflected by the more negative peak Cp value shown in Figure 10. Even though there were significant differences between the two configurations beside and behind the pod, the results showed very little change over the modification region. This implied that reasonable results could be obtained with a body alone CFD study. The slight increase in peak Mach number for the body alone configuration was later supported by results from the full potential code.

A run with **VSAERO** on the first cut of the fine 3-D Navier-Stokes surface geometry was also performed. This run was quite helpful to the CFD study in that it revealed waves in the panel surface definition at the pod/fuselage juncture. The waves adversely affected the pressure coefficient distribution on the Open Skies plate. The fine 3-D geometry was then regridded based on the finite element model. A **VSAERO** run of the new geometry confirmed the geometry was now ready to be input into the Navier-Stokes computations. Though the **Spin3D** code that performs pre and post-processing for **VSAERO** showed some wrinkles were still present where the finite element definition was patched into the panel definition, their effects did not extend over the modification region. The results agreed with the **VSAERO** Mach number flowfield on the basic panel geometry of Figure 6.
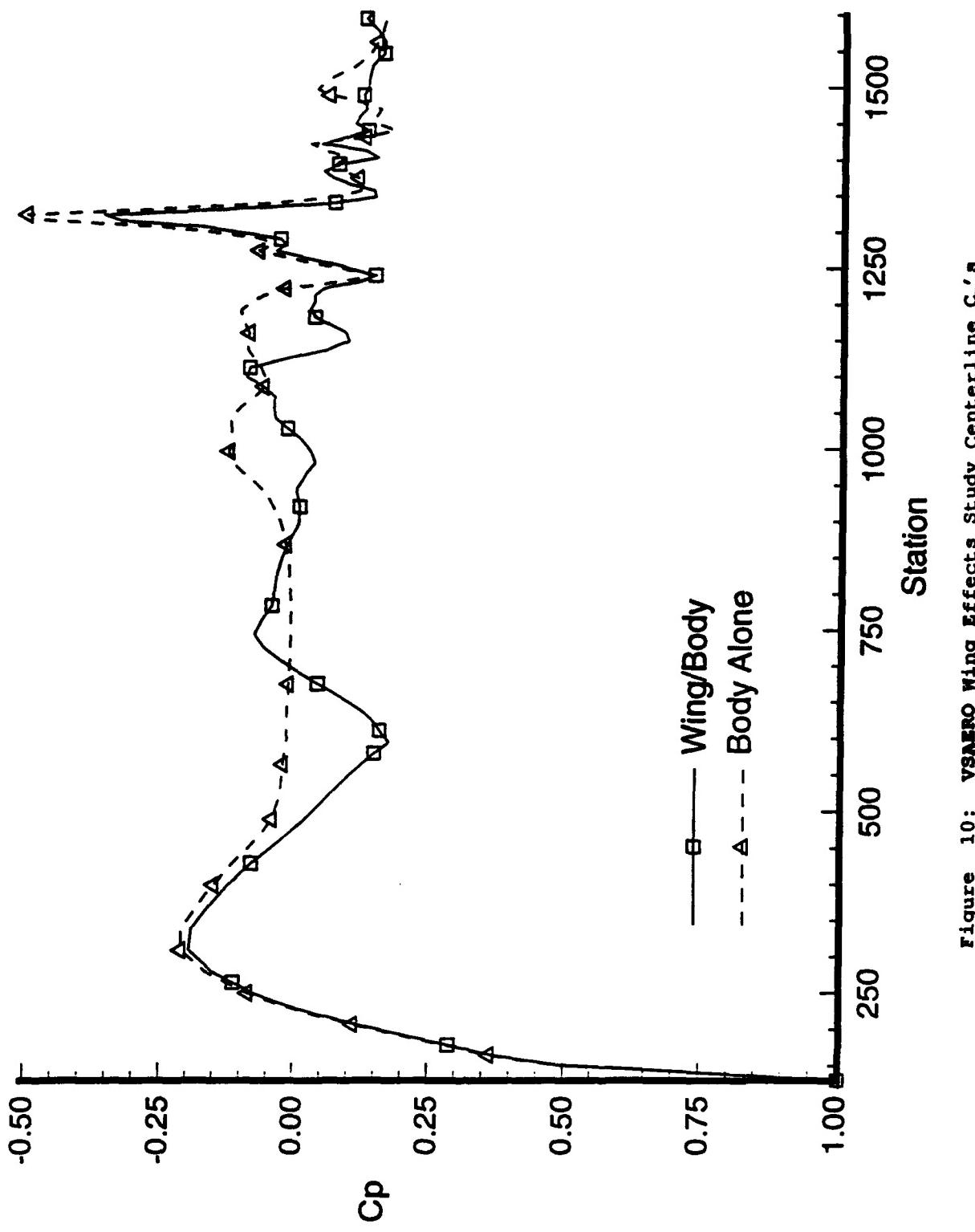
Figure 10: **VSAERO Wing Effects Study Centerline C_p's**

6. FULL POTENTIAL RESULTS

The full potential code provided an added compressibility modeling for more accurate transonic flow effects, which panel methods do not provide. Although **VSAERO** has an off-body flowfield survey utility, its inability to predict shocks caused it to over-predict the peak off-body Mach number. **TRANAIR**, therefore, provided a better 3-D off-body prediction, although without viscous effects. Figure 11 shows the predicted pressure field over the pod. Figure 12 shows the Mach numbers; and Figure 13 shows the density variations over the pod. The results indicate the presence of a shock. However, it was not known how much viscous effects would influence the answer.

The use of **TRANAIR** also provided a second look at wing-body versus body alone predictions. Figure 14 shows the pressure coefficient (C_p) comparisons along the centerline. As in the **VSAERO** wing-body study, the **TRANAIR** study showed the same trends upstream of the pod. The lower symmetry plane near the modification region is presented in the following figures. As with **VSAERO, TRANAIR** also predicted slightly more suction (compare Figure 15 with Figure 16) and a higher peak Mach number (compare Figure 17 with Figure 18) over the pod for the body alone case than for the wing-body case. No significant difference in the density ratio was noted (Figures 19 & 20), which is mentioned not just from a conservation of mass check but also considering optical diffraction.

At the bulkhead location near the surface, the peak Mach number reached 1.7 with a fairly small surrounding area of Mach numbers 1.1 - 1.3 as seen in the flowfield Mach contour (Figure 18) for the body alone case. The supersonic region was fairly small and immediately "shocked" back to subsonic flow. The C_p had a peak negative value of -1.40 with surrounding values between -0.60 to -1.14 as seen in the flowfield C_p contour (Figure 16). The density ratio had a peak minimum value of 0.43 with surrounding values ranging between 0.7 and 0.5 as seen in the flowfield density contour (Figure 20).

For the wing-body case, the peak Mach number was reduced to 1.5, and the surrounding Mach numbers reduced to 1.0 - 1.2 as seen in the flowfield Mach contour (Figure 17). A reduction in the

Figure 11: TRANAIR C_p Contours (WB), Bottom View of Modification

1.60

1.31
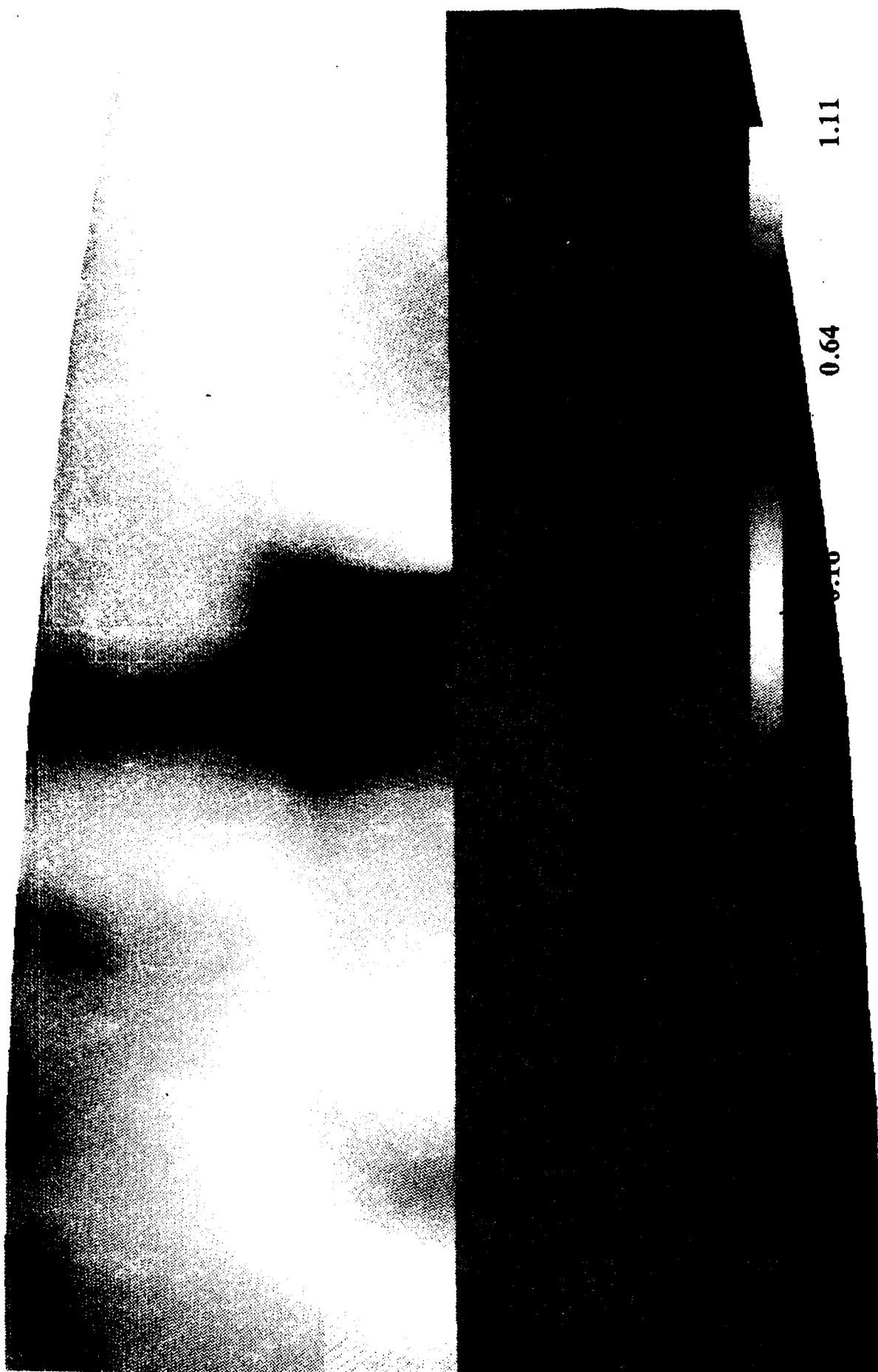
Figure 12: TRANAIR Mach Contours (WB), Bottom View of Modification
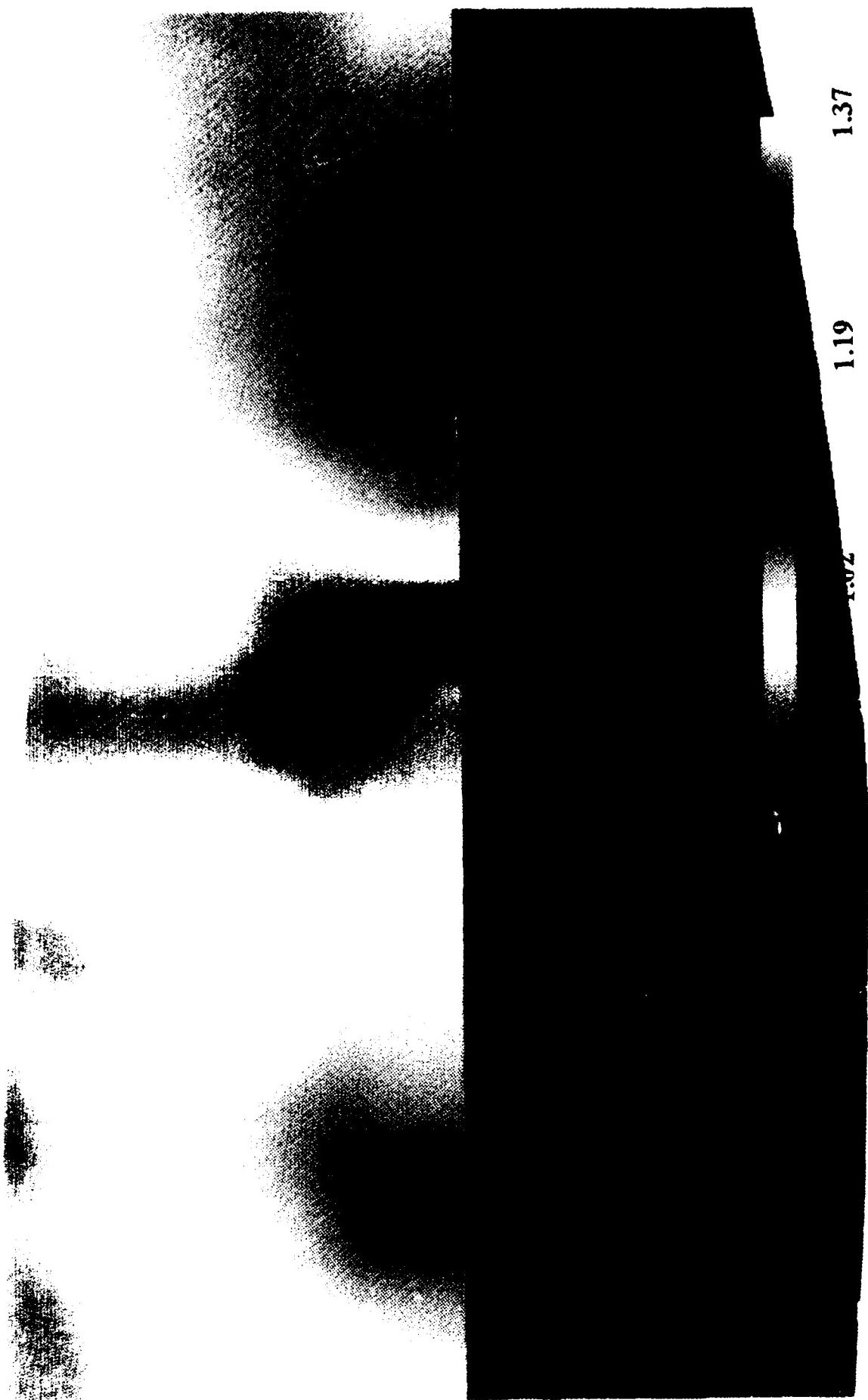
Figure 13: TRANAIR Density Contours (WB), Bottom View of Modification
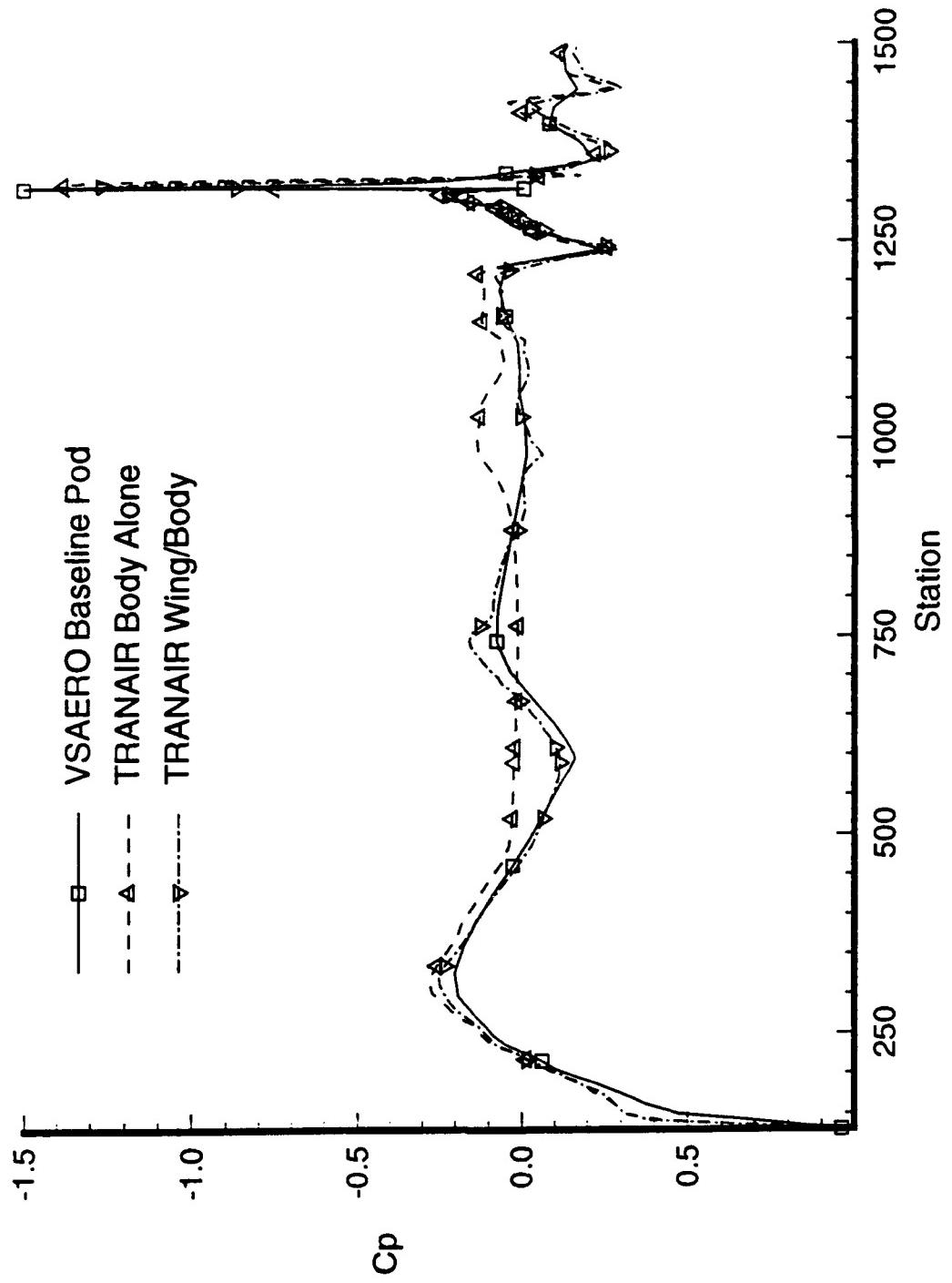
Figure 14: TRANAIR Wing Effects Study

29
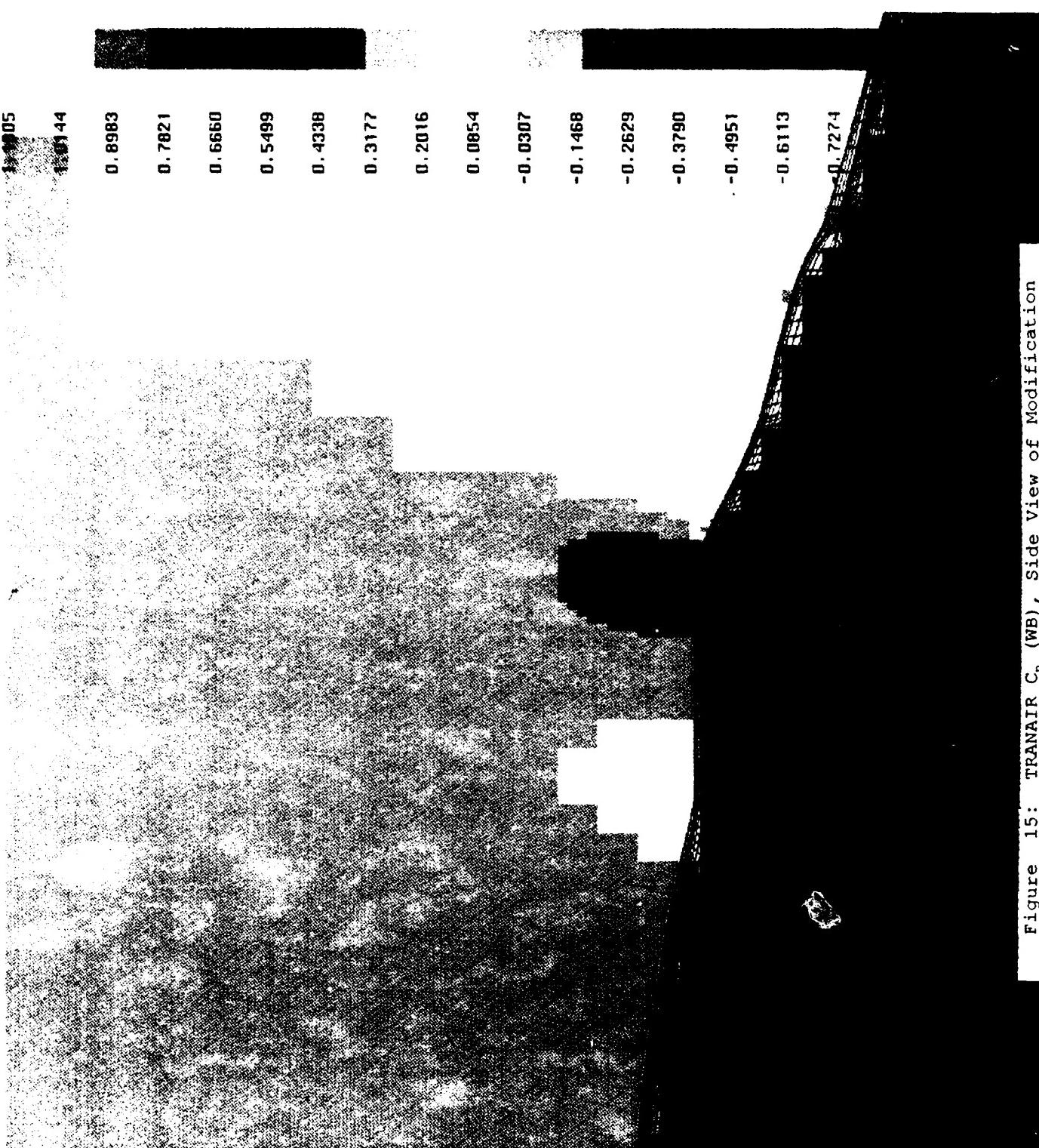
Figure 15: TRANAIR C_p (WB), Side View of Modification

The following values appear along the color scale legend:

- 0.8983
- 0.7821
- 0.6660
- 0.5499
- 0.4338
- 0.3177
- 0.2016
- 0.0854
- -0.0307
- -0.1468
- -0.2629
- -0.3790
- -0.4951
- -0.6113
- -0.7274
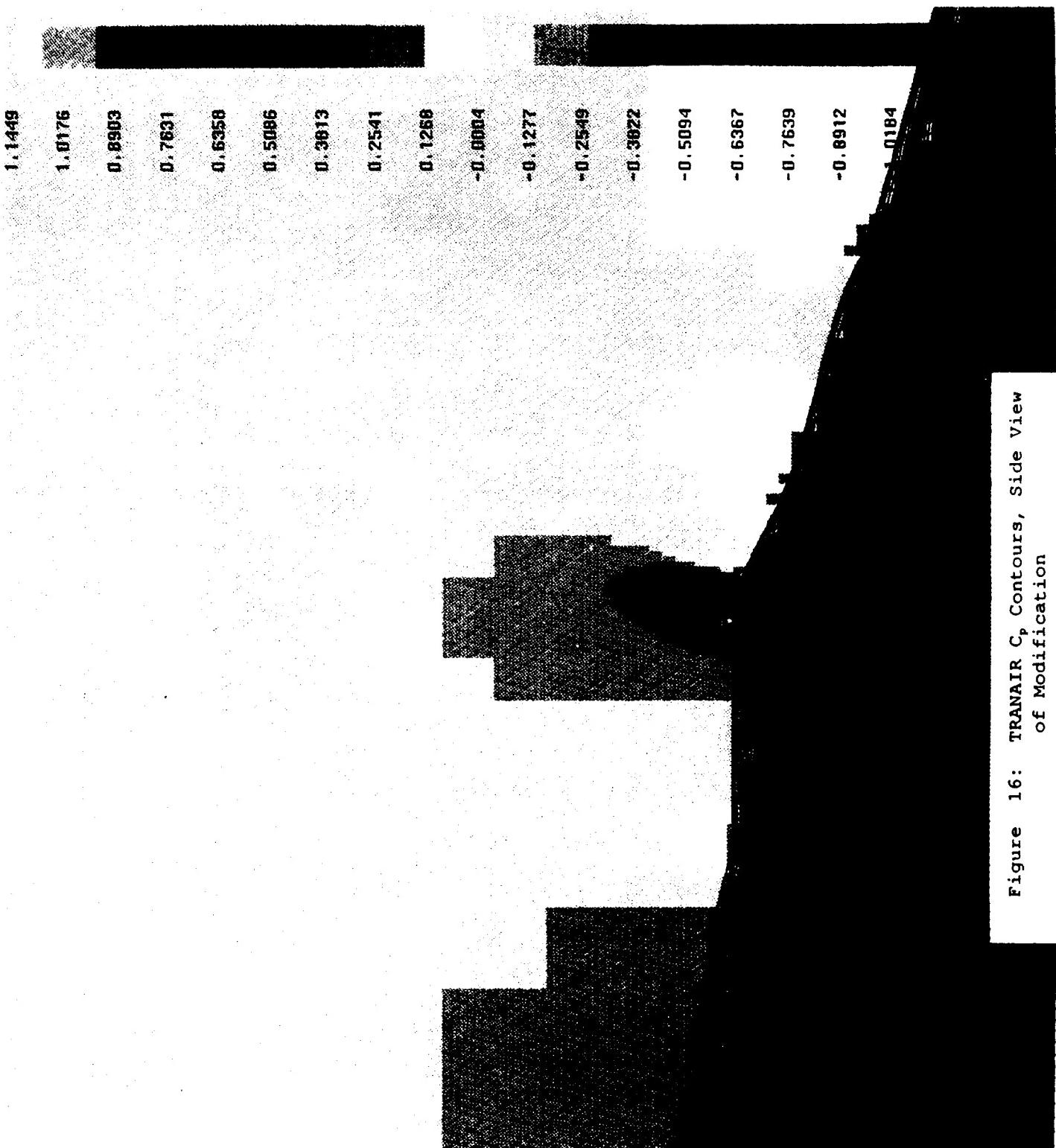
Figure 16: TRANAIR C_p Contours, Side View of Modification

1.5843
1.4857
1.3971
1.3285
1.2599
1.1913
1.1227
1.0541
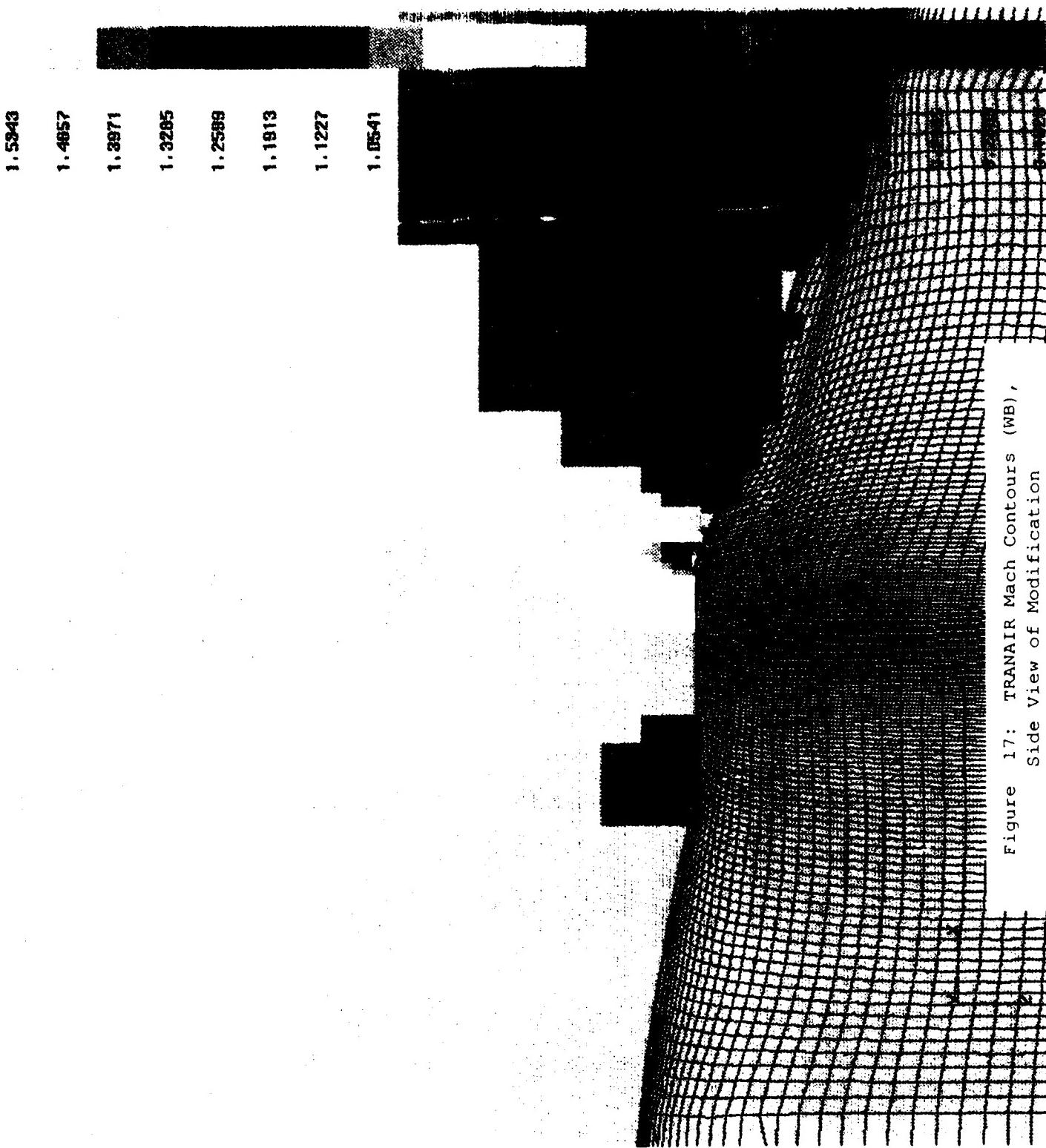
Figure 17: TRANAIR Mach Contours (WB),
Side View of Modification
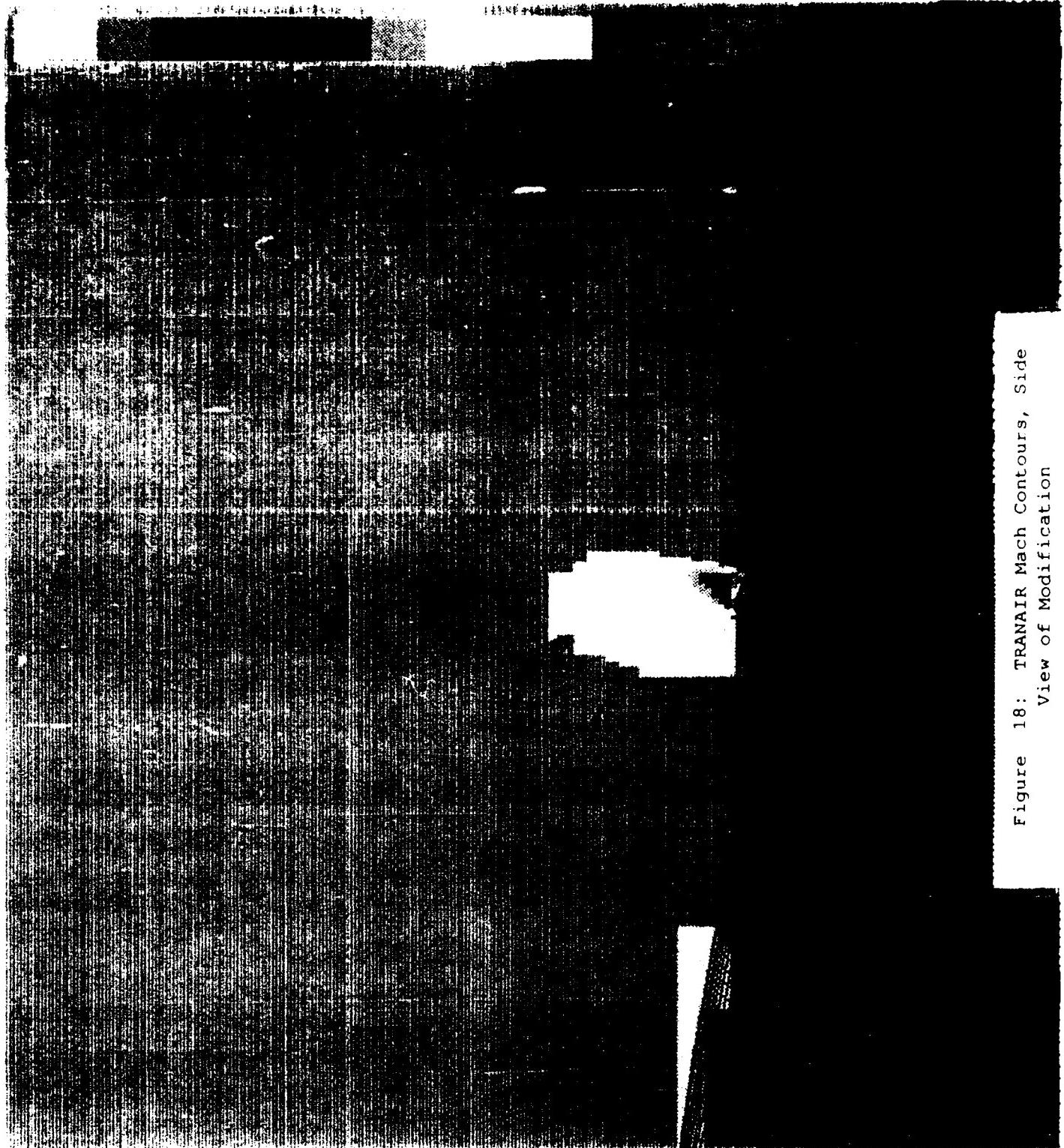
Figure 18: TRANAIR Mach Contours, Side View of Modification
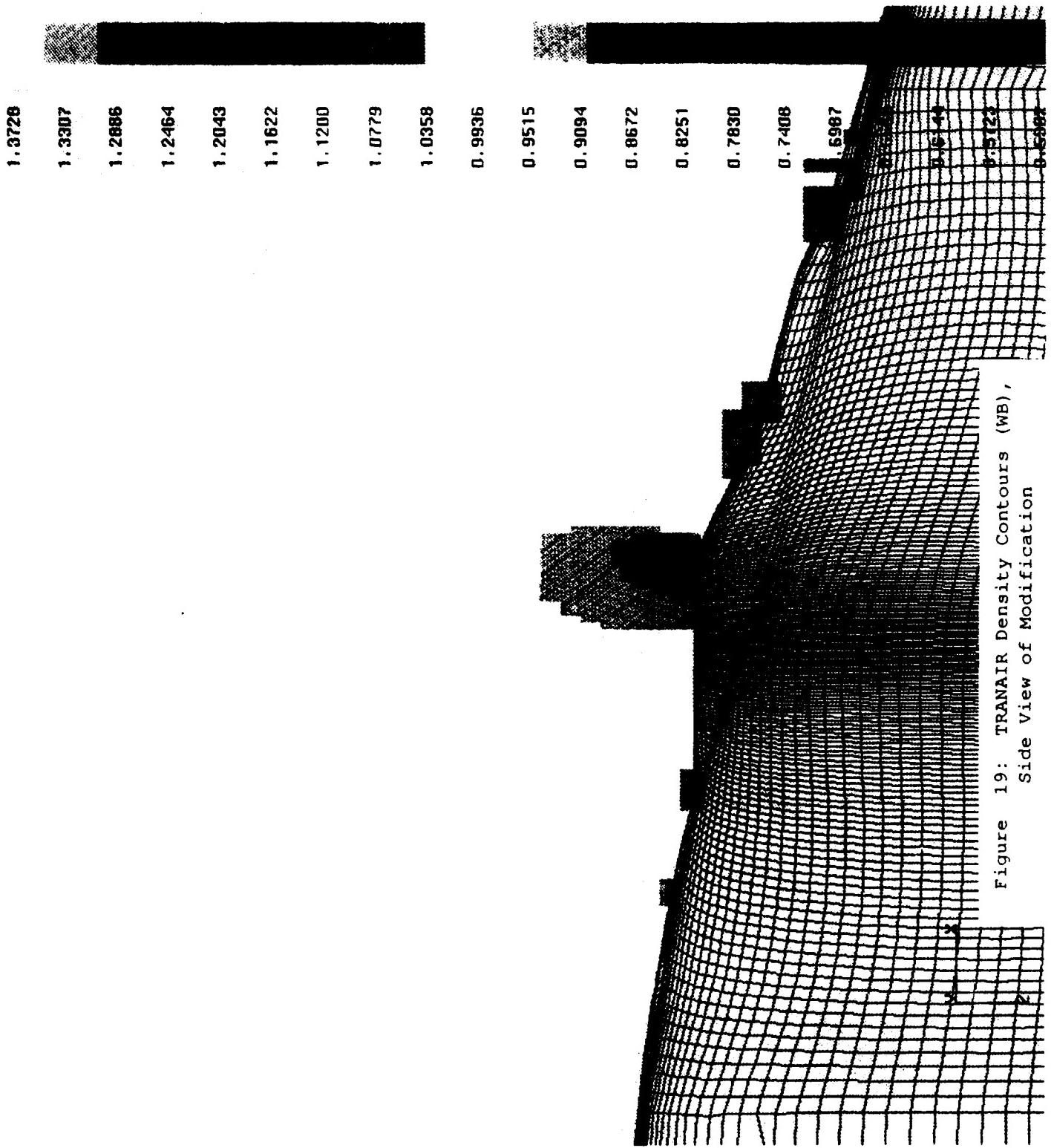
Figure 19: TRANAIR Density Contours (WB), Side View of Modification

1.3728
1.3307
1.2886
1.2464
1.2043
1.1622
1.1200
1.0779
1.0358
0.9936
0.9515
0.9094
0.8672
0.8251
0.7830
0.7408
.6987
0.6565
0.5723
0.5302

1.3773

1.3300

1.2827

1.2355

1.1882

1.1409

1.0936

1.0463

0.9990

0.9517

0.9045

0.8572

0.8099

0.7626

0.7153

0.7??

0.4?89

0.4316

Figure 20: TRANAIR Density Contours, Side
View of Modification
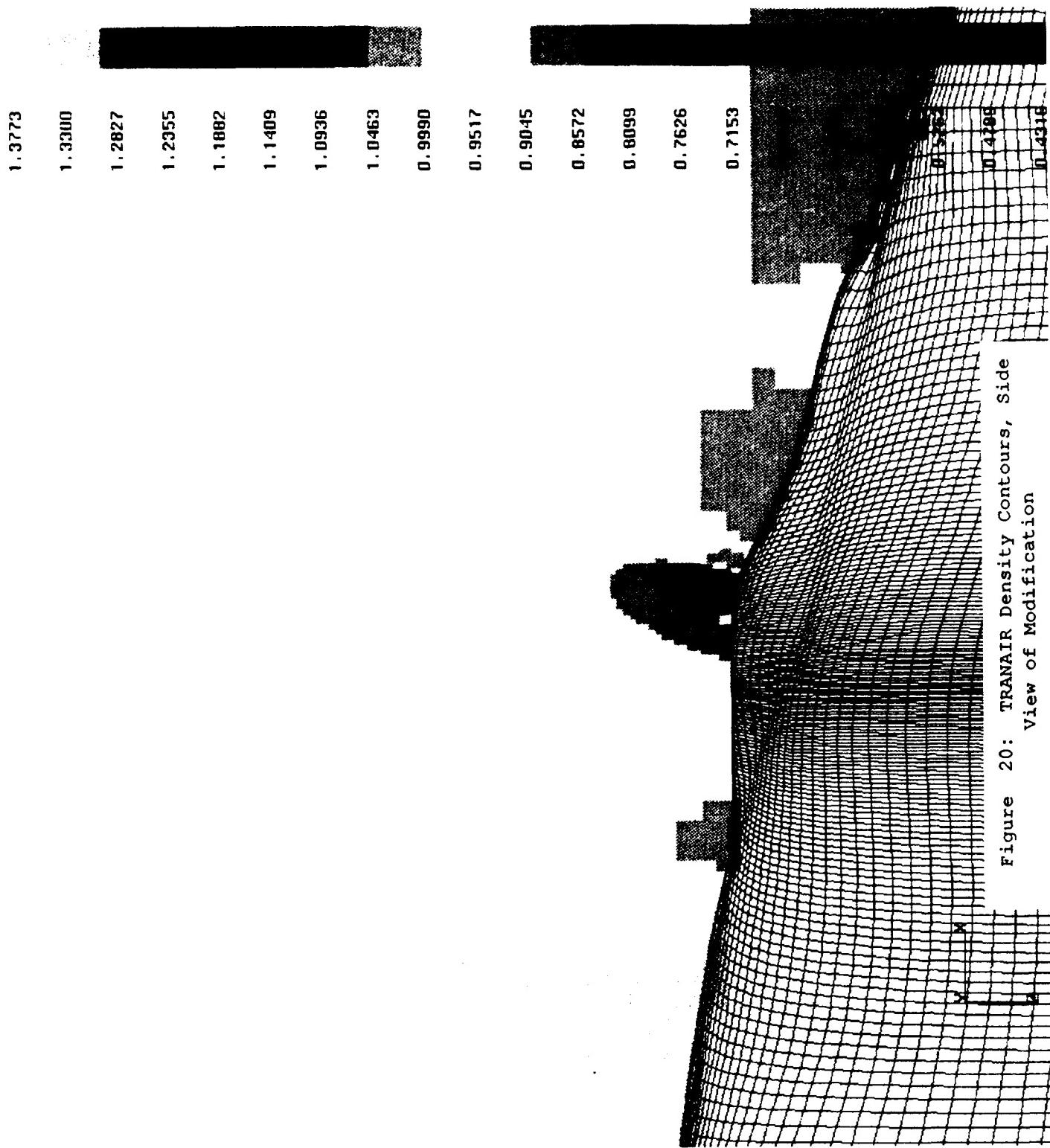
size of the supersonic region was also observed. The C_p peak decreased to -1.19 with surrounding values between -0.49 to -0.80 as seen in the flowfield C_p contour (Figure 15). The minimum density ratio increased to 0.53 with surrounding values between 0.8 to 0.6 as seen in the flowfield density contour (Figure 19). Since the body alone results differed only slightly from the wing-body results, it was concluded that performing the Navier-Stokes study without the wings would give reasonable, slightly conservative results.

For lessons learned purposes, a few notes about the full potential code should be made. It was found during the analysis that the wing tip panels needed to be very small for a successful solver analysis. Sharp slope discontinuities were discovered to give results that were grid resolution dependent. Increasing the grid resolution caused the extent of excessive local errors to decrease rapidly; further increases brought less of a change. The final grid resolution was selected by choosing the grid that reasonably approached what seemed to be an asymptotic limit.

7. NAVIER-STOKES RESULTS

7.1 Introduction:

In selecting a supercomputer to perform the Navier-Stokes simulations, the capabilities and cost effectiveness of the computer systems at Wright-Patterson AFB, Eglin AFB, and Kirtland AFB were evaluated (Ref's 26-30). The Cray II at Kirtland AFB was selected mainly because the **GASP** software had been used on it and the memory available was large enough for the project. The Cray II system runs a similar operating system to the WPAFB Cray **XMP**, with nearly identical compilers; this made porting code straightforward, except for a few subtle differences in architecture and operating systems. Utilization of the machine was usually relatively low enabling faster than normal turn-around time. The CPU is also about three times faster than the **XMP1/2**. The required software was transferred to KAFB, backed up, and compiled. All files needed to be backed up on their Central File System (CFS), as they were generated, to protect against unexpected purges.

7.2 GASP Description:

The General Aerodynamic Simulation Program (**GASP**) finite volume CFD code was selected for the project because of its proven accuracy (Ref. 31). Its superior speed for 3-D problems was another main factor for its selection. Finally, its cost was economical -- even more so with the limited freeware demonstration agreement. This shock capturing program is capable of performing time accurate or time warping solutions of the Euler, Thin-Layer (TLNS), Slender-Layer (SLNS), or Full Navier-Stokes equations. The solution can be either parabolized (space marched) (PNS) or elliptical (global iterations). The turbulence modeling is fully coupled with the flow equations. The code provides the user with broad control over convergence acceleration schemes, boundary conditions, flux treatment, etc. The documentation of the code is excellent, with a complete coverage of its formulation, and many pragmatic examples of how to set up simulations. For this simulation, the options chosen were normal direction only TLNS, adiabatic wall, third order Roe's

37

scheme, Sutherlands viscosity, triple point surface treatment, Van Leer limiters, triple level grid sequencing, and Courant-Friedrichs-Lewy (CFL) number ramping from 0.5 up to 10 (Ref. 8).

The flat plate **GASP1.3** check run results showed a good log-law boundary-layer profile. A little optimization of **GASP2.2** performance on the system was then performed to speed up the large analyses, thus reducing costs. A supercritical airfoil analysis of the NASA SC-31 showed that the **GASP2.2** turbulence modeling implementation gave good correlation to experiment (Figure 21).

7.3 NASTD Description:

The NAvier-Stokes Time Dependent (**NASTD**) finite volume CFD code was obtained from the McDonnell Douglas Aircraft Company. The code is proprietary to McDonnell Douglas and so is the CPUsec per iteration per node information. The program can perform Euler, PNS, TLNS, and FNS analysis with either 1-D variable width, 2-D, axisymmetric, or 3-D geometry. It does not require a 3-D grid for lower dimensioned cases as **GASP** does; it is coded for the appropriate internal transformations. The k–ε equations in **NASTD** are formally decoupled and time lagged. The turbulent Navier-Stokes equations were Favre averaged (Ref. 32). Like **GASP**, it has numerous chemistry, thermodynamic and turbulence models. However, documentation was limited compared to most CFD codes. The robustness of the code was impressive. In the Open Skies simulations the first order Roe scheme was used for initial convergence, then switched to second order. Total Variation Diminishing (TVD) was used, with the full block tridiagonal implicit operator, along with CFL ramping to accelerate convergence. Adiabatic wall boundary conditions were set for the vehicle surfaces.

The **NASTD** CFL was set to 0.1 and ramped to 0.4 over a few hundred iterations. All the solutions were converged to approximately 0.0001 in the average residuals. The coarse axisymmetric solution required 4000 iterations to appropriately develop the flowfield, using Baldwin-Lomax (B-L). The coarse 2-D run was restarted from the coarse axisymmetric solution and needed an additional 1600 iterations to converge. The fine axisymmetric case took a total of 12,000 iterations to obtain a k-ε solution.

GASP2.2 Results -- Pressure Coefficient
NASA SC-31 M=.82 AOA=.1 2 vs. 3 Decades Conv.
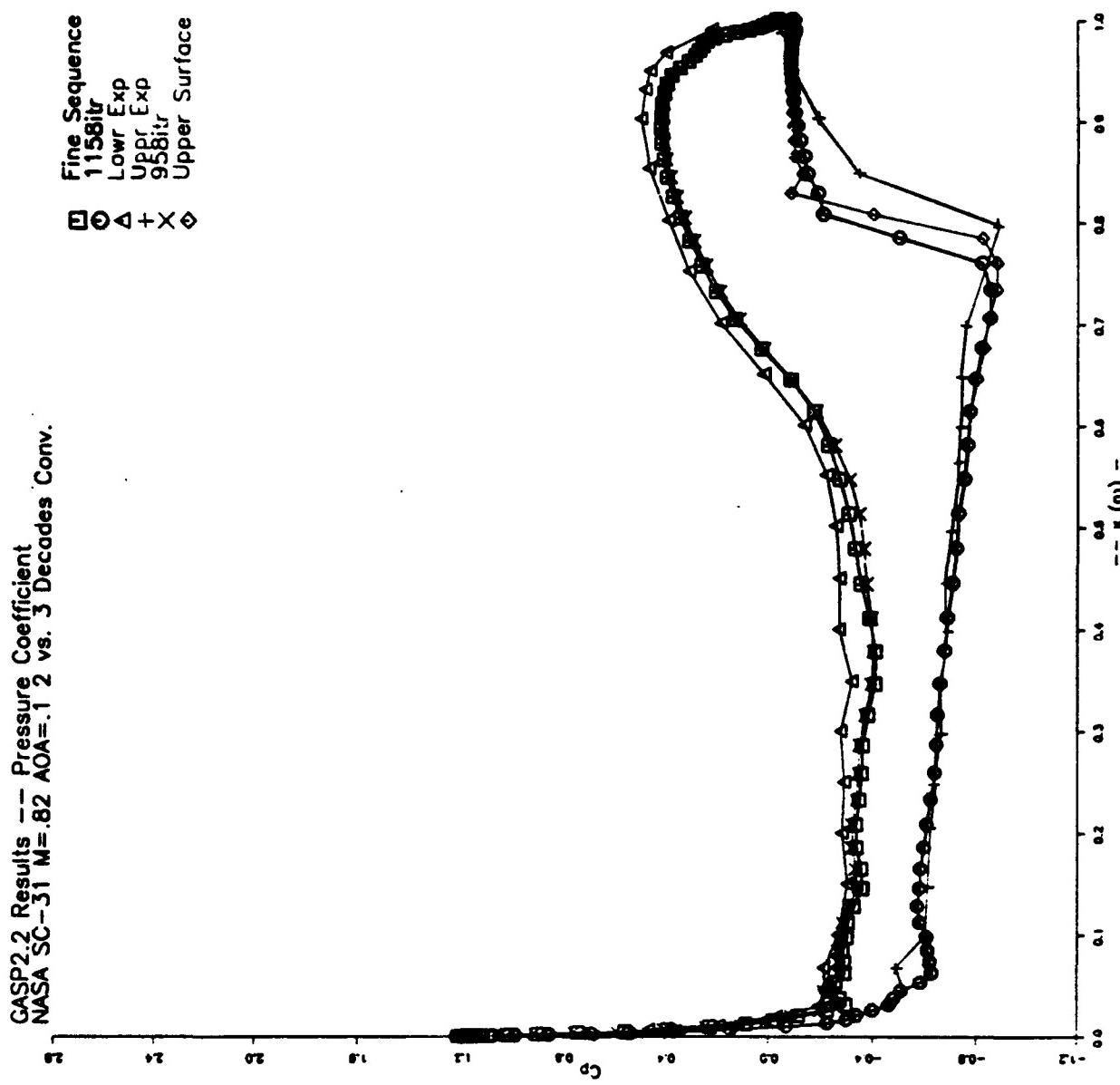
Figure 21: GASP Validation on NASA SC-31 Airfoil

39

7.4 Boundary Conditions:

The 2-D and axisymmetric boundary conditions were set as follows: the Imin line (near the stagnation line) was input as a reflection plane as was the Imax line (running aft of the tail). The Jmin line (surface of the fuselage) was set to no-slip adiabatic wall and the Jmax boundary (outer boundary) was set to freestream inflow for the forward half, and freestream outflow for the aft half. As previously stated, the axisymmetric study was performed by analyzing a body of revolution defined by the bottom centerline of the aircraft.

For the 3-D cases, before the grid was cut, the Imin plane was approximately the stagnation line. The Imax plane was aft of the tail. The J planes formed the upper and lower symmetry planes. Finally, the Kmin plane was the aircraft surface, and the Kmax plane was the outer boundary. The body surfaces were set to no-slip adiabatic wall conditions. For the coarse 3-D grid the outer boundary was set to freestream inflow to the half I index point, and freestream outflow for the aft half. In the fine 3-D grid the aft two outer grid zones were set to freestream outflow. The Imin planes for zones 1 and 2 (in the fine 3-D grid) were set to user specified arbitrary inflow, to enable the use of conditions interpolated from the coarse simulation.

7.5 Turbulence Model Selection:

Two-equation models give reasonably accurate predictions for simple flows, and are generally better than Baldwin-Lomax (or other algebraic models) since they incorporate more of the flow physics (Table 1). They have the limitations of overpredicting reattachment heat transfer and separation pressure rise, and underpredicting the separation bubble sizes and shear layer spreading rate. They are also deficient in predicting complex flows such as shock wave boundary-layer interactions involving separation. In-house calculations show they don't agree well in the turbulence quantities themselves (Figures 22 to 24). In spite of these limitations, it was decided to proceed with two-equation models because models of higher complexity would have been too costly to run. The Open Skies modification is complex, as it includes multiple triple corners in subsonic flow with right angle sharp edges, two-dimensional parts adjoining curved geometry, and three-dimensional contour
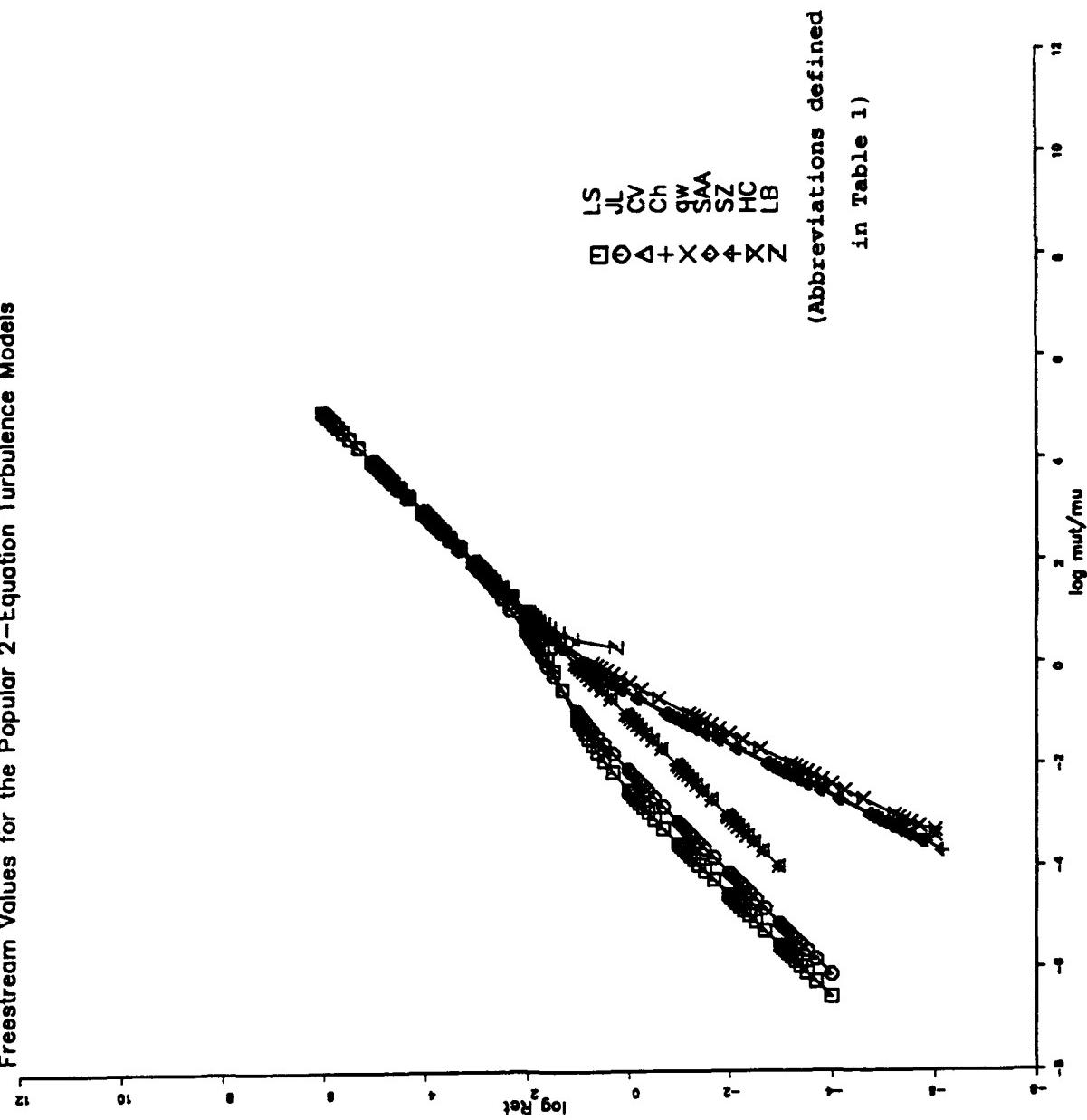
Figure 22: Re_t vs. μ_t/μ for Various 2-Equation Models
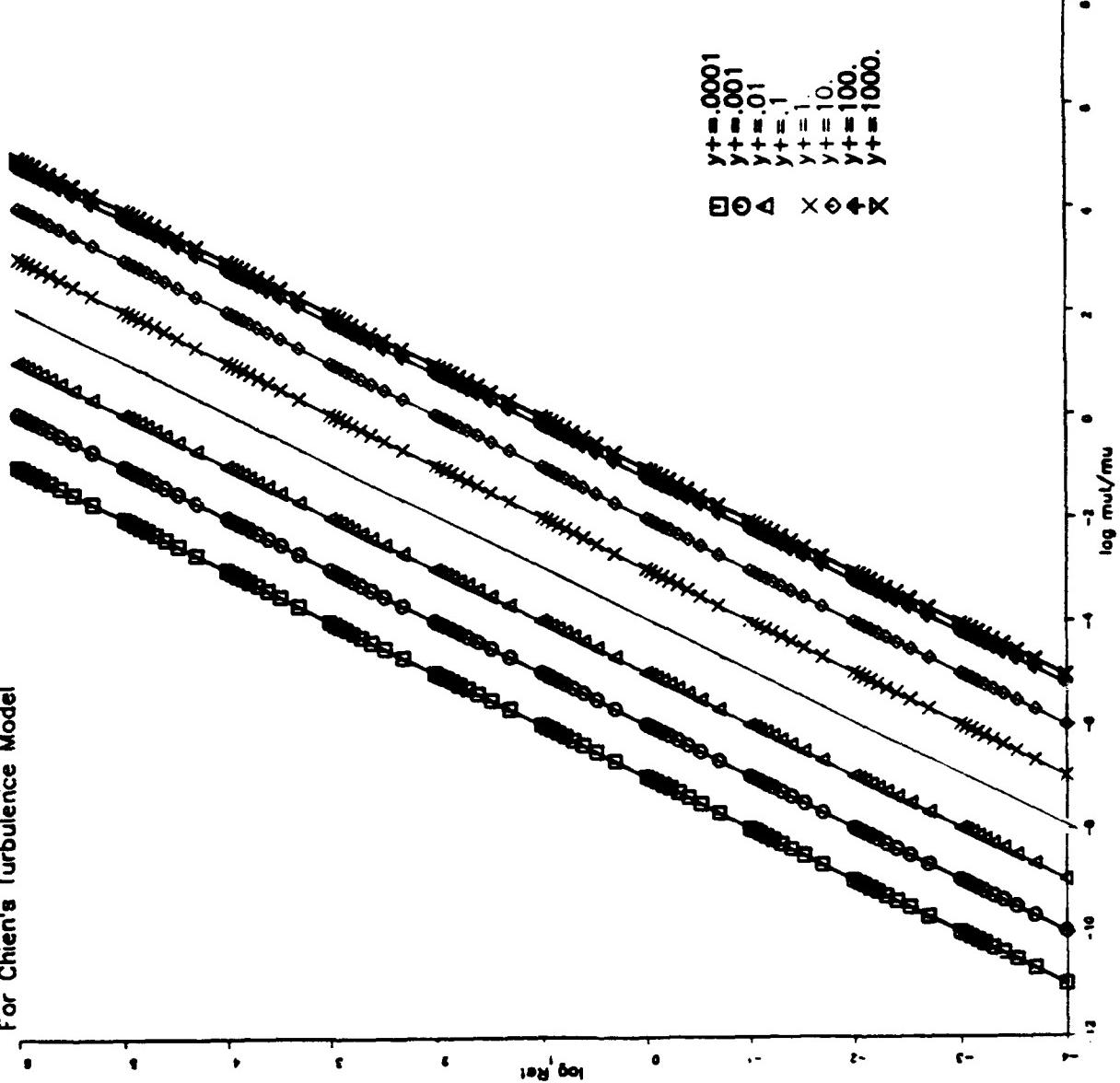
Figure 23: Re_t vs. μ_t/μ for Chien's Model

Figure 24: Sublayer Values for the Popular Two-Equation Models

corners. Based on Dr. Rizzetta's recommendations, the low Reynolds number Jones-Launder model was selected. This model is independent of y^+ thus avoiding potential numerical confusion in the corner regions. It is apparent from the literature that this method is better than most of the other two-equation models in predicting accurate separation pressure peaks (Ref's 32-40). The fall-back model selected was Chien's (Figure 23).

The procedure chosen was to initially converge the fine grid solutions using the Baldwin-Lomax turbulence model (Ref's 41-43). The solution would then be further iterated using the Jones-Launder k-ε turbulence model. This method was chosen to obtain faster initial convergence, then using k-ε to resolve any separated region predicted by the solver. Baldwin-Lomax is not typically well behaved with separated flows.

Table 1: Turbulence Models Considered

Method	μ_t/μ Equation
Coakley & Vuong's model (CV)	$0.09 \cdot R_{et} \cdot (1.-\exp(-0.022 \cdot R_q))$
Chien's model (Ch)	$0.09 \cdot R_{et} \cdot (1.-\exp(-y^+/87.))$
Wilcox's model (q-ω)	$0.09 \cdot R_{et}$
Speziale, Abid,& Aderson's model (SAA)	$0.09 \cdot R_{et} \cdot (1.+3.45/\mathrm{sqrt}(R_{et})) \cdot \tanh(y^+/70.)$
So & Zhang's model (SZ)	$0.096 \cdot R_{et} \cdot (1.+3.45/\mathrm{sqrt}(R_{et})) * \tanh(y^+/115.)$
Haung & Coakley's model (HC)	$0.09 \cdot R_{et} \cdot \tanh((y^+/43.)^2) \cdot x$ where $x=\max(1.,10.1/\mathrm{sqrt}(R_{et}))$
Lam-Bremhorst's model (LB)	$0.09 \cdot R_{et} \cdot (1.+20.5/R_{et}) \cdot (1.-\exp(-0.0165 \cdot R_y+))^2$
Launder-Sharma's model (LS)	$0.09 \cdot R_{et} \cdot \exp(-3.5/(1.+0.02 \cdot R_{et})^2)$
Jones-Launder's model (JL)	$0.09 \cdot R_{et} \cdot \exp(-2.5/(1.+0.02 \cdot R_{et}))$

7.6 Coarse 3-D Results:

As stated in the approach section, the first Navier-Stokes results were obtained on a 3-D body alone geometry, but with a coarser grid than is normally used for Navier-Stokes calculations. Because of the coarseness of the grid, this was only used to define the initial overall flowfield for the fine 3-D grid simulation, and to check trends. Comparisons with **VSAERO** results on the coarse surface geometry were favorable. The coarse grid, however, did not capture the height of the bulkhead protuberance at the back of the plate, and therefore showed a significantly lower peak Mach number than the fine grid results. The boundary layer profiles looked appropriate based on Ref. 44.

The coarse 3-D **GASP** solution was performed in four days. It used grid sequencing for 200 iterations on two grid levels, which is equivalent to about three orders of magnitude on the finest level. The simulation lasted a total of 25 CPU hours, 1050 iterations, and cost $15K in total (Figure 25). Because of prohibitive costs (Table 2), further **GASP** runs were not performed on the Kirtland system.

NASTD was used on the coarse 3-D grid as well, to make a code to code check correlation. The **NASTD** solution was run without utilizing the grid sequencing option. Good pressure agreement was obtained between the results from the **NASTD** and **GASP** codes. Figures 26 to 37 show the overall details of the vehicle flowfield. Figures 38 to 44 show comparisons between **NASTD** and **GASP**. These plots and similar ones of the lower symmetry plane are upside down, to place the area of interest next to the colorbar. The skin friction and internal energy viscous results, of the two codes, agree in trend but not in quantitative levels. This is partly explained by code algorithmic differences, and because the **NASTD** run was for Mach number 0.84 instead of Mach number 0.8323. The nonphysical values at the nose and tail, for **NASTD**, are an oversight in its postprocessor. Figures 45 and 46 show the **NASTD** convergence history. Both coarse grid solutions were run using the Baldwin-Lomax turbulence model. The k-ε model was not used because the sharp corners were not resolved in the coarse geometry.

GASP2.2 Preliminary Results Convergence Rates
Open Skies .4Million pt grid M=.8323 AOA=1.4

☐   Fine Sequence
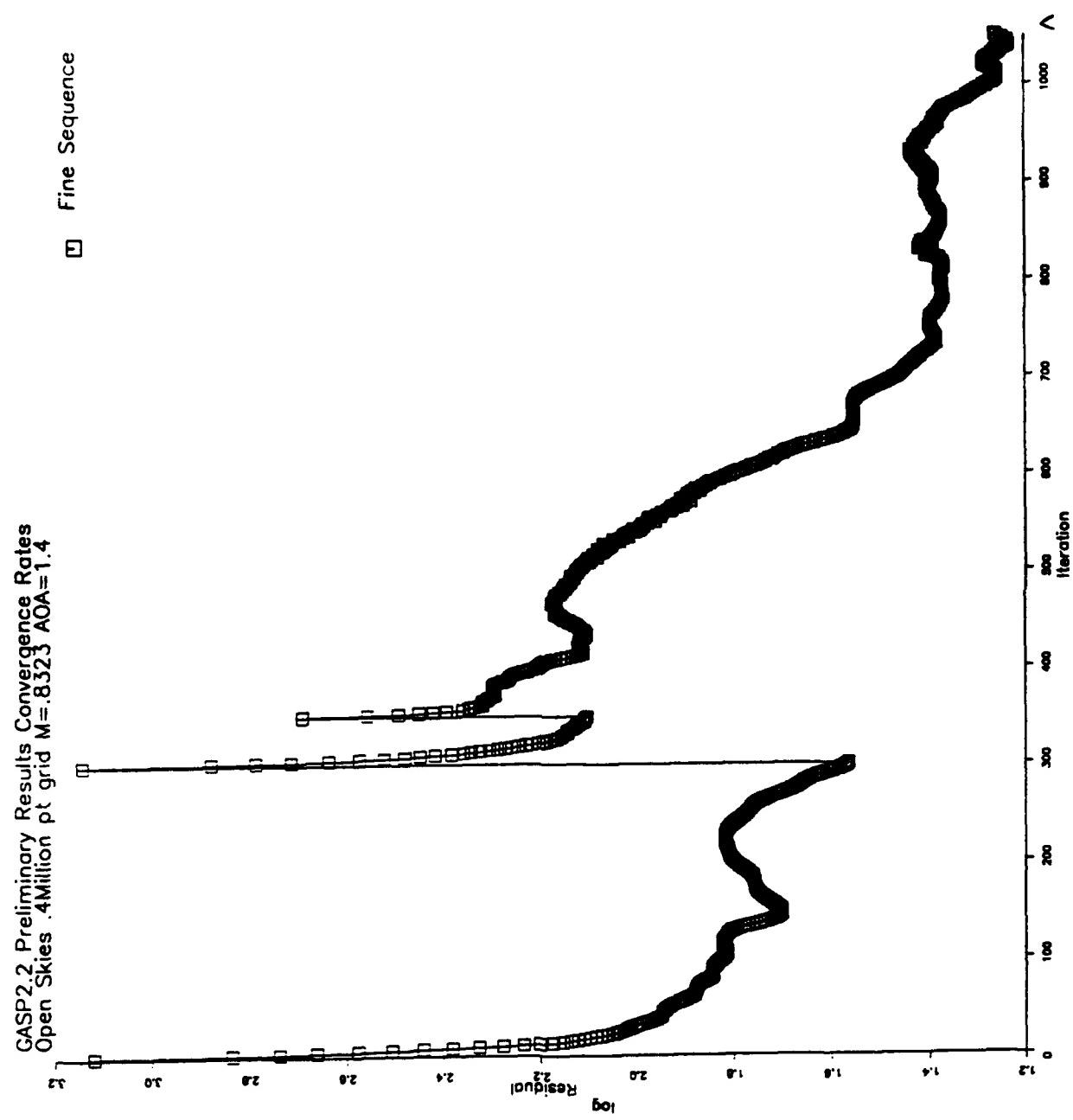
Figure 25:   GASP Convergence History on Coarse 3-D Grid

Figure 26: **GASP** Selected Boundary Layer Profiles Convergence

47

Open Skies Coarse Grid Solution
Mach .8323 AOA=1.4 Rn=60M

y+
5
4.75
4.5
4.25
4
3.75
3.5
3.25
3
2.75
2.5
2.25
2
1.75
1.5
1.25
1
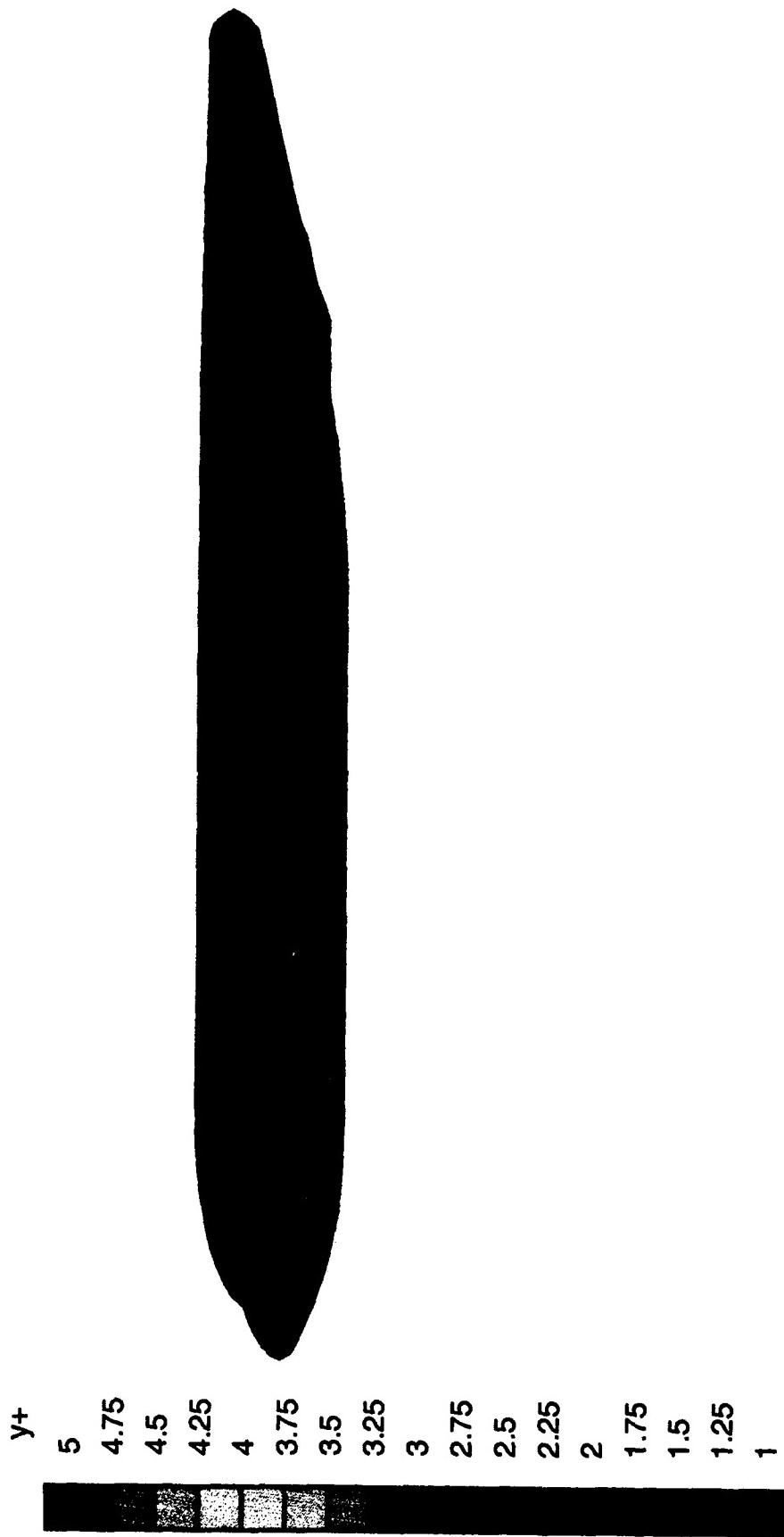
Figure '27: GASP y+ Contours, Side View
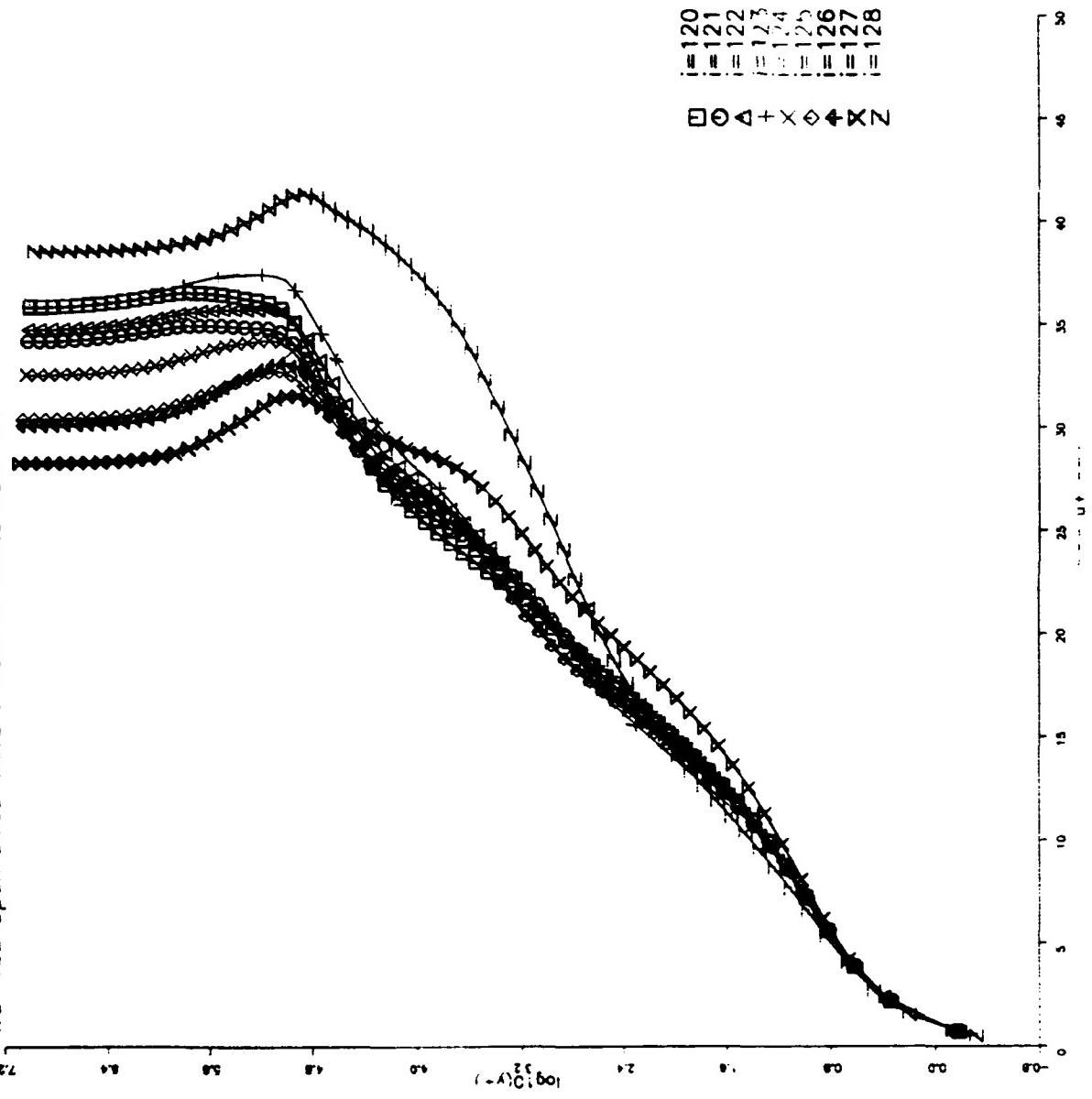
Figure 28: GASP Lower CL Boundary Layer Profiles Near the Bulkhead

49

Figure 20. GASP Pressure Schematic, Side View (Frame 810)
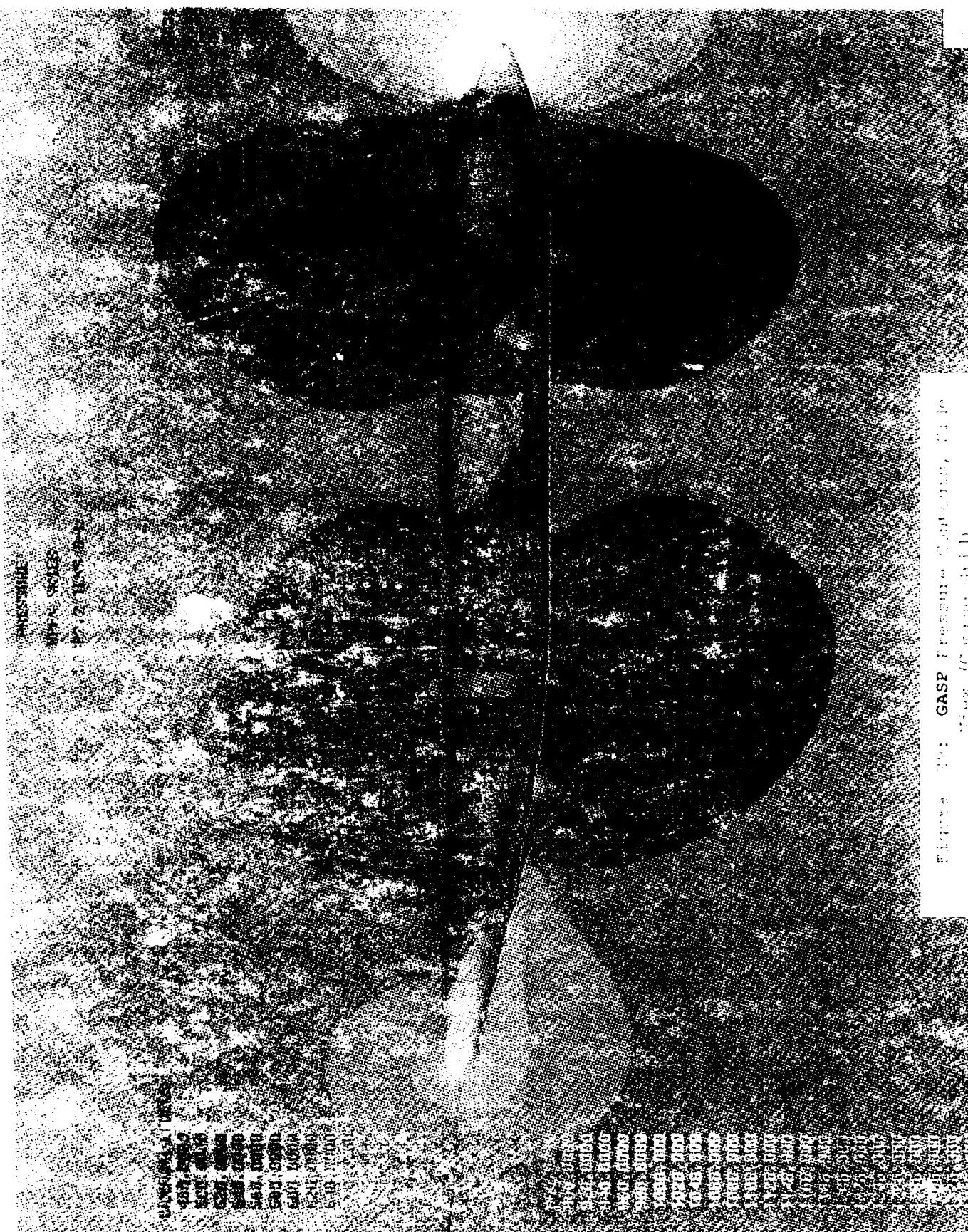
Figure 30: **GASP** Mach Contours, Side View

51
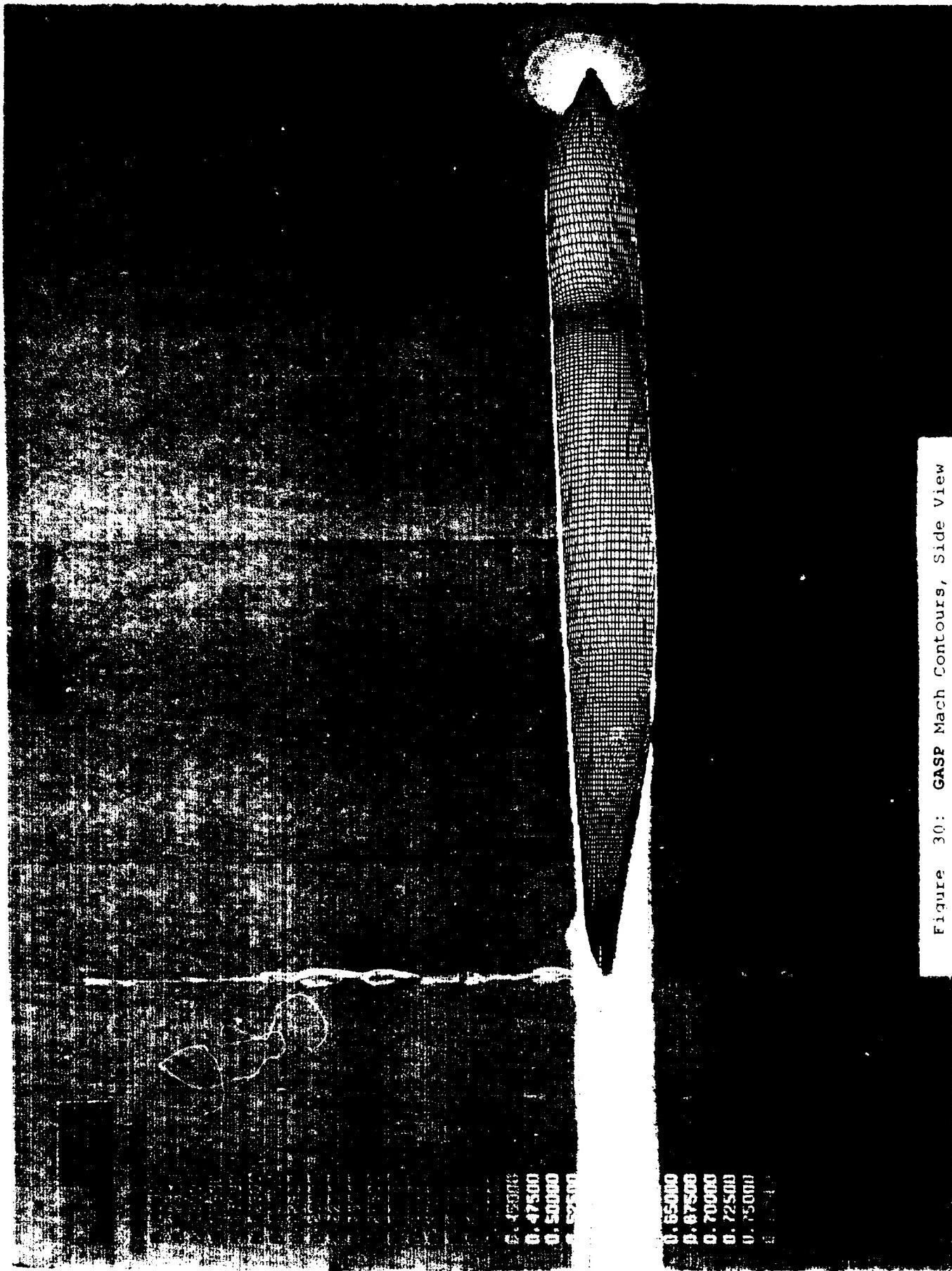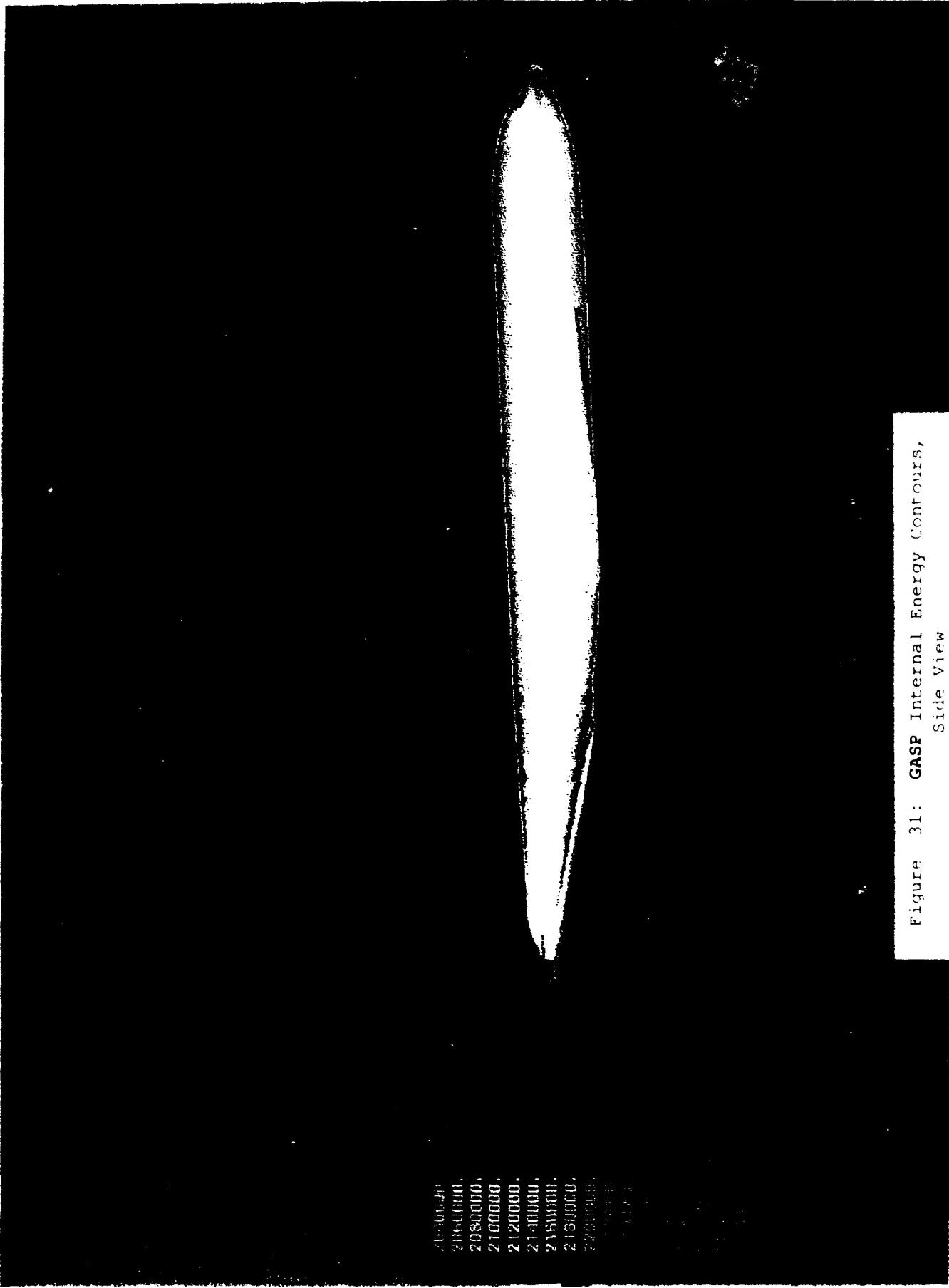
Figure 31: **GASP** Internal Energy Contours, Side View

Open Skies Coarse Grid Solution
Mach .8323 AOA=1.4 Rn=60M

Cf_k

0.004
0.00375
0.0035
0.00325
0.003
0.00275
0.0025
0.00225
0.002
0.00175
0.0015
0.00125
0.001
0.00075
0.0005
0.00025
0
-0.00025
-0.0005
-0.00075
-0.001

Figure 32: GASP C_z Contours, Side View

53
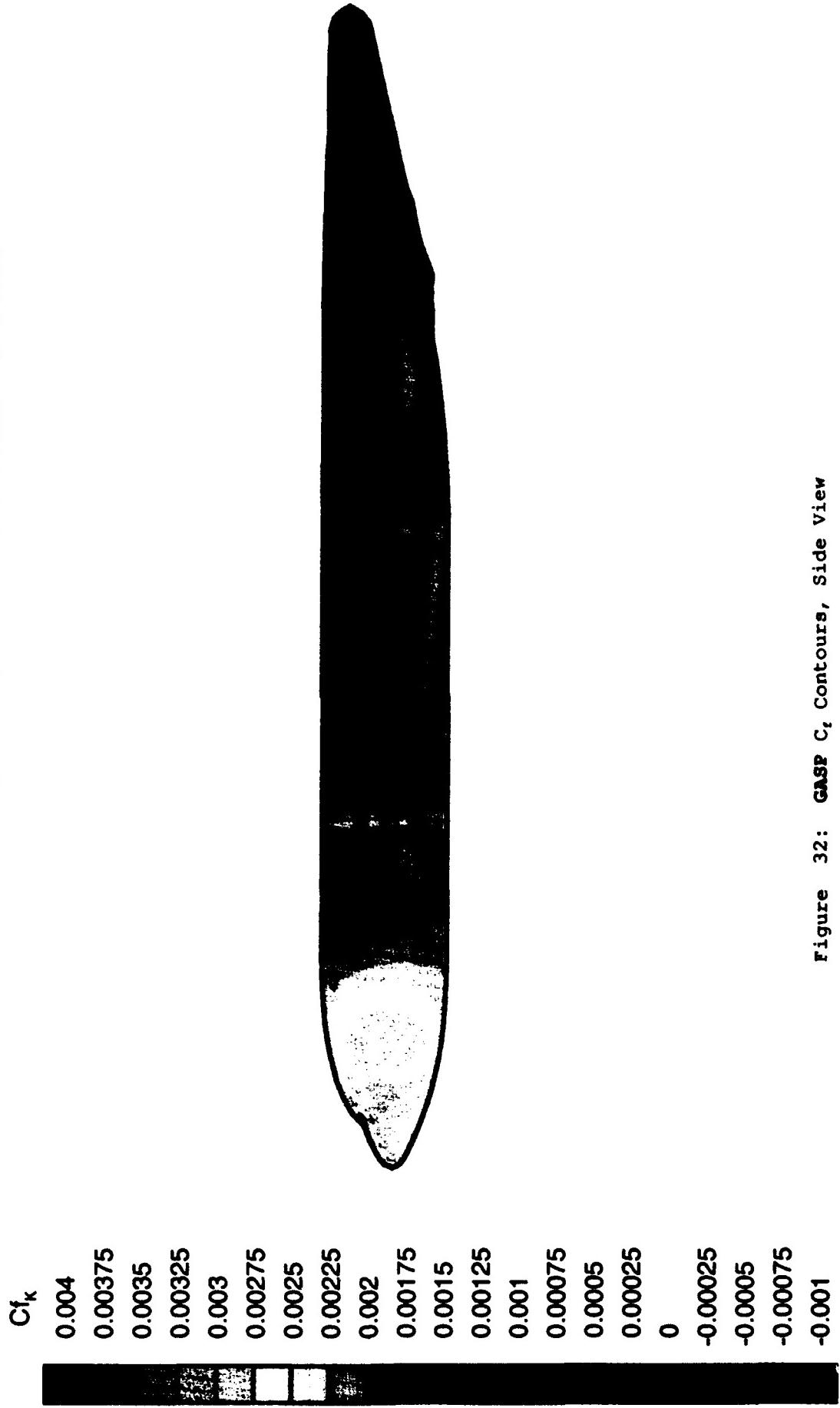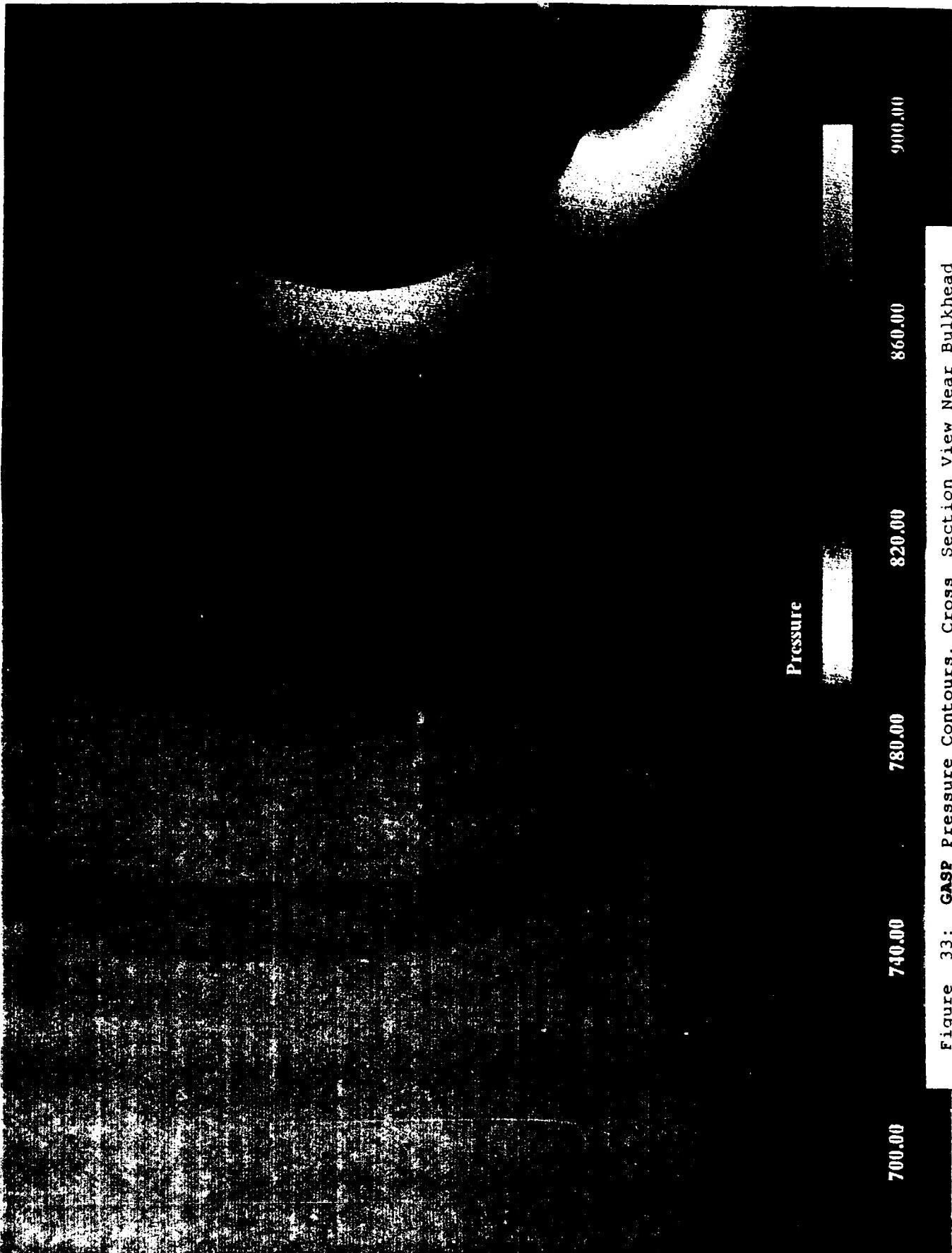
Figure 33: **GASP** Pressure Contours, Cross Section View Near Bulkhead

Pressure

700.00   740.00   780.00   820.00   860.00   900.00

Figure 24: GASP Mach contours, close-up, with fine grid refinement

55
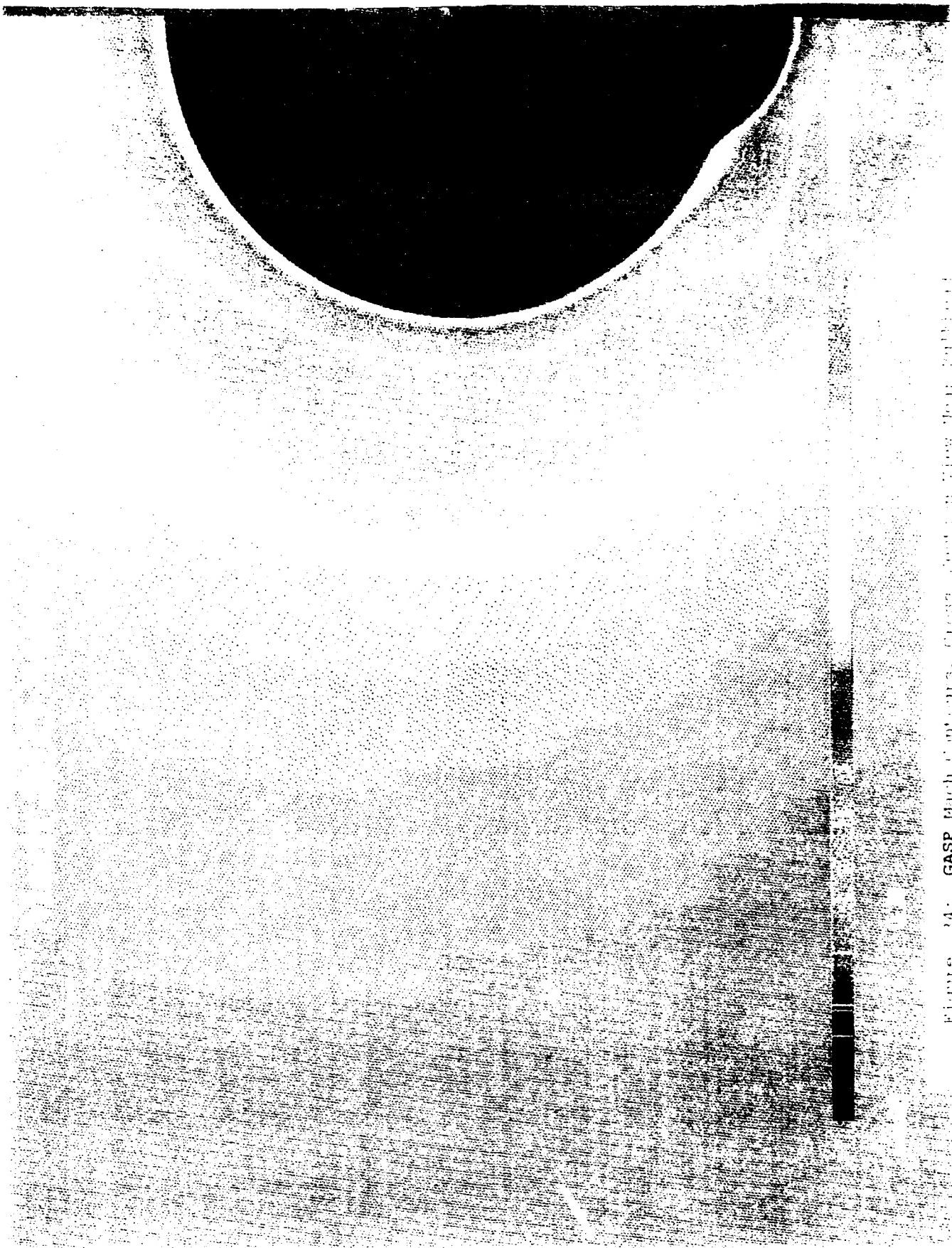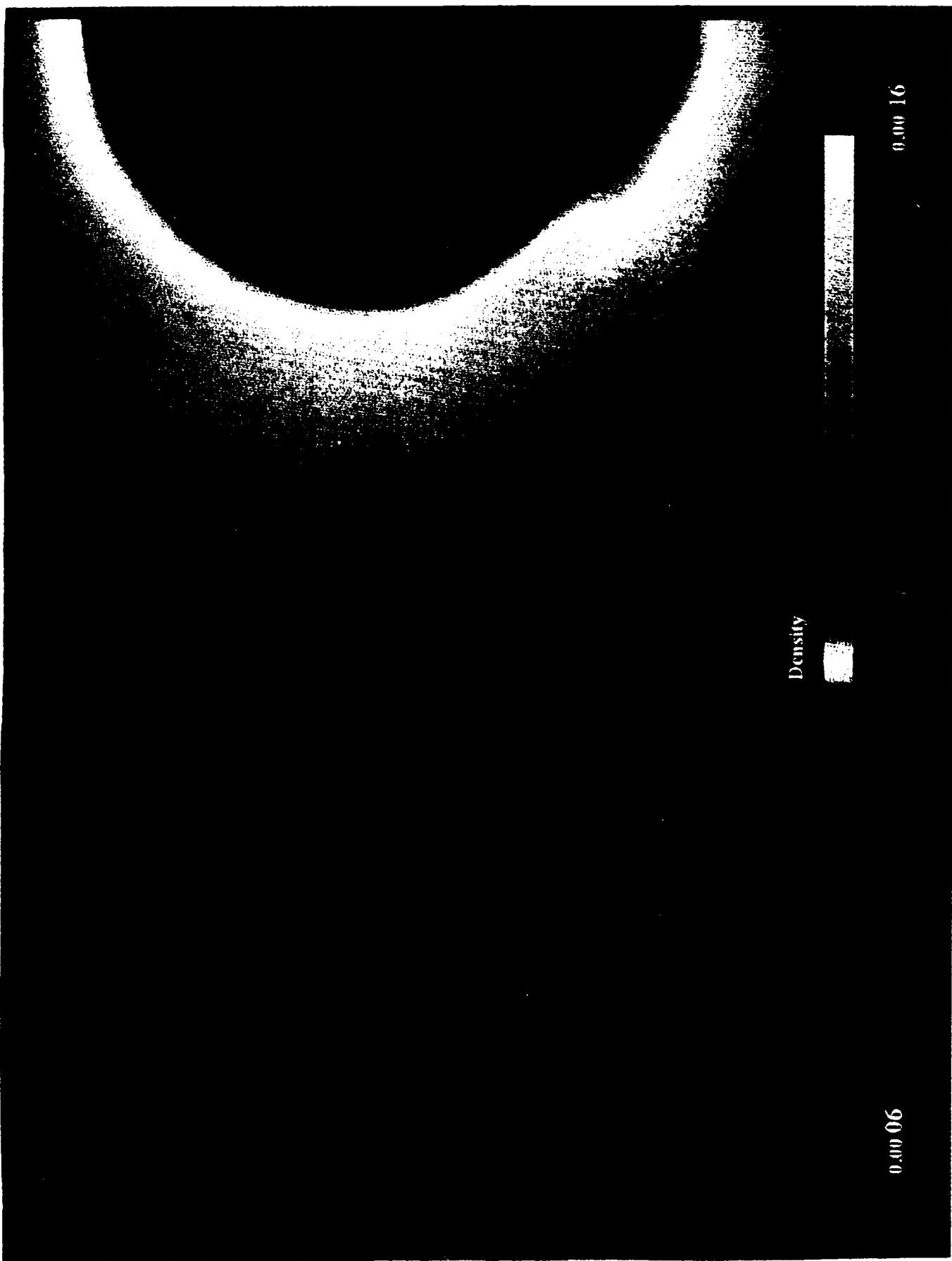
Figure 35: **GASP** Density Contours, Cross Section View Near Bulkhead
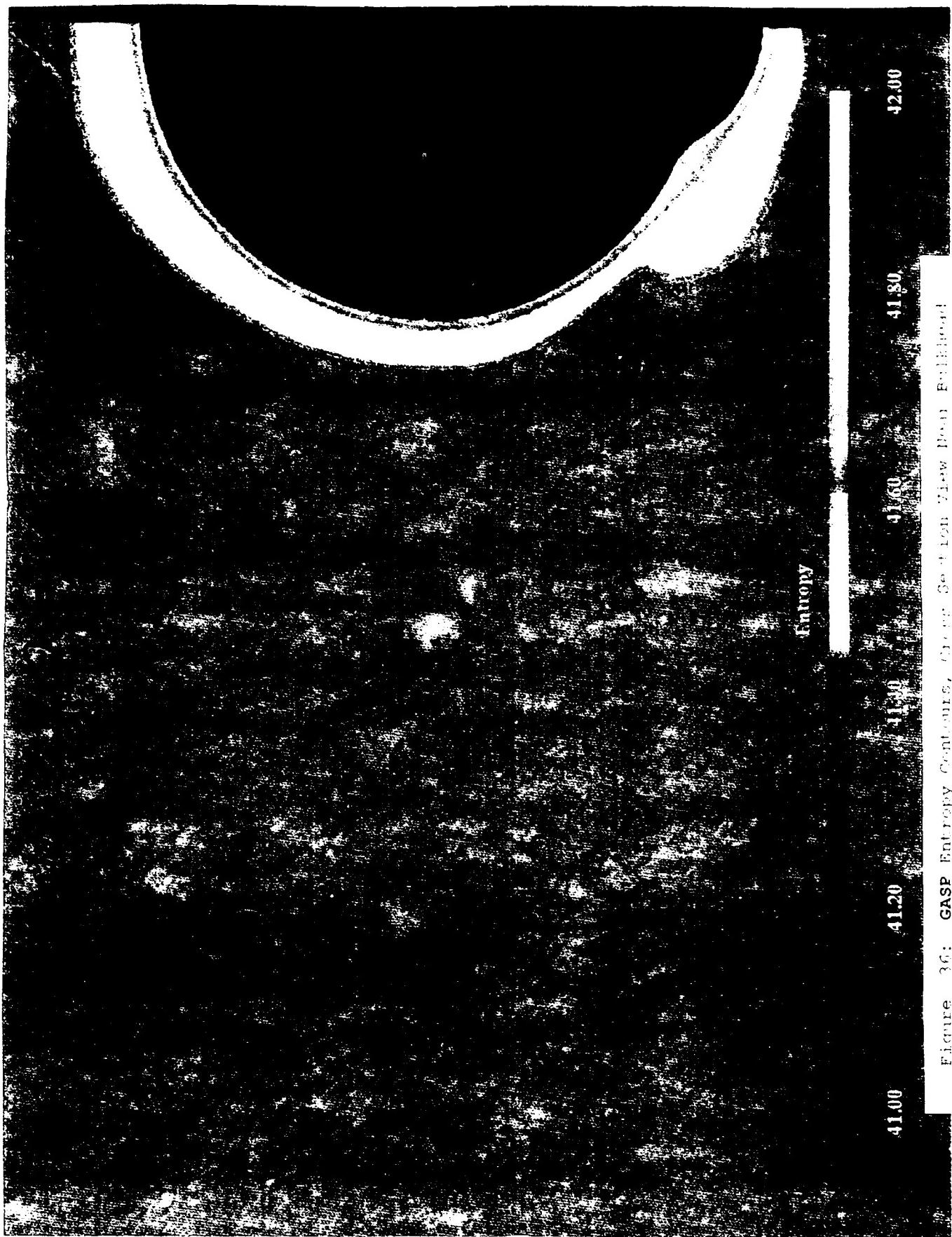
Figure 36: GASP Entropy Contours, Cross Section View Port Bulkhead

Open Skies
Mach .8323 AOA=1.4 deg, Rn=60,M
Crossflow Velocity Field
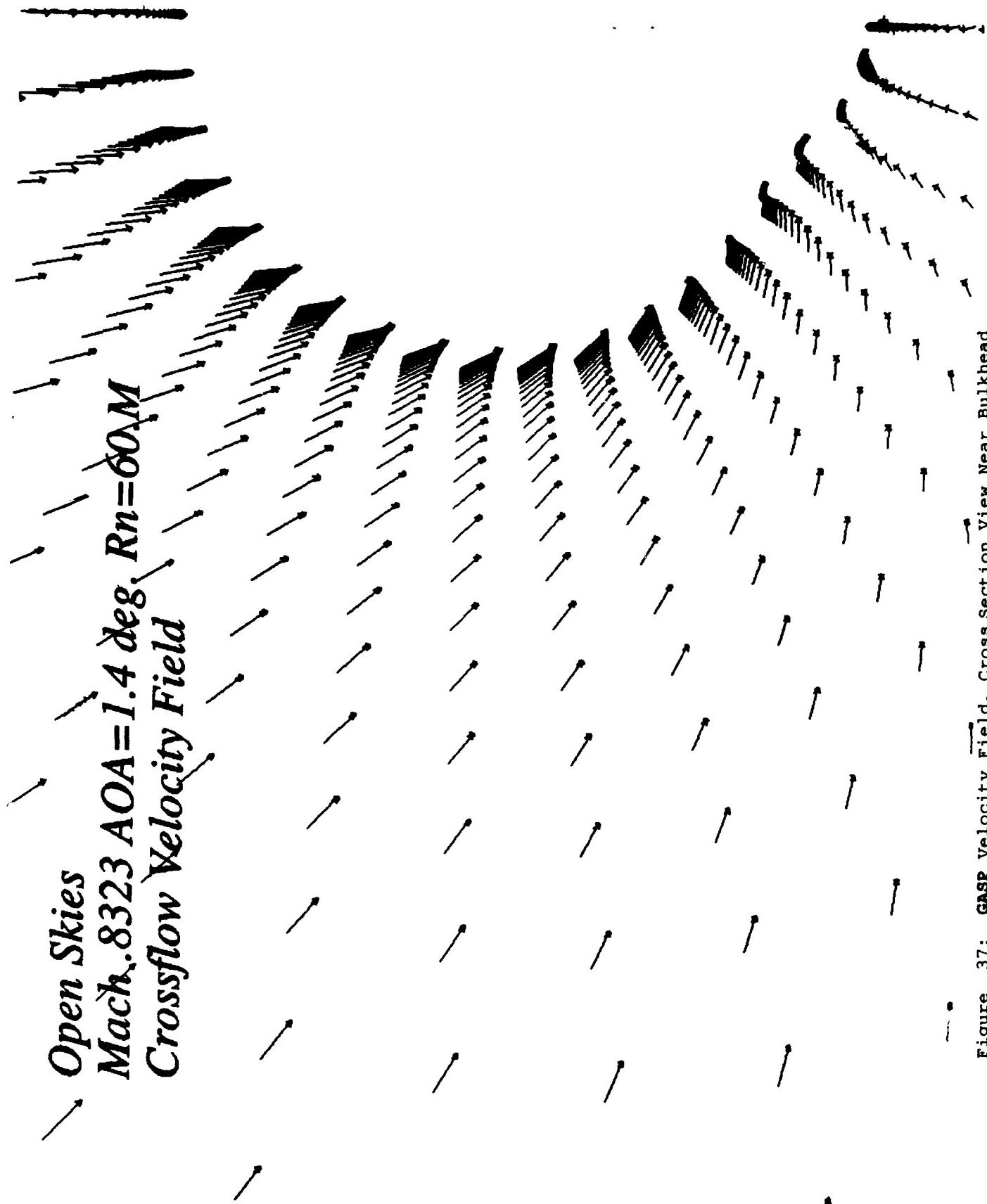
Figure 37: **GASP** Velocity Field, Cross Section View Near Bulkhead
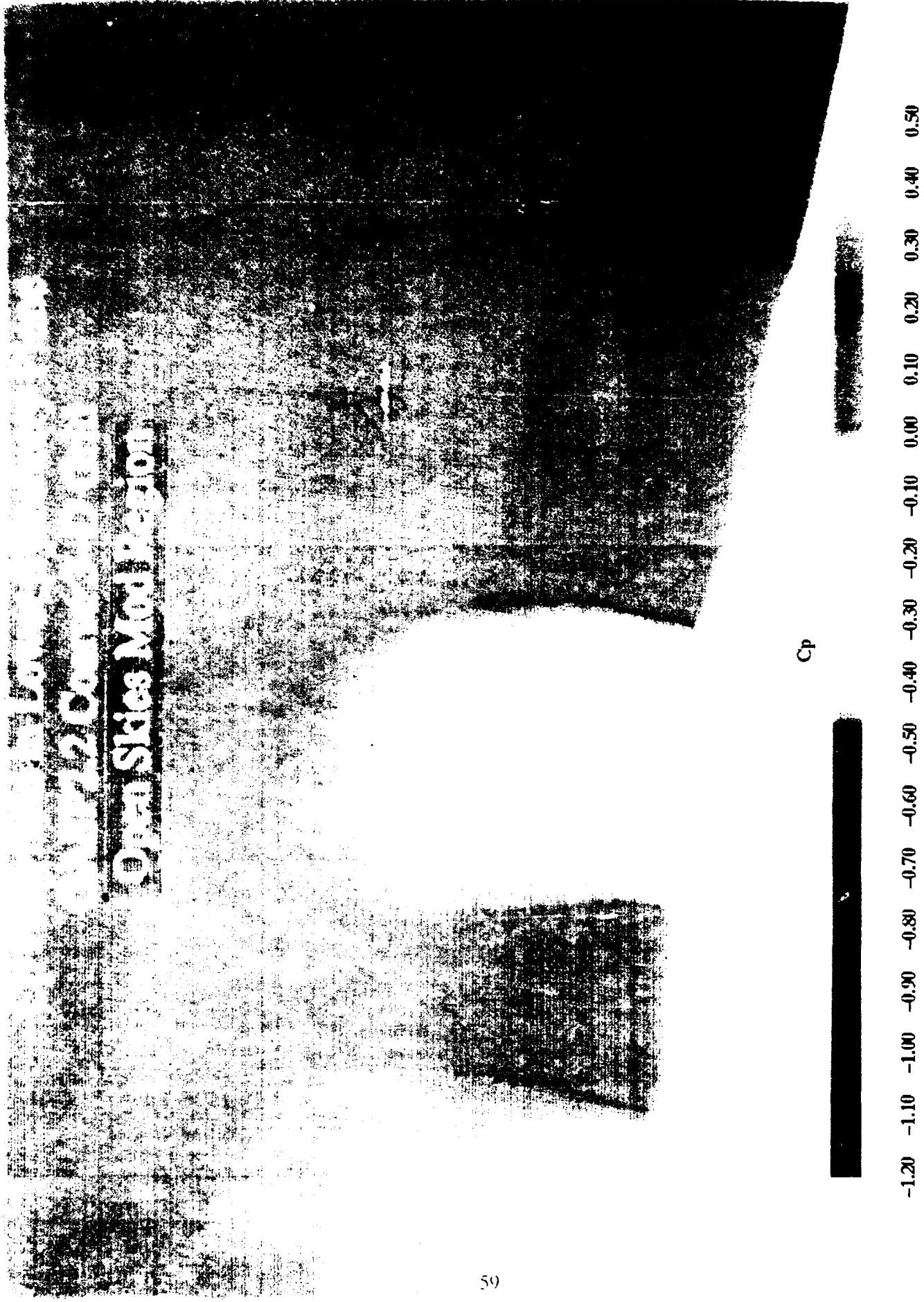
Figure 38: **GASP** C_p Contours, Lower Symmetry Plane
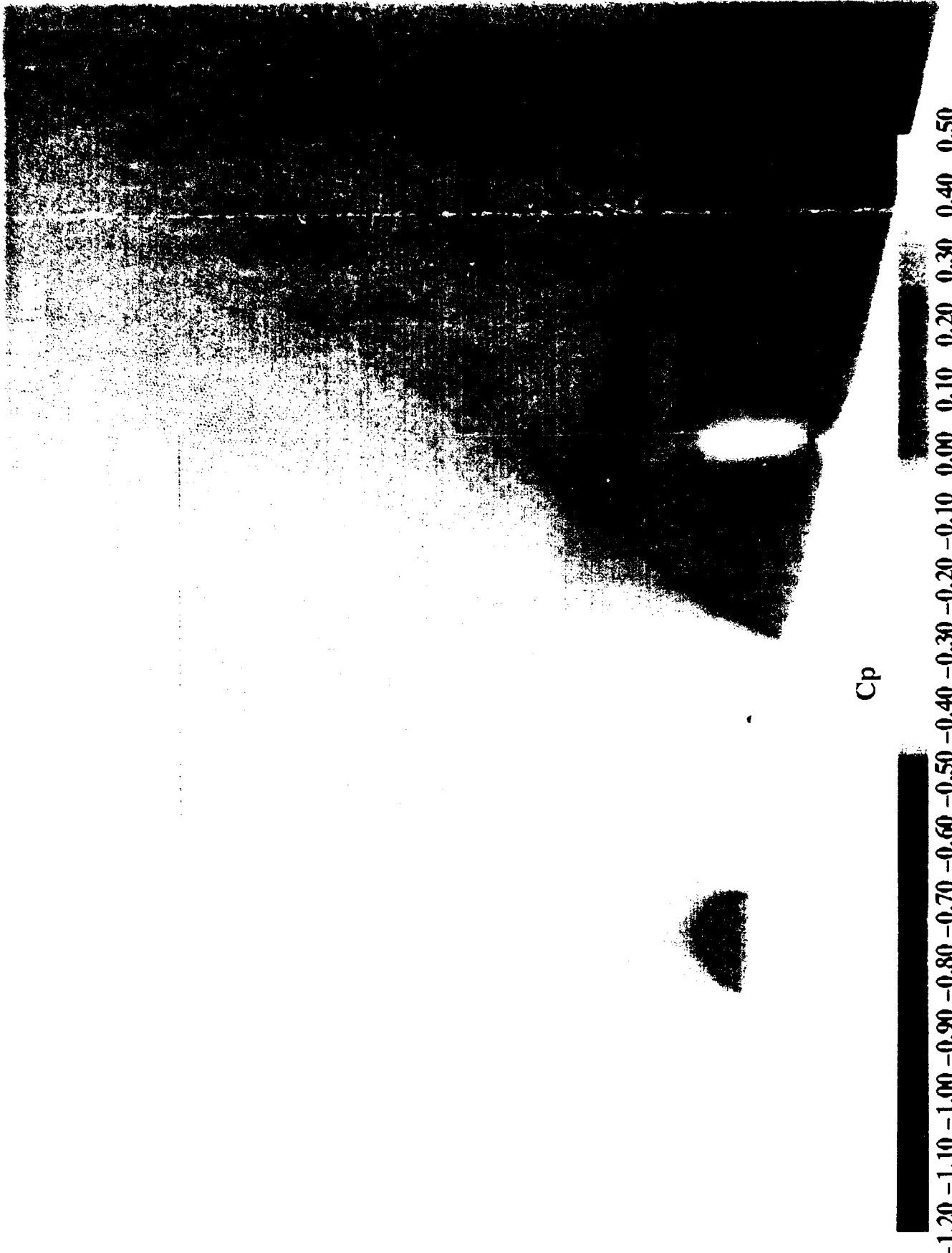
Figure 39: **NASTD** C_p Contours, Lower Symmetry Plane

Cp

-1.20 -1.10 -1.00 -0.90 -0.80 -0.70 -0.60 -0.50 -0.40 -0.30 -0.20 -0.10 0.00 0.10 0.20 0.30 0.40 0.50

Figure 40: **GASP** Mach Contours, Lower Symmetry Plane

Mach

0.00   0.32   0.64   0.96   1.28
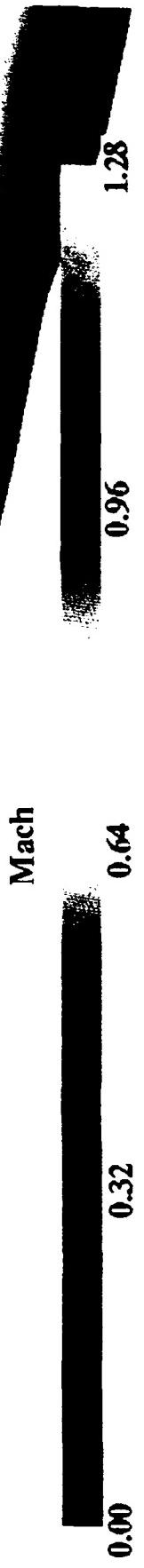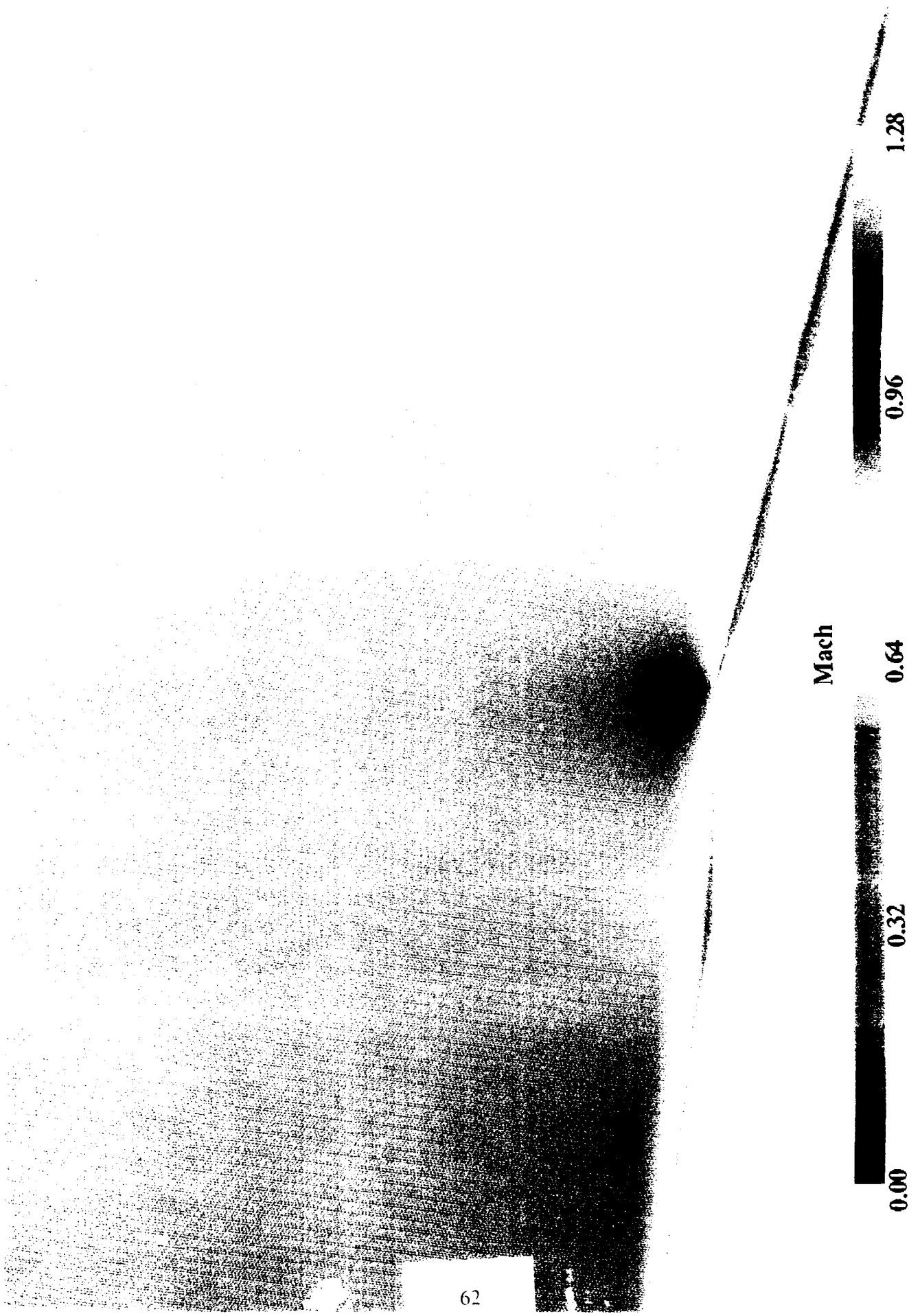
Figure 41: **NASTD** Mach Contours, Lower Symmetry Plane

62
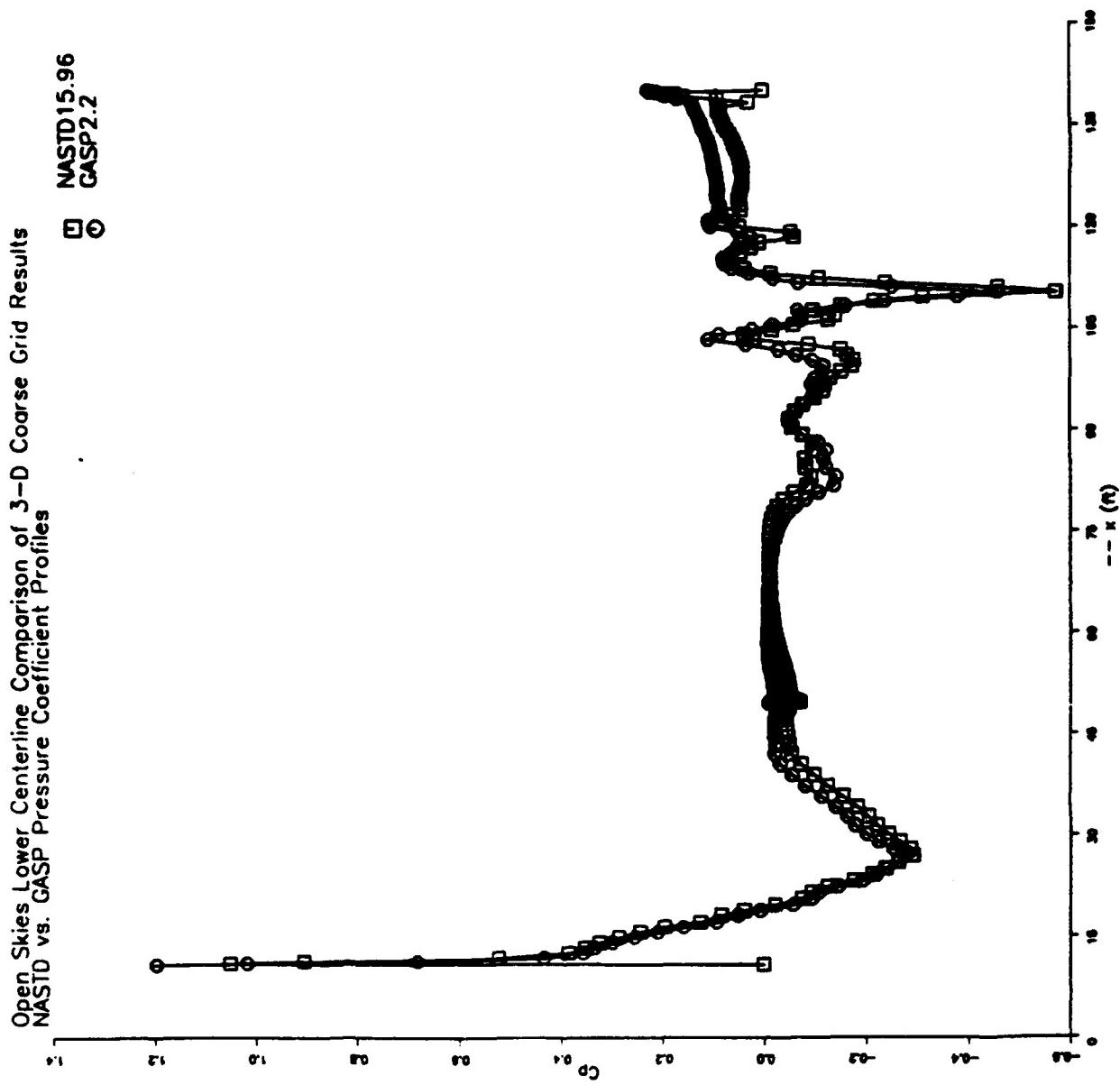
Figure 42: **NASTD vs. GASP Lower Centerline C_p Comparison**

Open Skies Lower Centerline Comparison of 3-D Coarse Grid Results
NASTD vs. GASP Skin Friction Coefficient Profiles
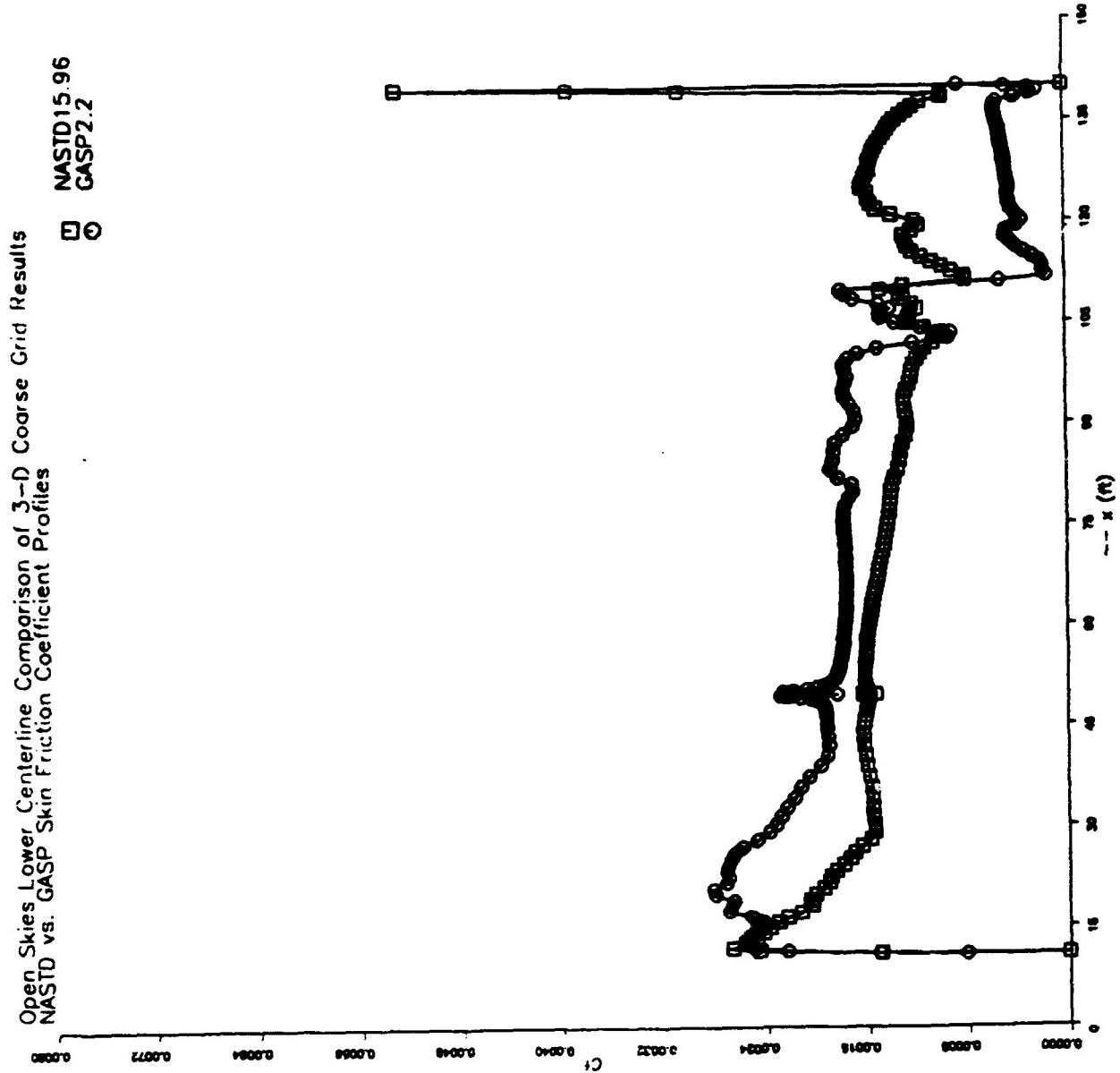
Figure 43: NASTD vs. GASP Lower Centerline C_f Comparison
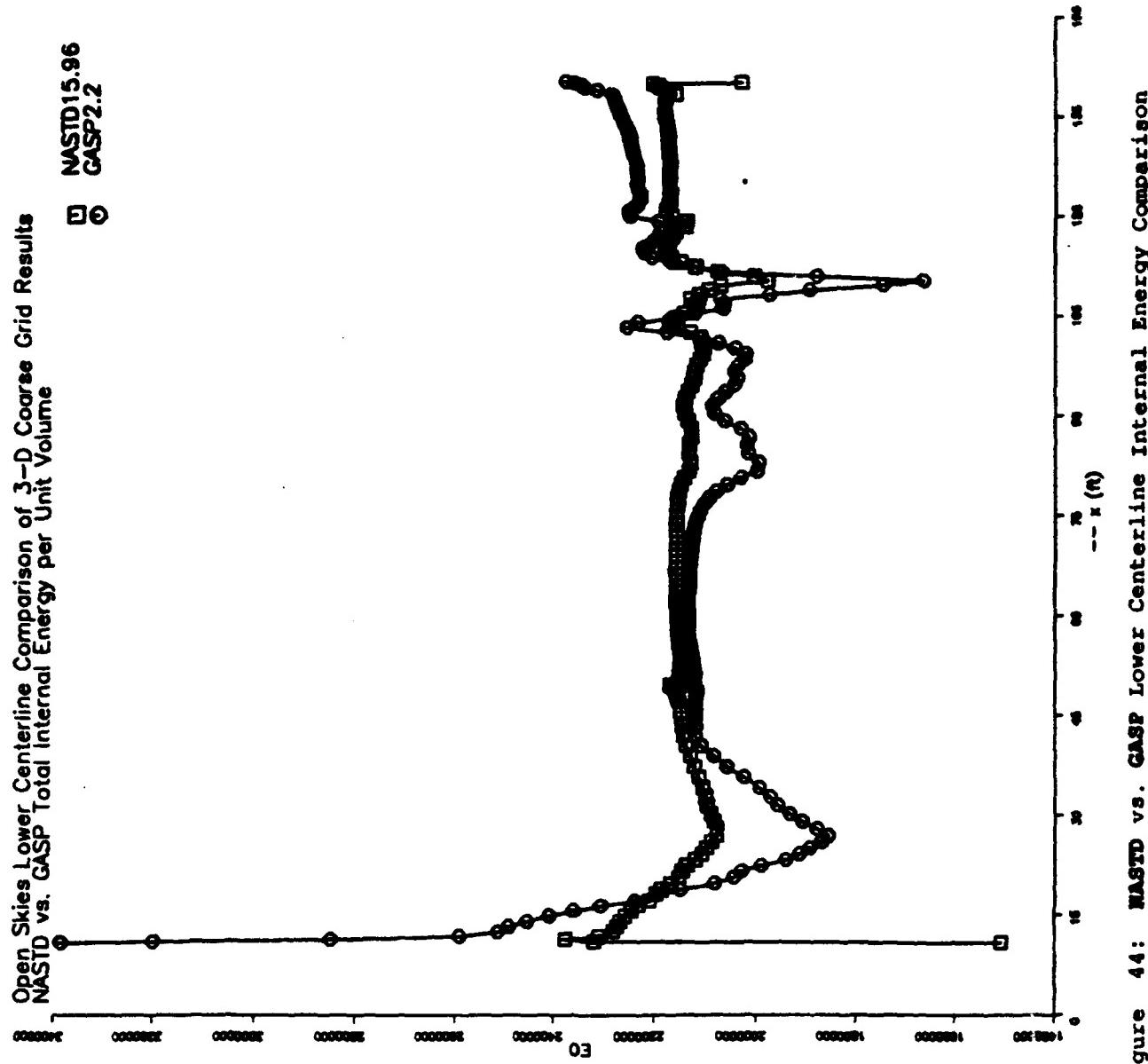
Figure 44: NASTD vs. GASP Lower Centerline Internal Energy Comparison

Convergence History for NASTD Coarse 3-D Grid Simulation
Full Navier–Stokes with Baldwin–Lomax

Coarse Grid
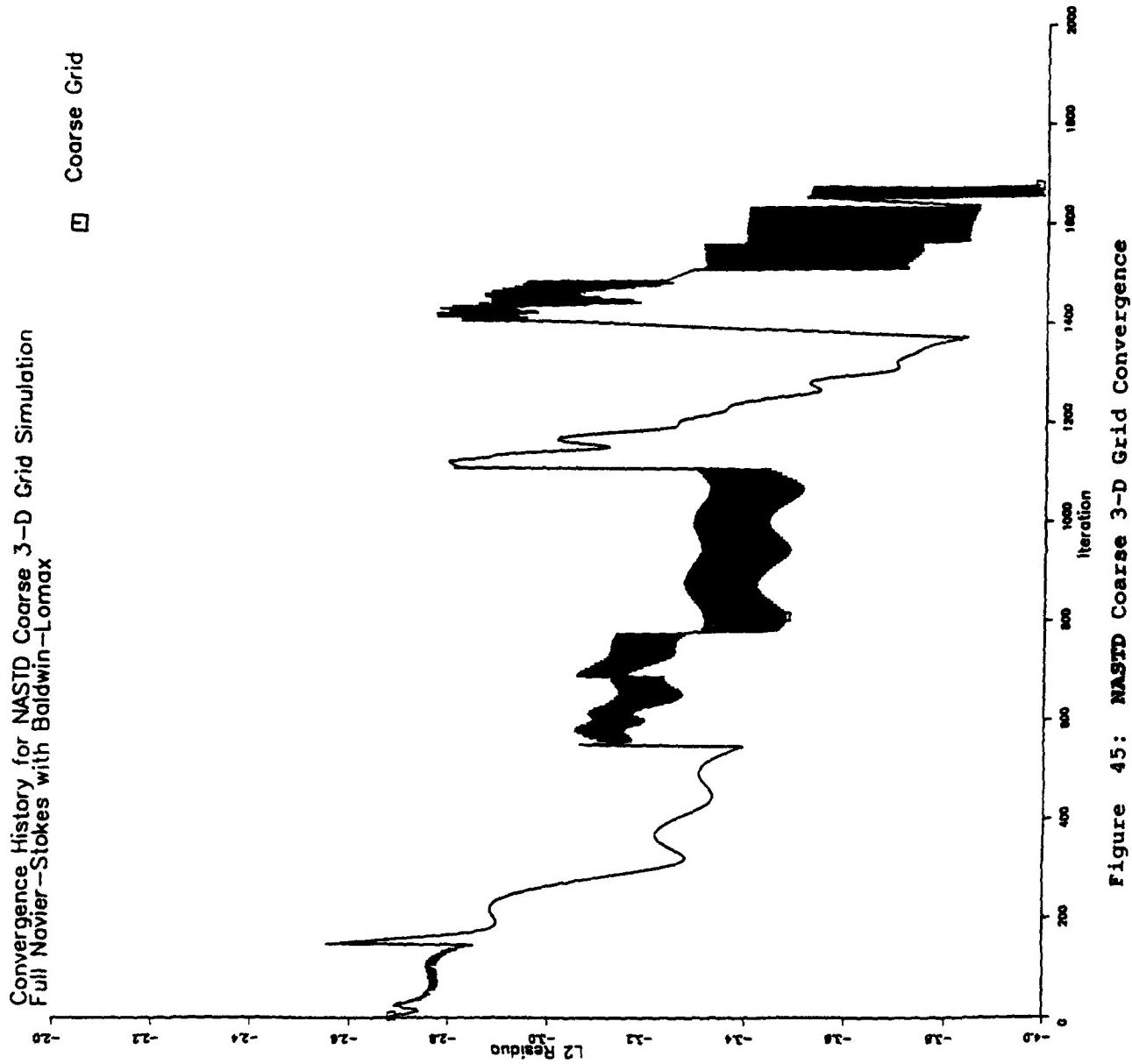
Figure 45: NASTD Coarse 3-D Grid Convergence

66
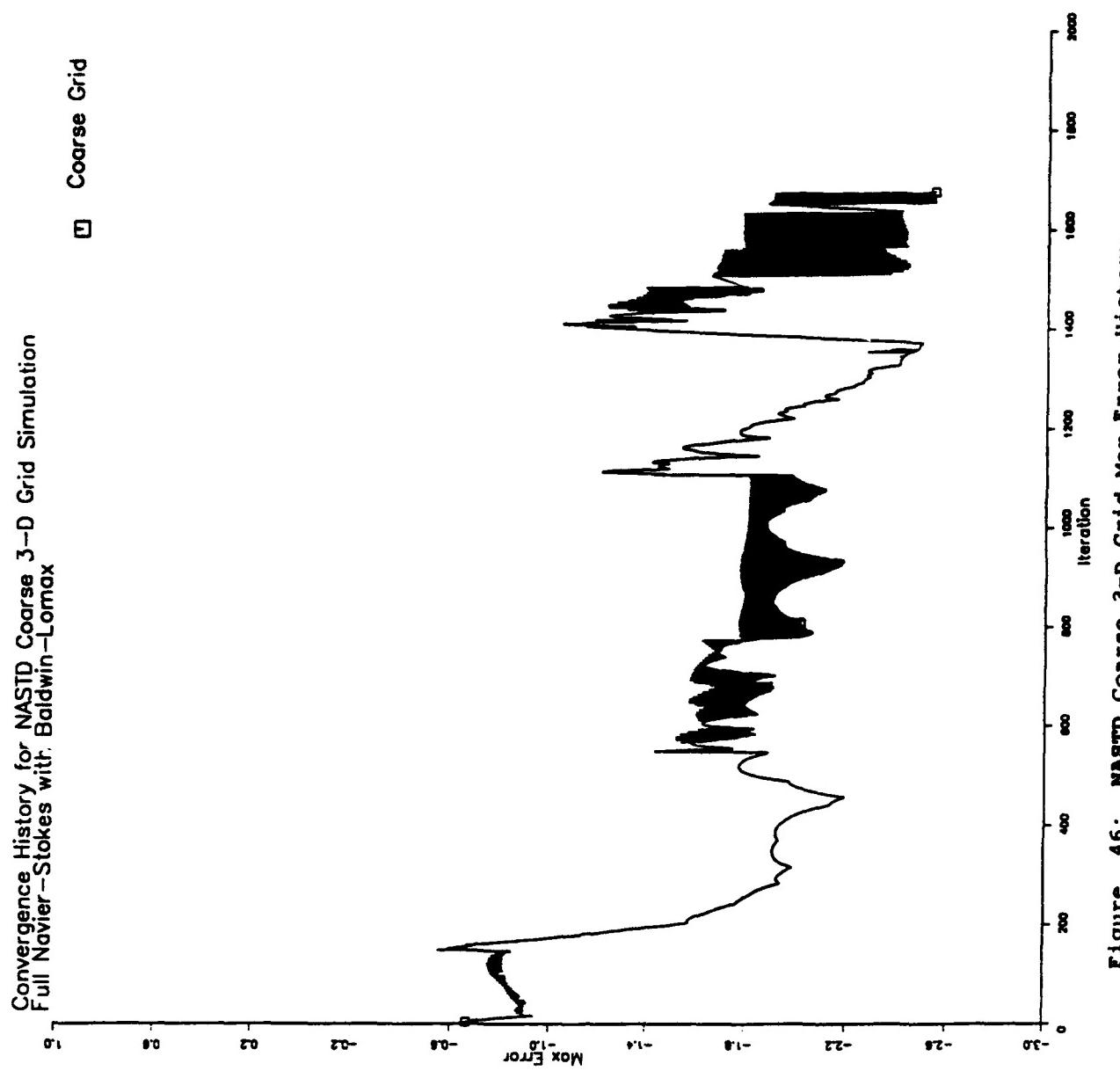
Figure 46: NASTD Coarse 3-D Grid Max Error History

67

Table 2: Cray II Cost Projections for GASP

FNS k-ε	FNS B-L	TLNS B-L	Grid
		$770.	2-D Coarse Baseline (actual)
$6700.			2-D Fine Baseline
$6700.			2-D Fine Alternative Fairing
		$15,000.	3-D Coarse Baseline (actual)
$168,360.	$56,120.		3-D Fine Baseline
$168,360.	$56,120.		3-D Fine Alternative Fairing

The remainder of the simulations were performed with the **NASTD** program on the local Cray **XMP**.

7.7 Coarse 2-D Results:

The 2-D option was tried since the modification region (flat plate) is locally 2-D. This, however, proved to be too limiting a mass flow constraint to provide a representative flowfield. It overpredicted the shock strength compared to the axisymmetric results. Figures 47 and 48 present views of the grid. Figures 49 and 50 show the convergence rates for the run. Figures 51 and 52 present the pressure and Mach number flowfield results obtained.

7.8 Coarse Axisymmetric Results:

The axisymmetric case was considered slightly more severe than the full 3-D case (because of the absence of curvature effects). Figures 53 and 54 present the residual convergence rates. Figures 55 and 56 depict the pressure and Mach number flowfields respectively. The velocity vectors indicate a region of recirculation on the aft side of the pod. The results indicated the presence of a
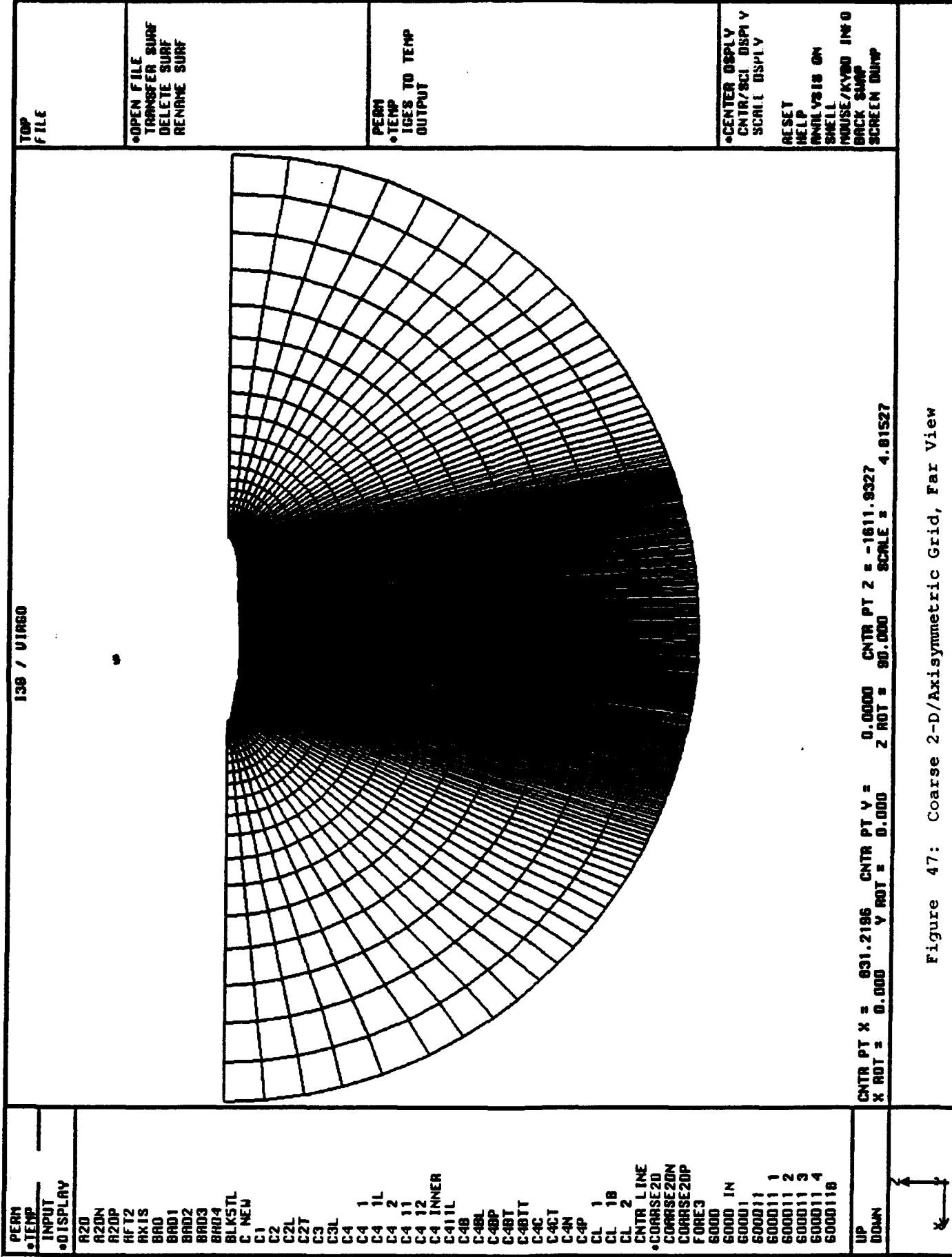
Figure 47: Coarse 2-D/Axisymmetric Grid, Far View
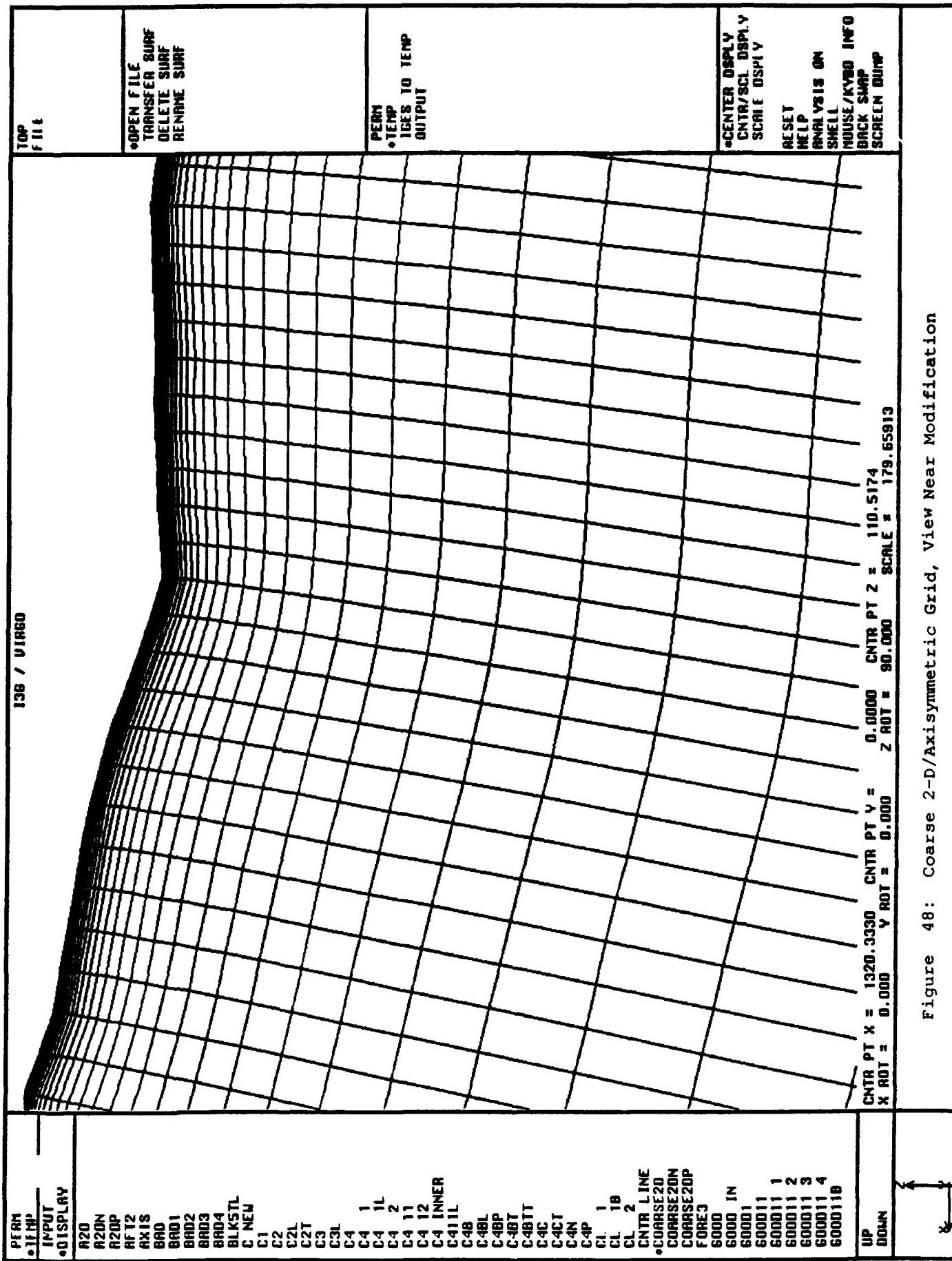
Figure 48: Coarse 2-D/Axisymmetric Grid, View Near Modification

Convergence History for NASTD Coarse 2-D Grid
Full Navier-Stokes with Baldwin-Lomax, 1st order Roe, Unlimited
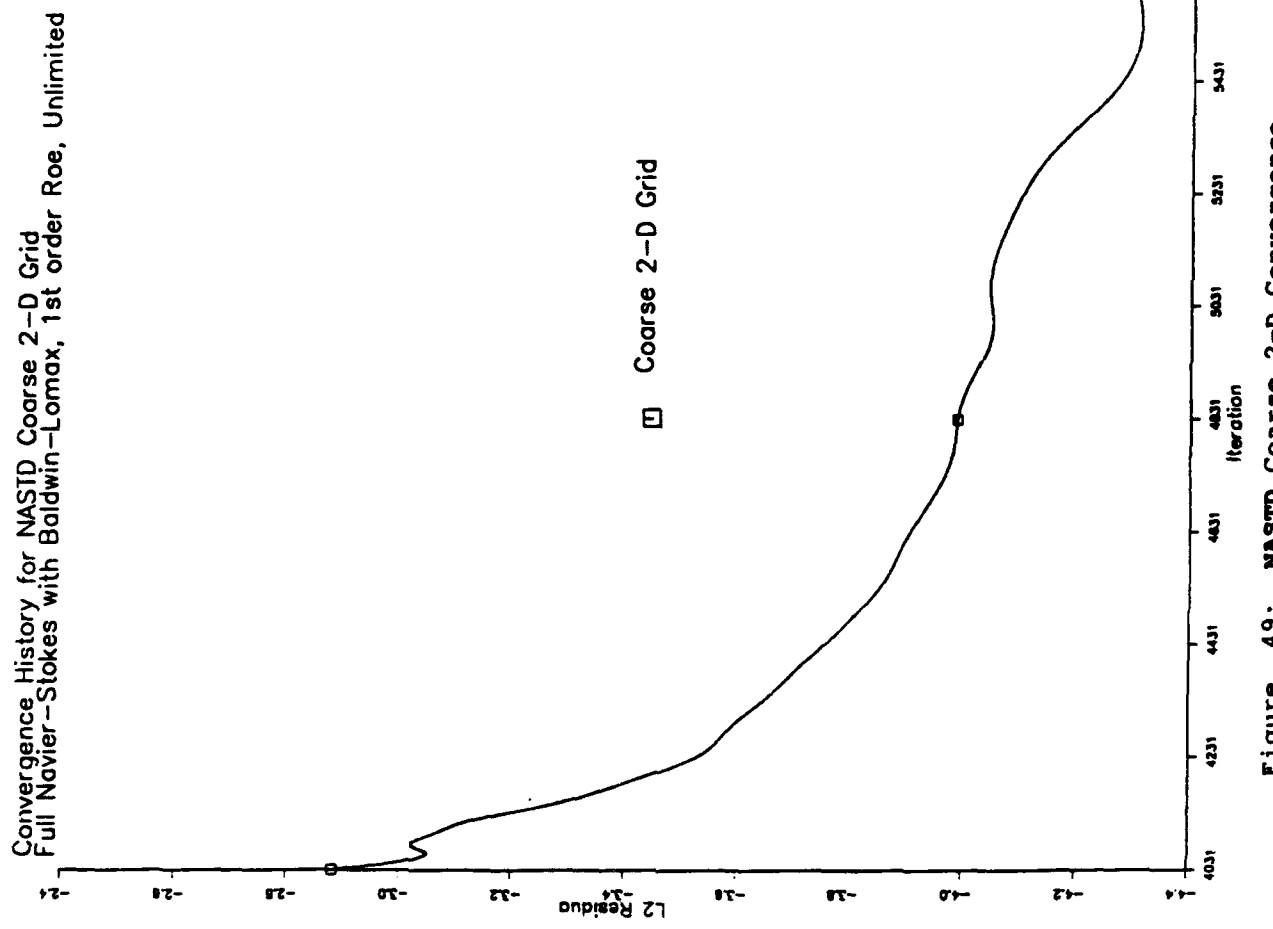
Figure 49: NASTD Coarse 2-D Convergence

71

Convergence History for NASTD Coarse 2-D Grid
Full Navier-Stokes with Baldwin-Lomax, 1st order Roe, Unlimited
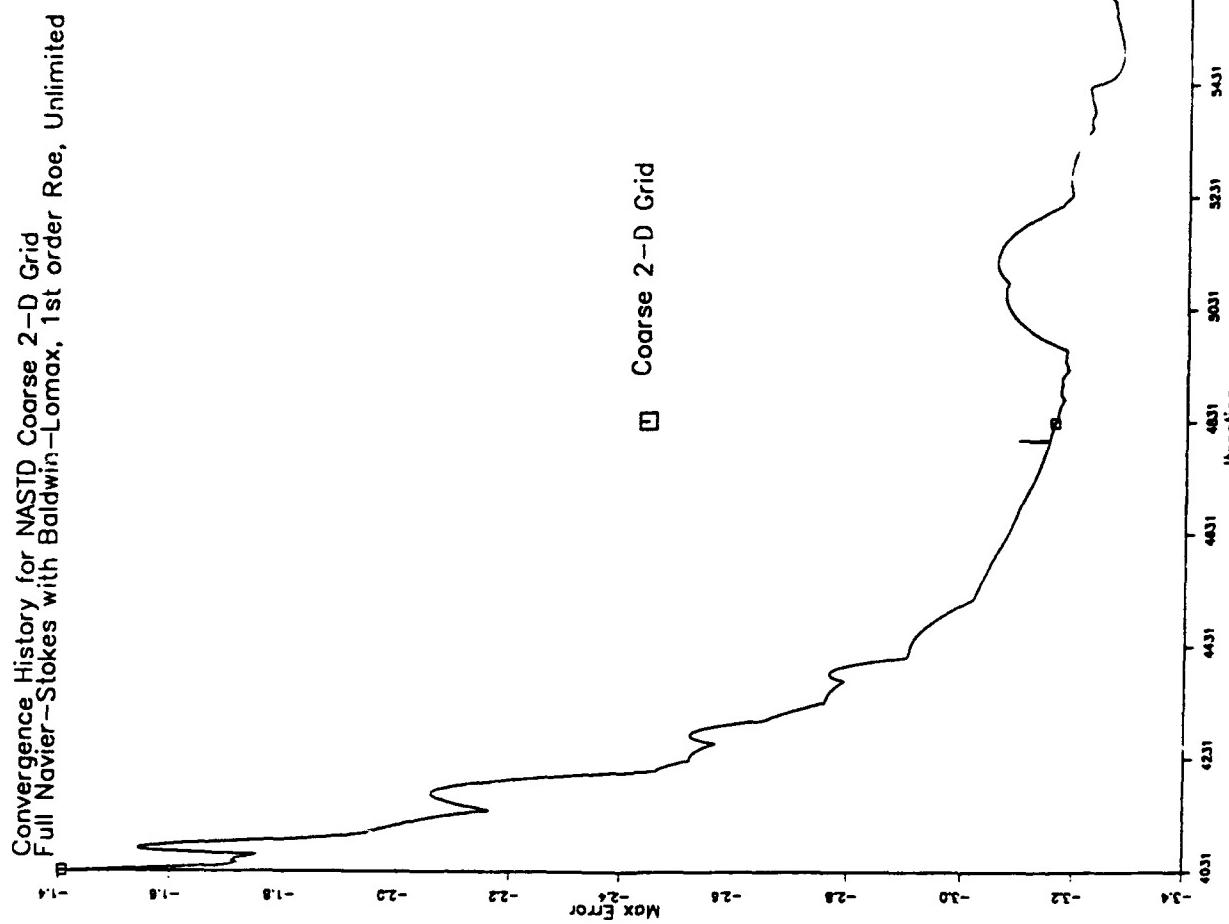

Figure 50: NASTD Coarse 2-D Max Error History

72

Cp

0.50

−0.35

−1.20

Figure 91: NASTD C_p Contours, Coarse 2-D

Mach

0.00　　　　0.64　　　　1.28

Figure 52: NASTD Mach Contours, Coarse 2-D

Convergence History for NASTD Coarse 2-D Axisymmetric Grid
Full Navier-Stokes with Baldwin-Lomax, 1st order Roe, Unlimited
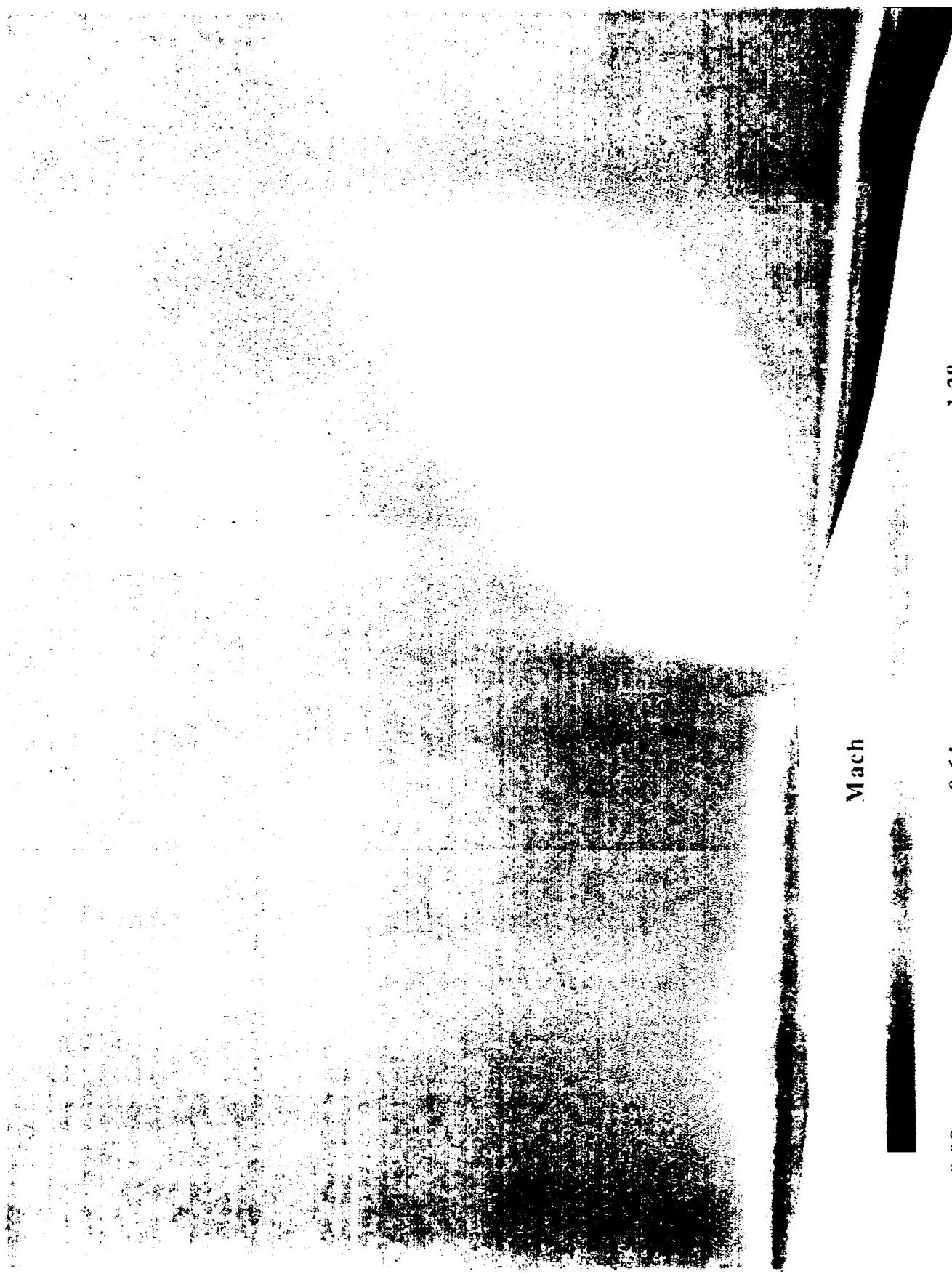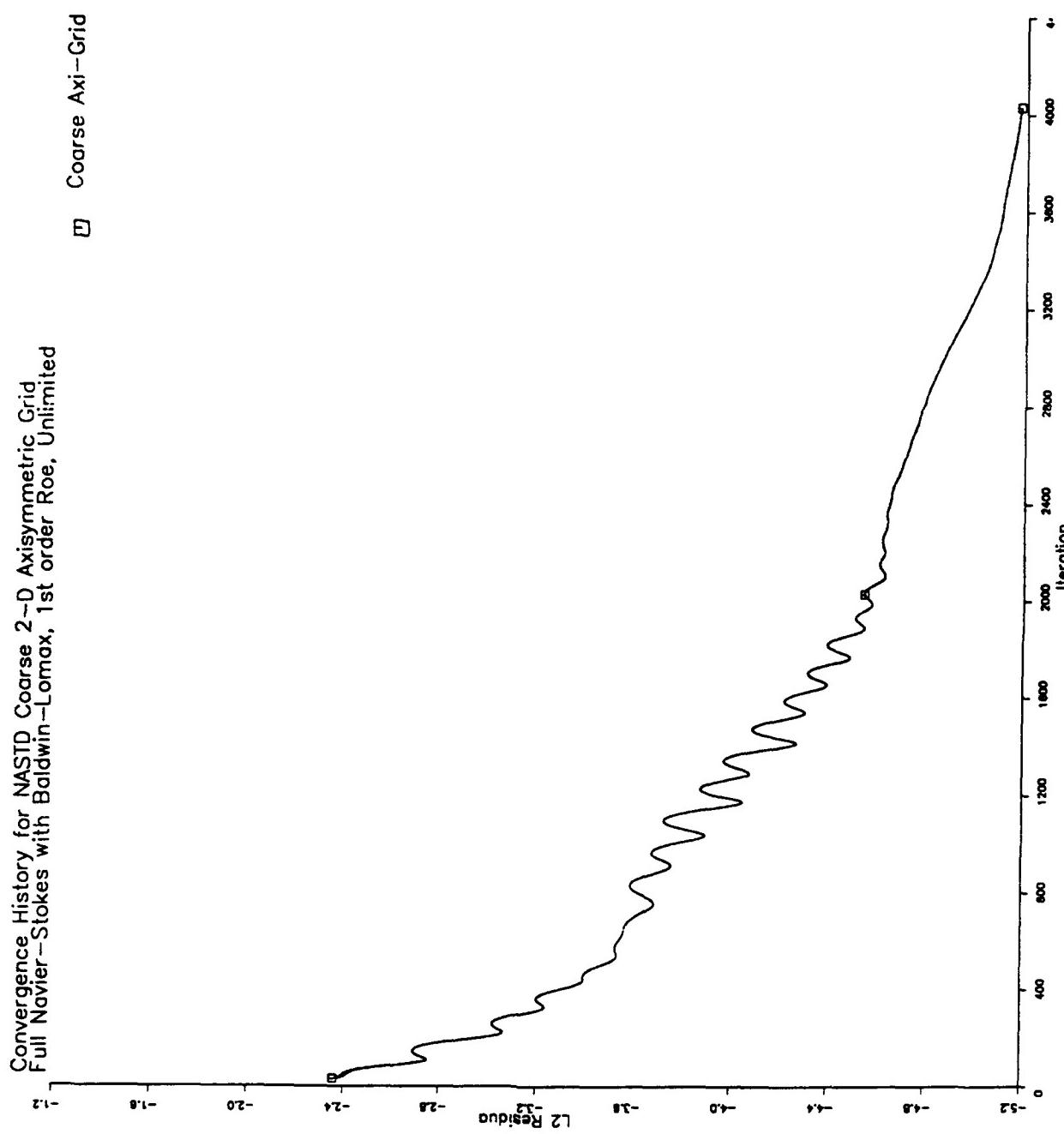
☐ Coarse Axi-Grid

Figure 53: **NASTD** Coarse Axisymmetric Convergence

Convergence History for NASTD Coarse 2-D Axisymmetric Grid
Full Navier-Stokes with Baldwin-Lomax, 1st order Roe, Unlimited
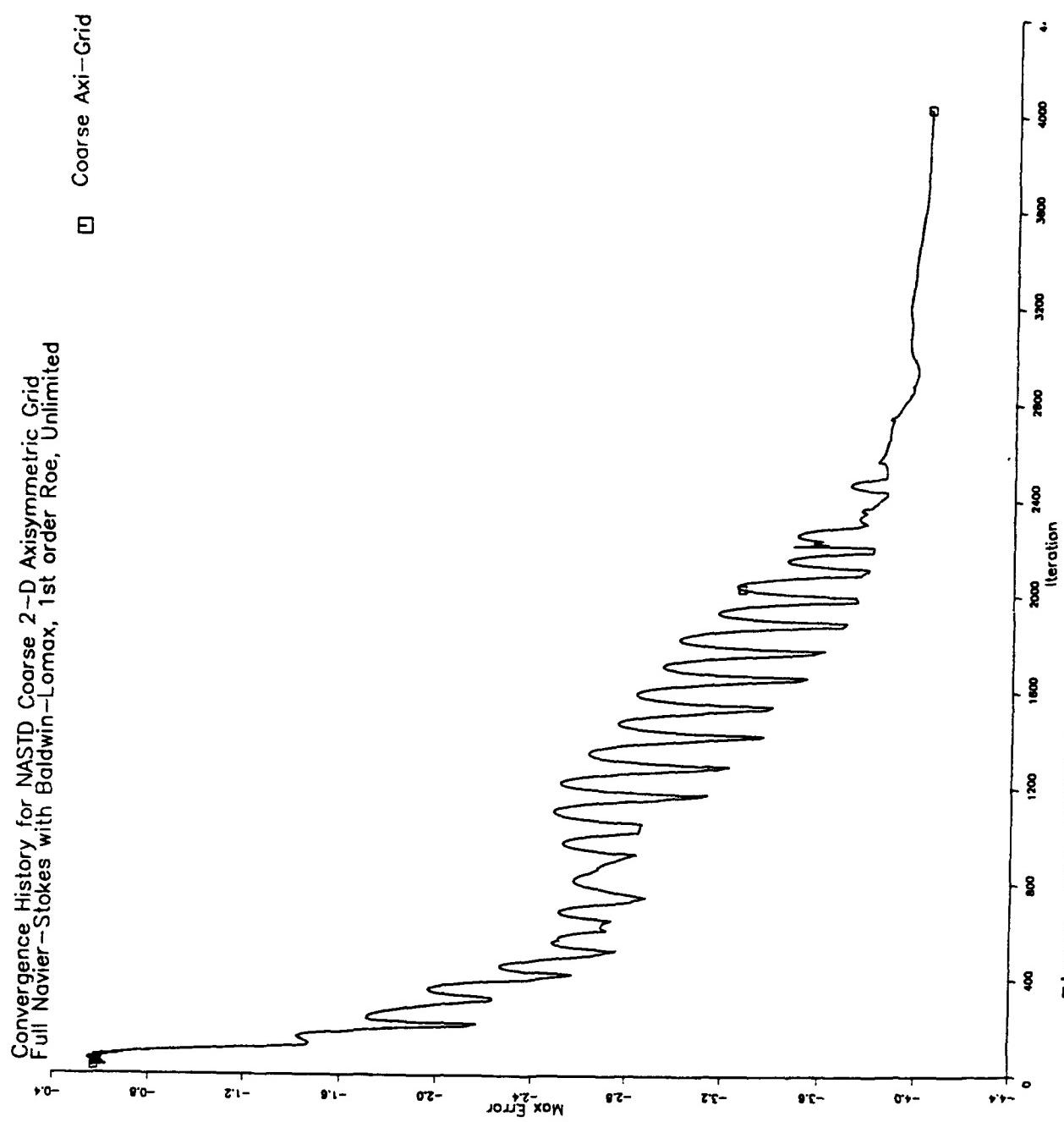
□ Coarse Axi-Grid

Figure 54: NASTD Coarse Axisymmetric Max Error History
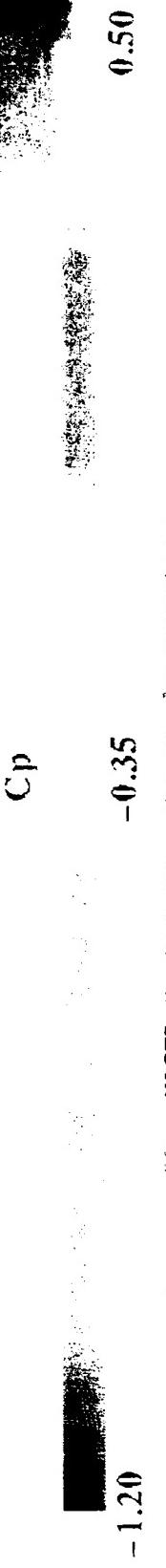
Cp

0.50

−0.35

−1.20

NASTD

Mach

| 0.00 | 0.26 | 0.51 | 0.77 | 1.02 | 1.28 |

Figure 56: **NASTD** Mach Contours, Coarse Axisymmetric
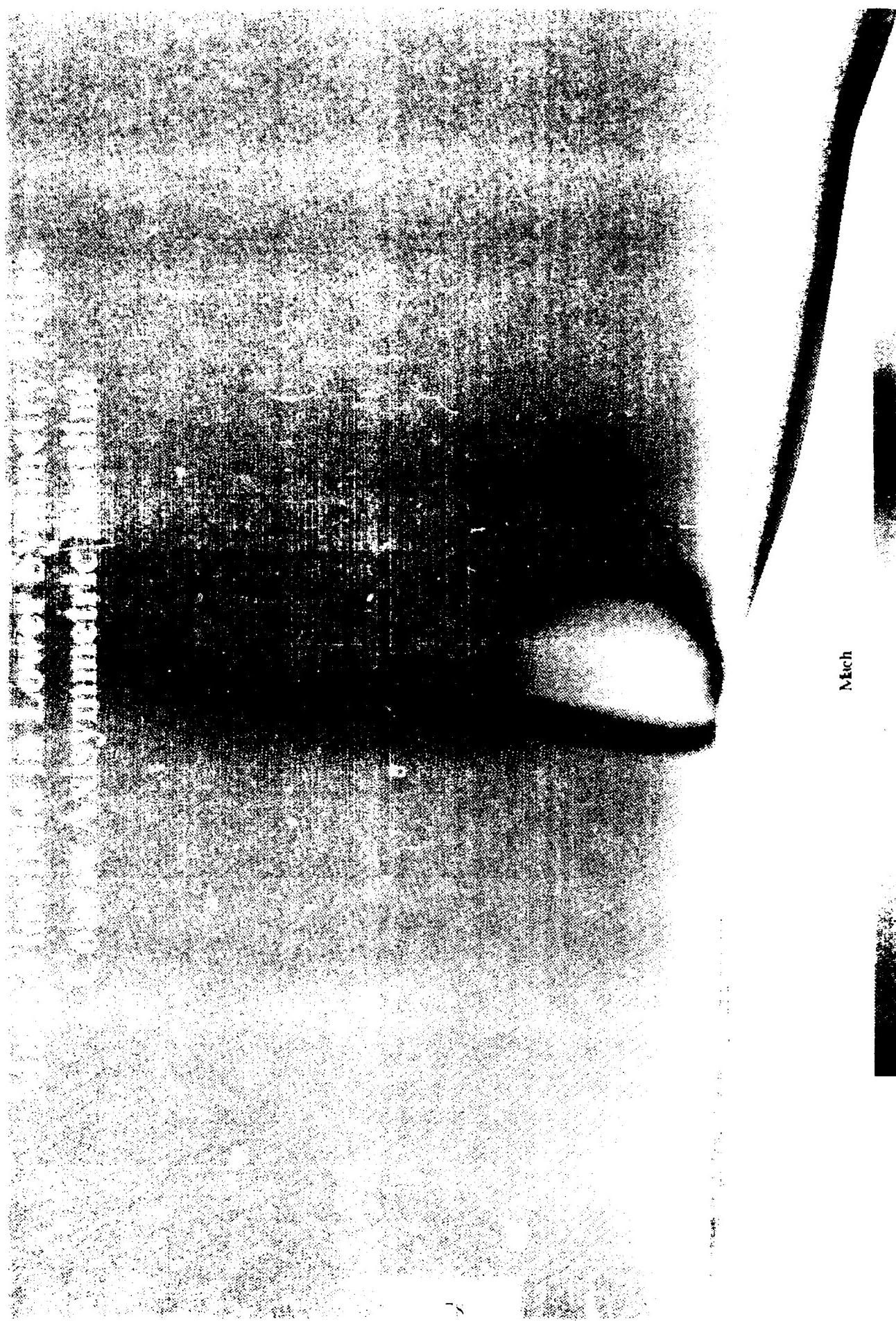
weak shock with a peak Mach number of 1.28 aft of the bump, followed by a recirculation region. Like the 3-D coarse grid, Baldwin-Lomax was used.

7.9 Fine Axisymmetric Results:

Figures 57 and 58 present views of the fine axisymmetric grid. Figures 59 and 60 show the FNS convergence time traces. Figures 61 and 62 provide the turbulent equation residual histories. Figures 63 to 65 depict the flowfield solution obtained, including the shock and the recirculation embedded in the boundary layer region. The peak Mach number for the fine baseline is just under 1.50. Since the axisymmetric case was considered more severe than the full 3-D case (because of the absence of mass flow relief), these results implied the actual configuration would experience a weaker shock or none at all.

The freestream turbulence intensity was selected as 0.6% to reflect a quiet day. The freestream turbulent dissipation rate was chosen as 971 ft^2/sec^3. Figures 66 and 67 depicts the corresponding turbulence. Figure 68 shows the contours of the derived pressure fluctuations.

7.10 Alternative Fine Axisymmetric Results:

An attempt was made to run an axisymmetric version of the alternative fairing. The desired convergence level, however, was not obtained for this configuration. The results were converged enough, however, to indicate a reduction in the peak Mach number to 1.2. The preliminary results also showed a recirculation still existed behind the fairing. Instead of refining this grid, efforts were concentrated on obtaining the fine grid 3-D results.

7.11 Fine 3-D Results:

The final results obtained were the fine grid 3-D FNS results. Figure 69 illustrates how the fine outer boundary encapsulated the one used in the coarse grid. Figures 70 to 72 show various views of the grid that was employed. Grid lines were not packed into the window corners in a typical manner. The corners were formed from lines wrapped down into the indentation, while the upper
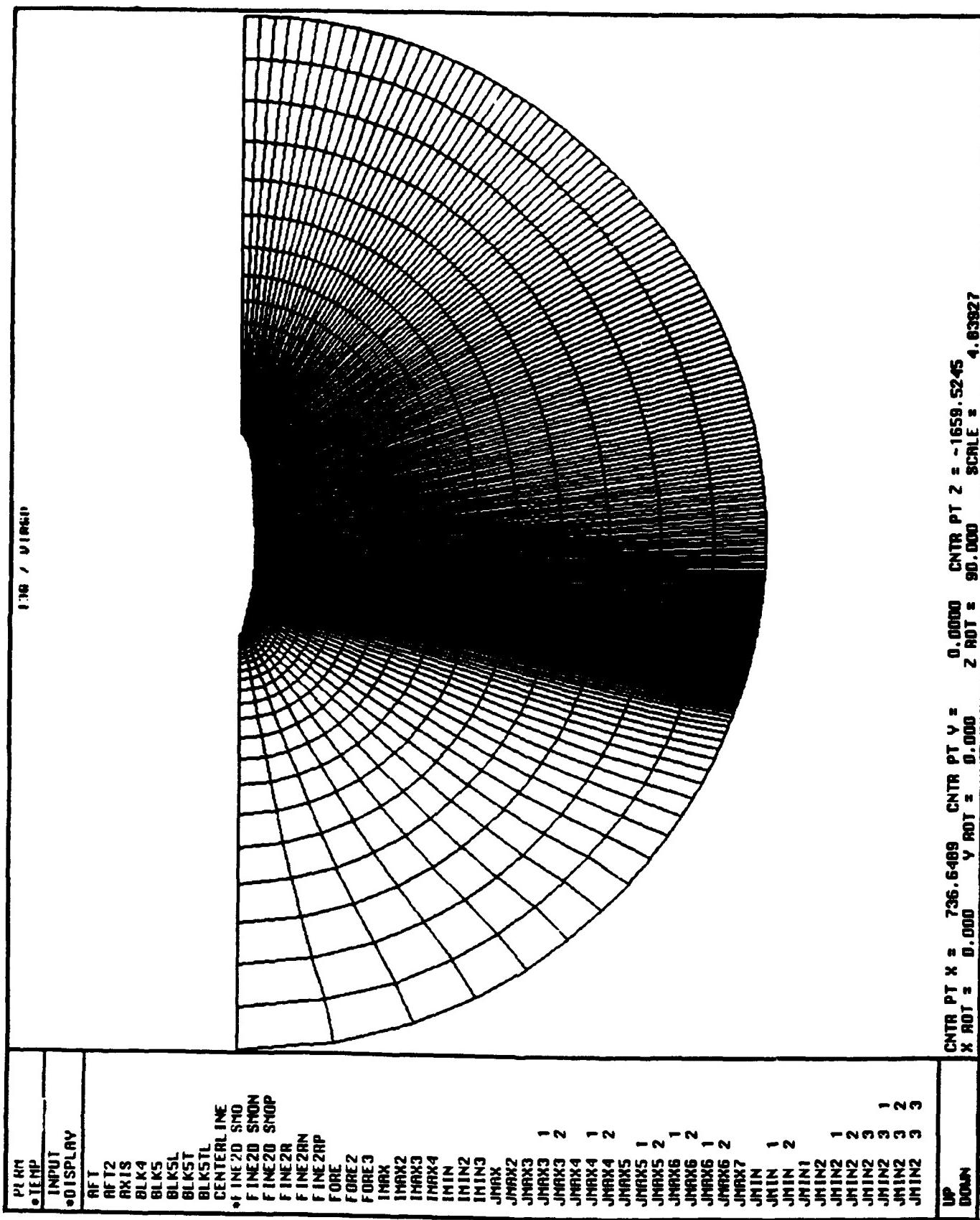
Figure 57: Fine Axisymmetric Grid, Far View
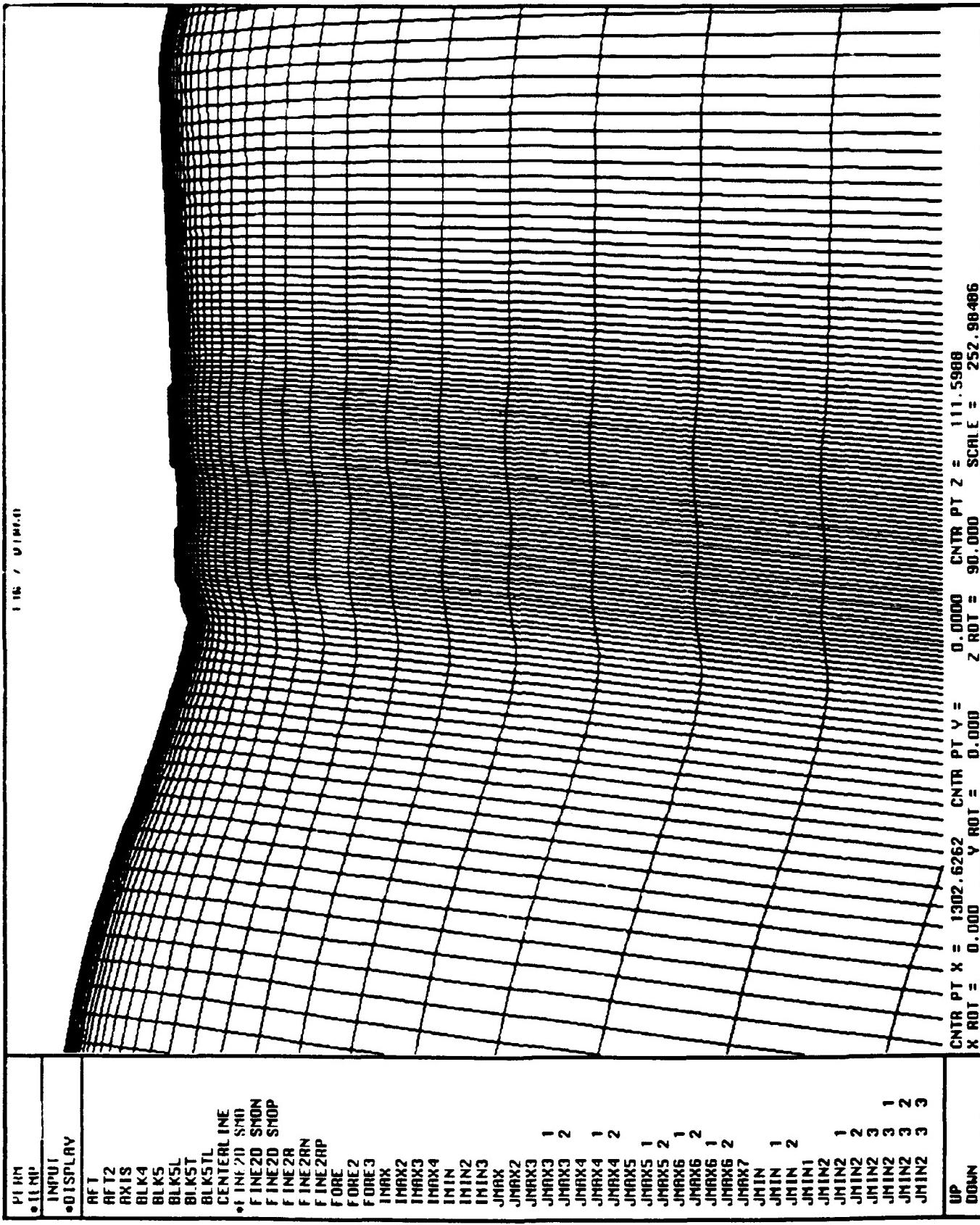
Figure 58: Fine Axisymmetric Grid, Near Modification View

Convergence History for NASTD Fine Axisymmetric Grid
Full Navier-Stokes with B-L-> K-e,.1st->2nd order Roe, Unlimited
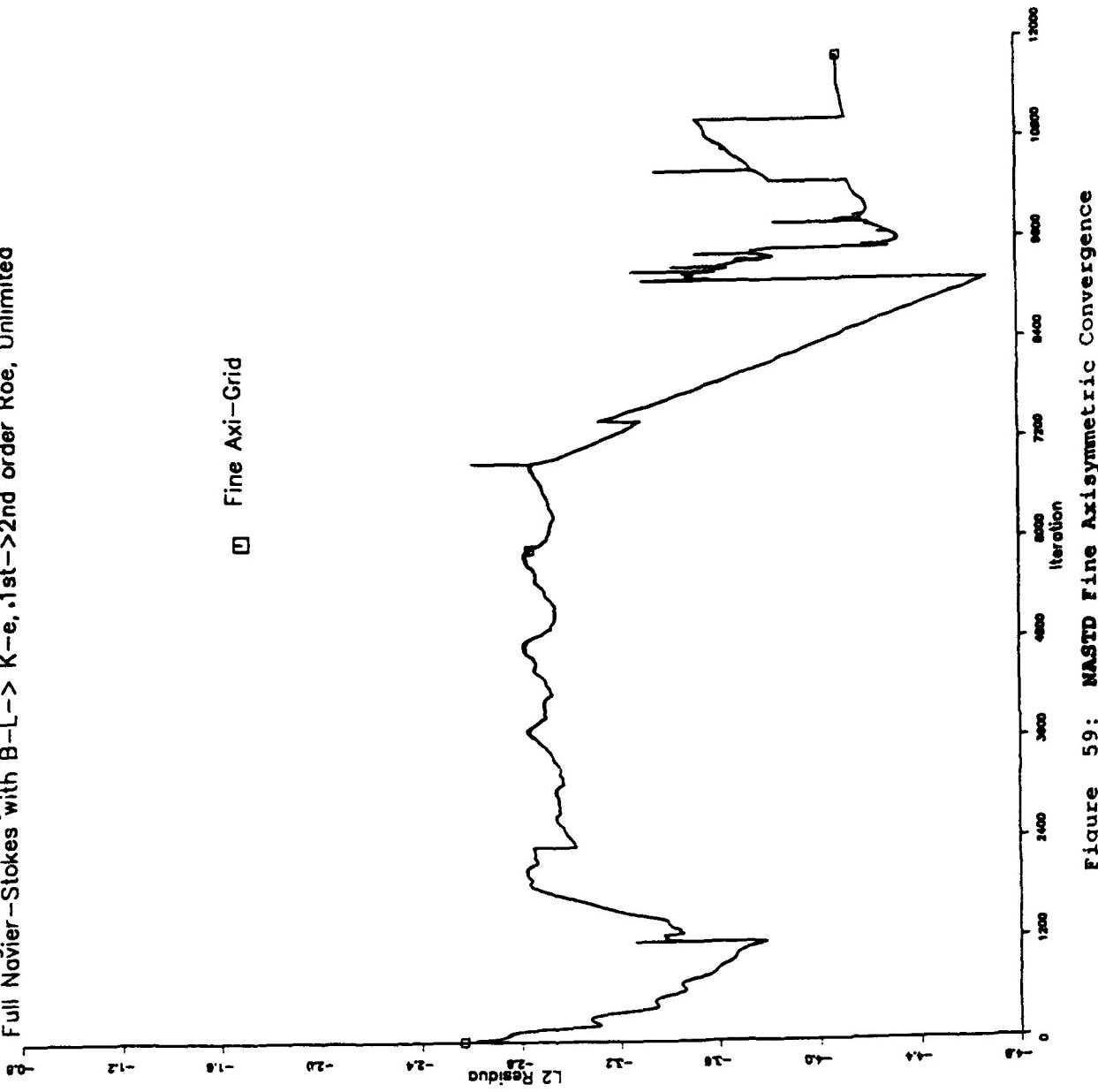
☐   Fine Axi-Grid

Figure 59: **NASTD** Fine Axisymmetric Convergence
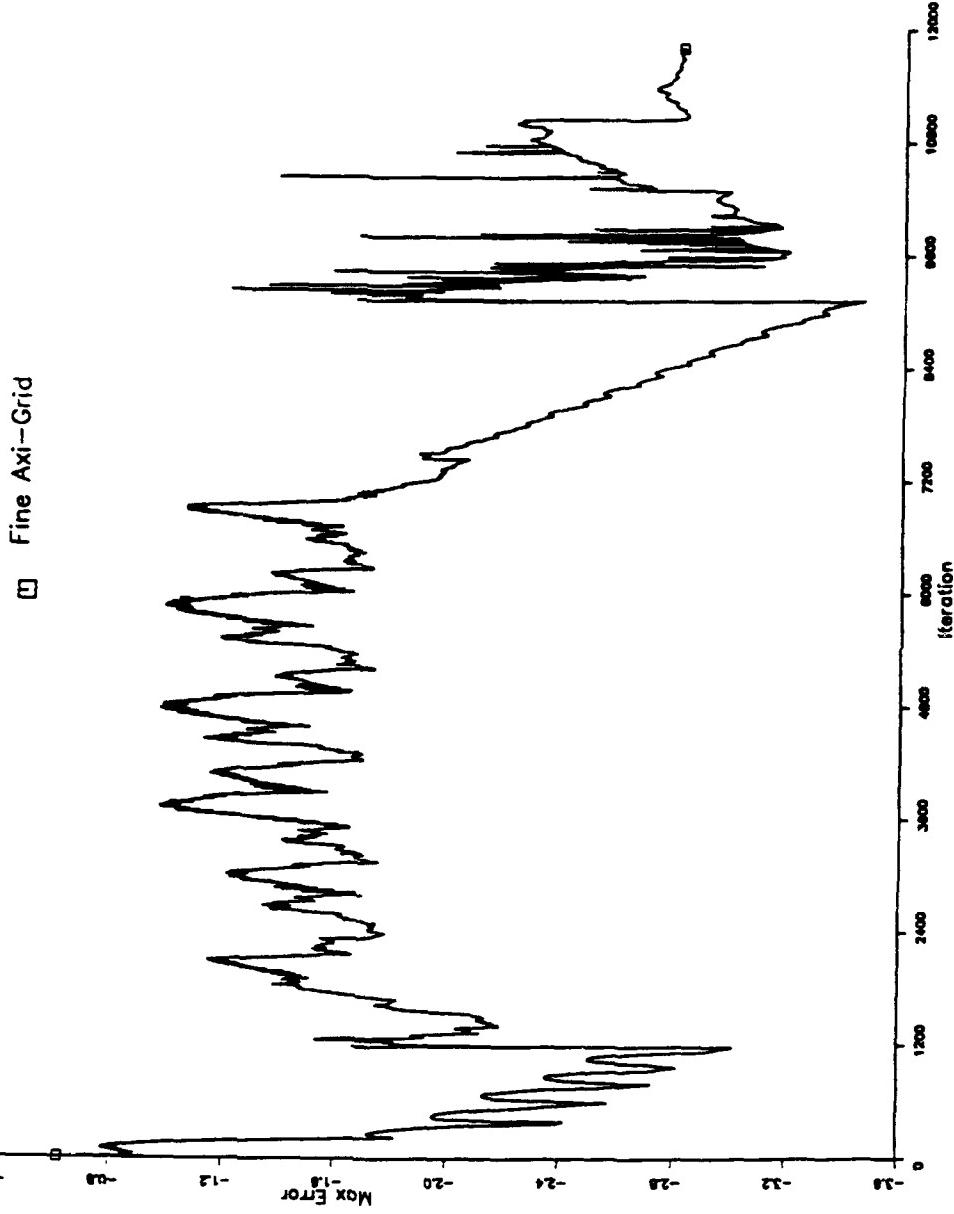
Figure 60: **NASTD** Fine Axisymmetric Max Error History

Convergence History for NASTD Fine Axisymmetric Grid
K—e Equations
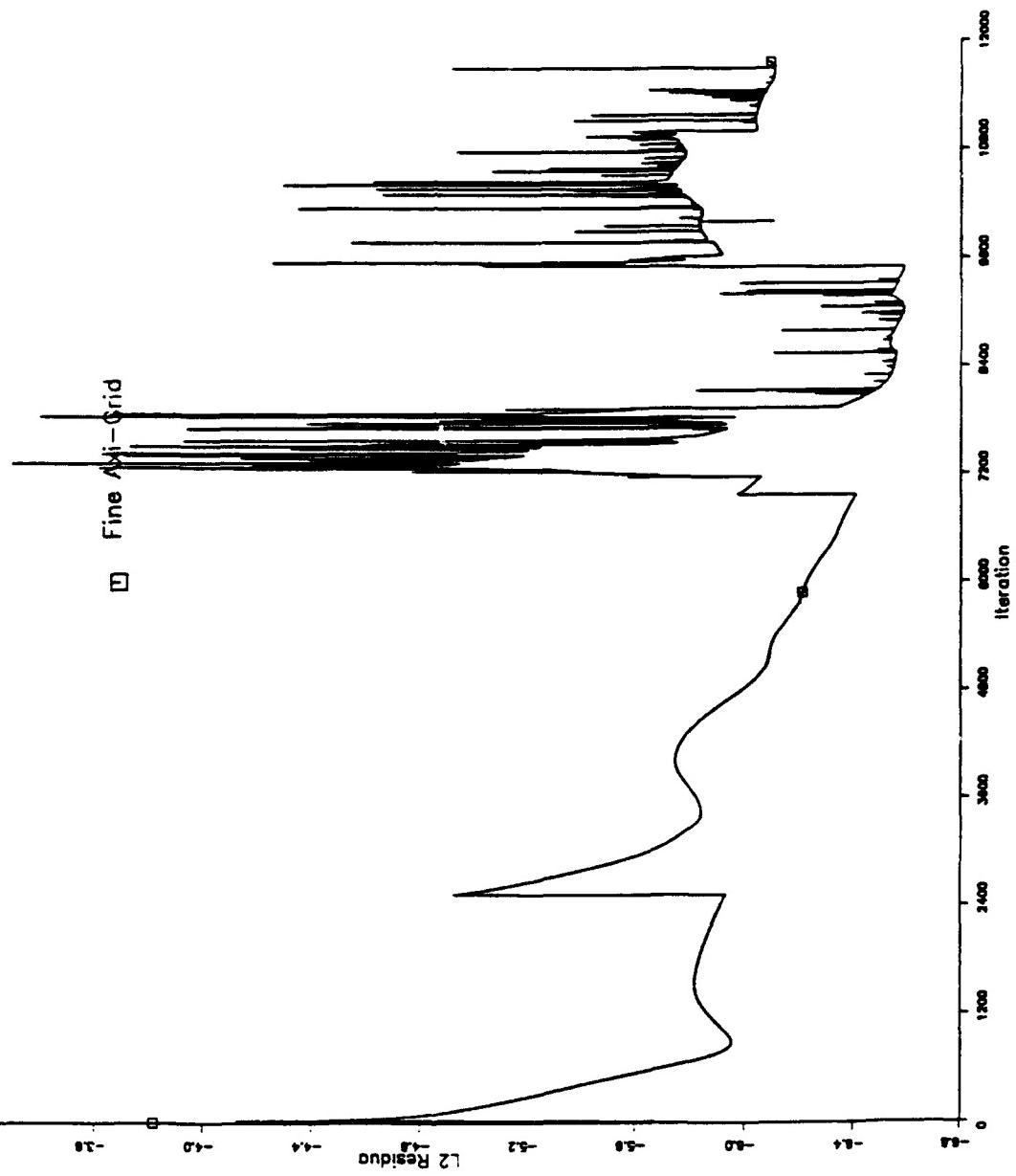
Figure 61:   **NASTD** Fine Axisymmetric k–ε Convergence

84

Convergence History for NASTD Fine Axisymmetric Grid
K-e Equations
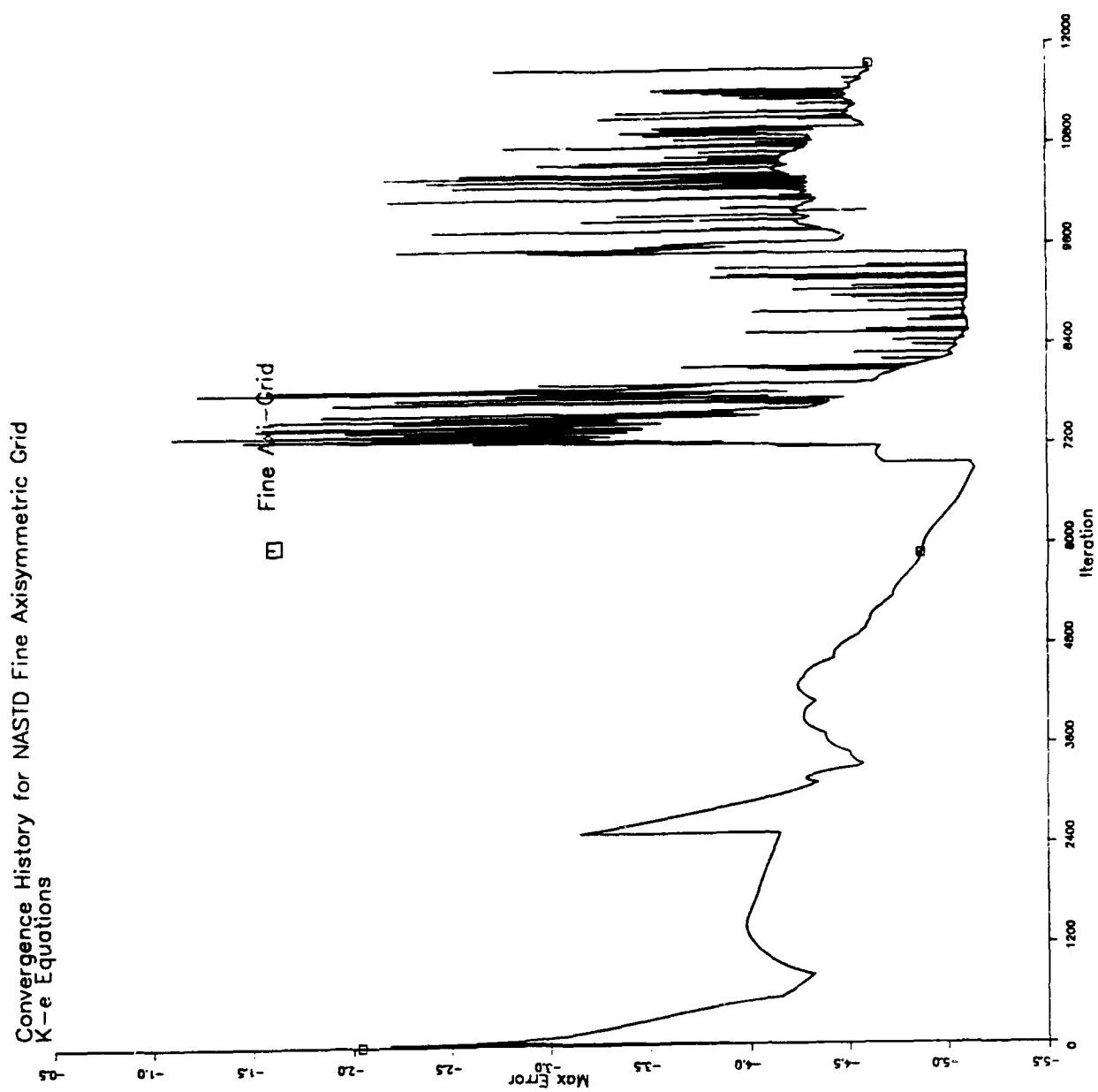
Figure 62: **NASTD** Fine Axisymmetric k-ε Max Error History

Cp

−1.20   −0.35   0.50

Figure 6.: NASTD C_p Contours, Fine Axisymmetric

Mach

0.00   0.25   0.50   0.75   1.00   1.25   1.50
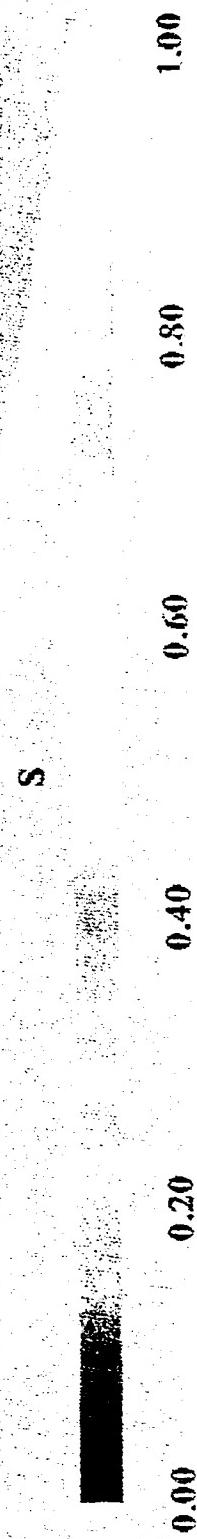
Lower Symmetry Plane Flowfield
Fine Axisymmetric Solution

Lower Symmetry Plane Flowfield
Fine Axisymmetric Solution

K

0.00   5500.00   11000.00   16500.00   22000.00
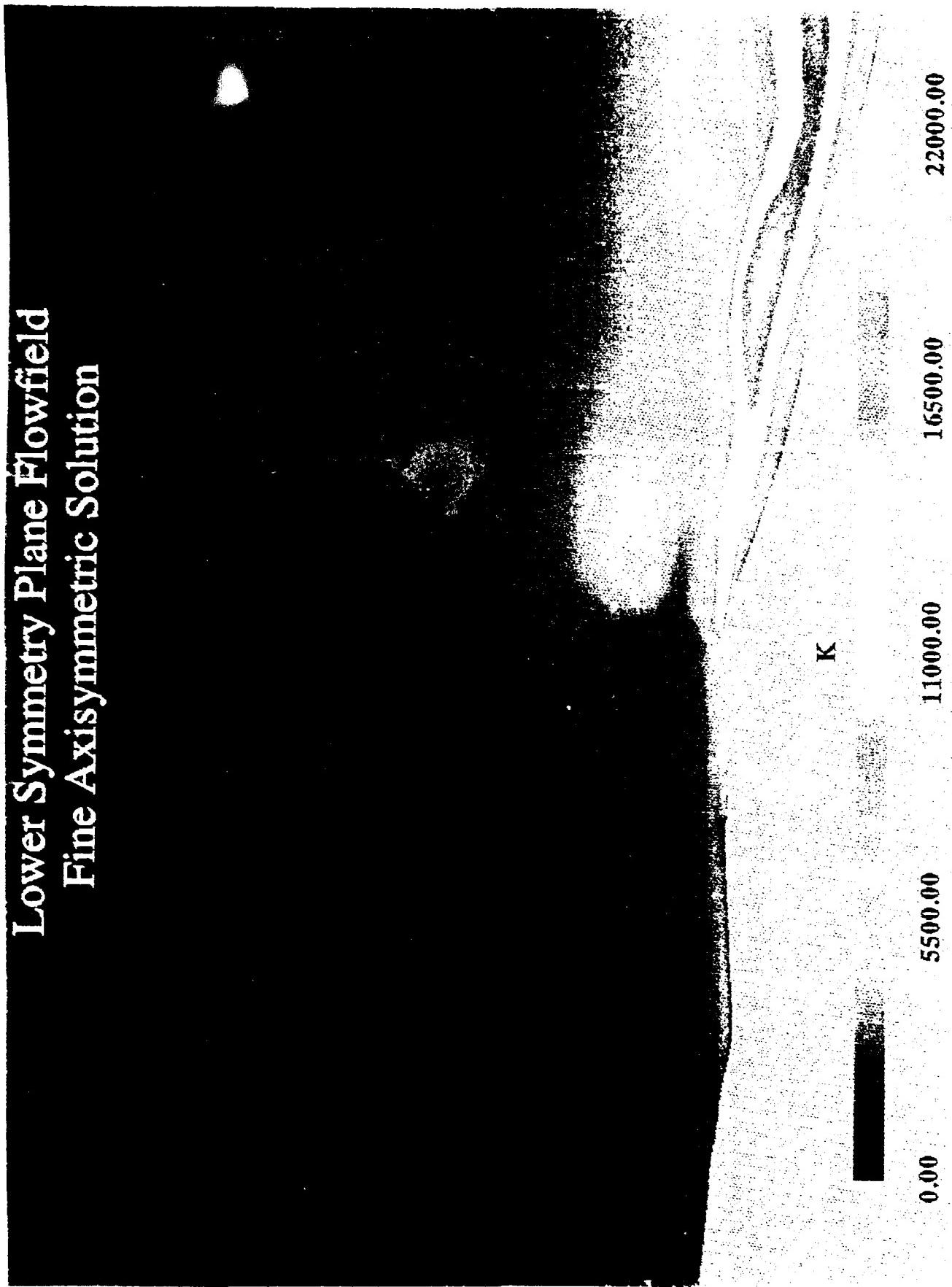
Lower Symmetry Plane Flowfield
Fine Axisymmetric Solution

Turb.Dissipation

0.00   50000000.00   10000000.00

NASTD

Open Skies Mod Area
k–e Reynolds Averaged Perturbations

delta_Cp

-0.40 -0.30 -0.20 -0.10 0.00

Figure 68: **NASTD** Derived C_p Fluctuation Contours, Fine Axisymmetric

Coarse 3-D
Outer Wrap

Body
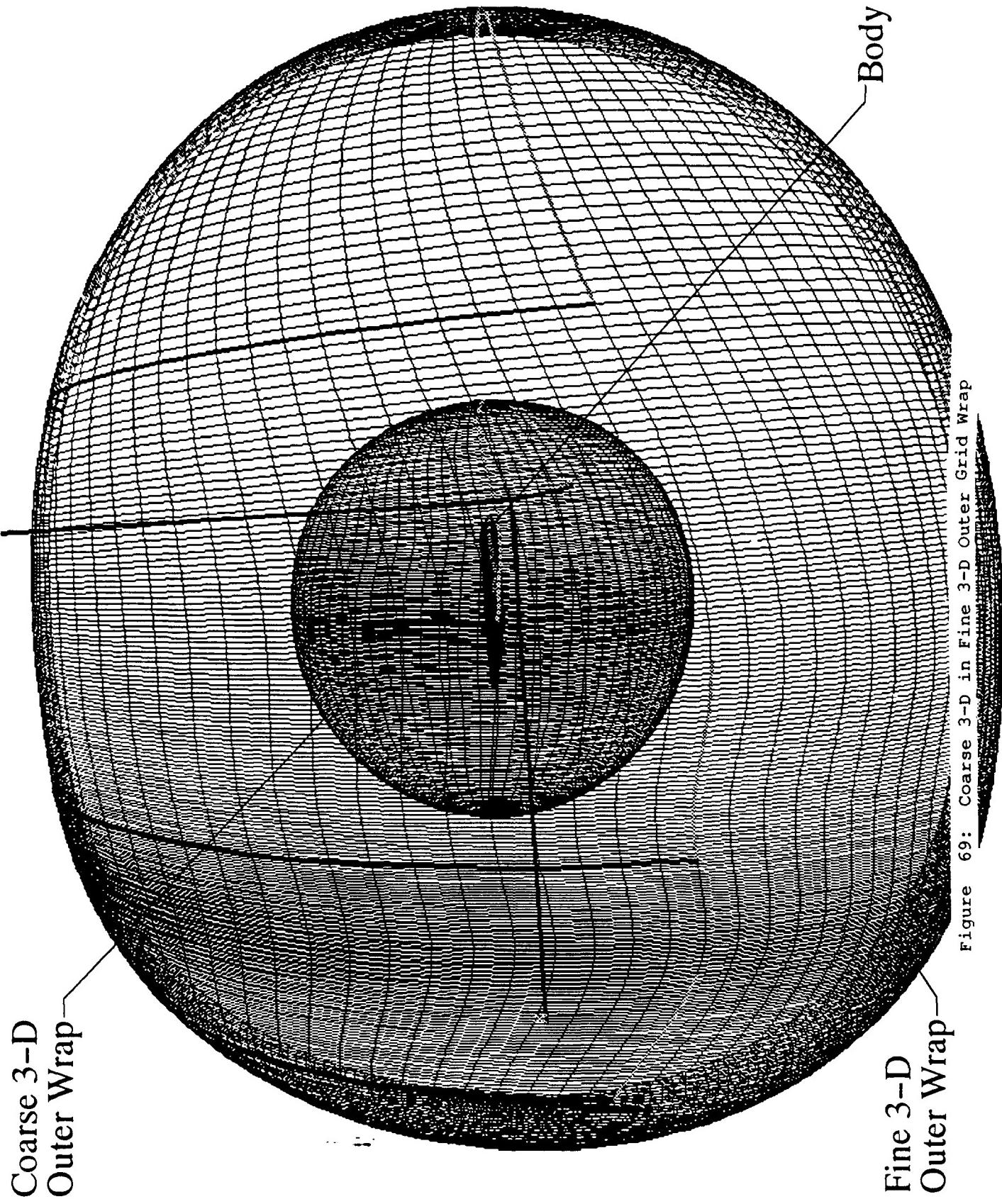
Fine 3-D
Outer Wrap

Figure 69: Coarse 3-D in Fine 3-D Outer Grid Wrap

92
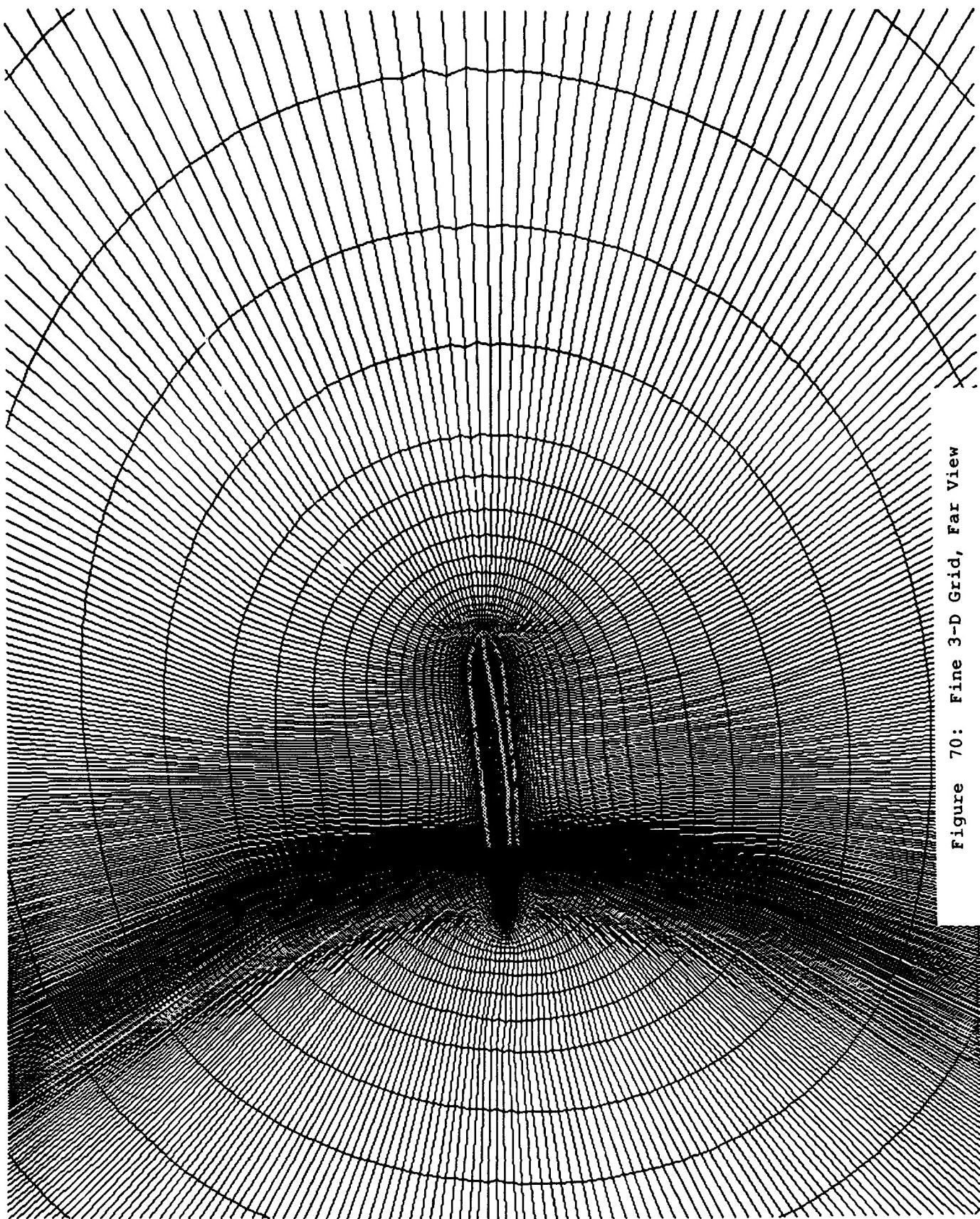
Figure 70: Fine 3-D Grid, Far View
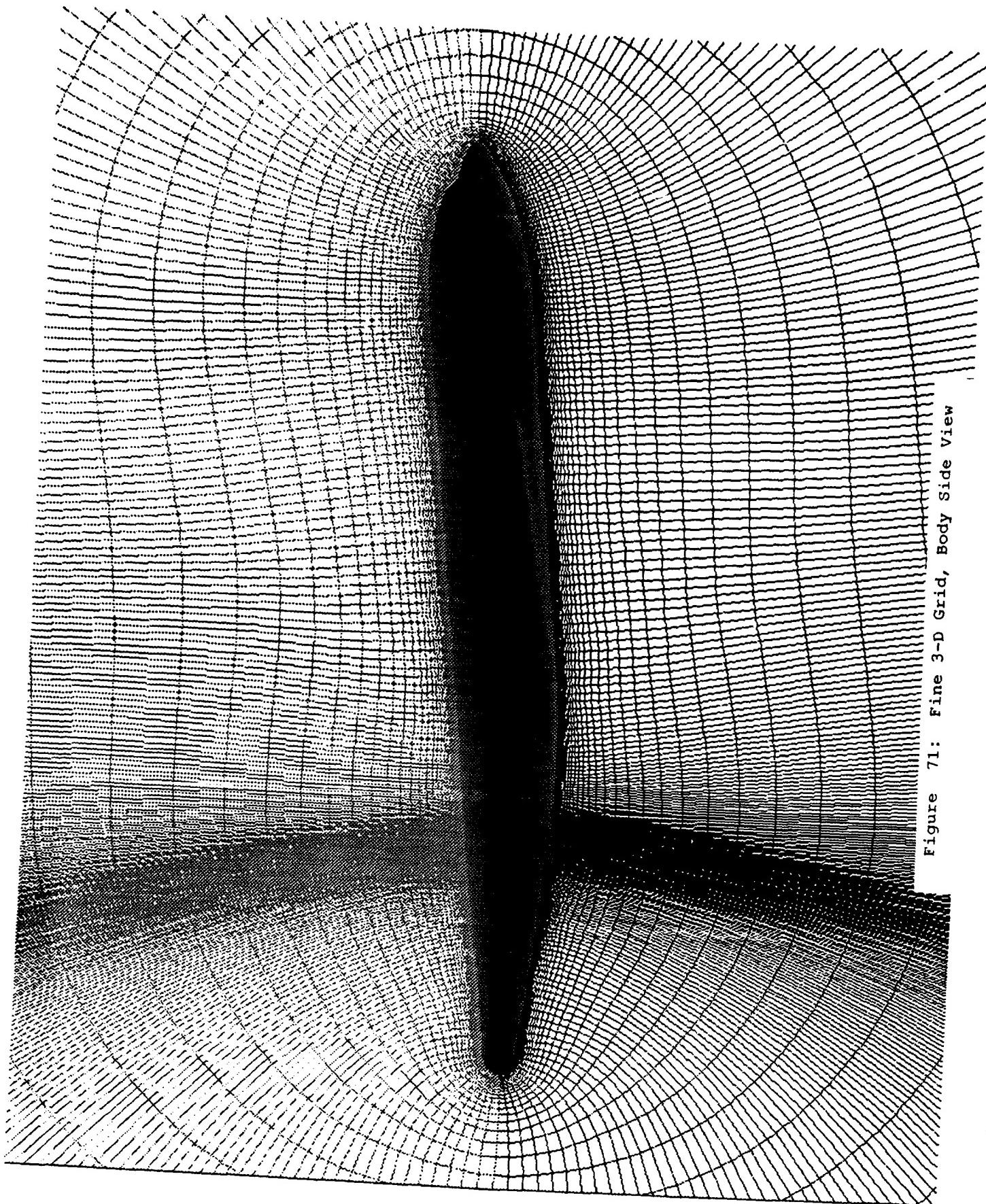
Figure 71: Fine 3-D Grid, Body Side View
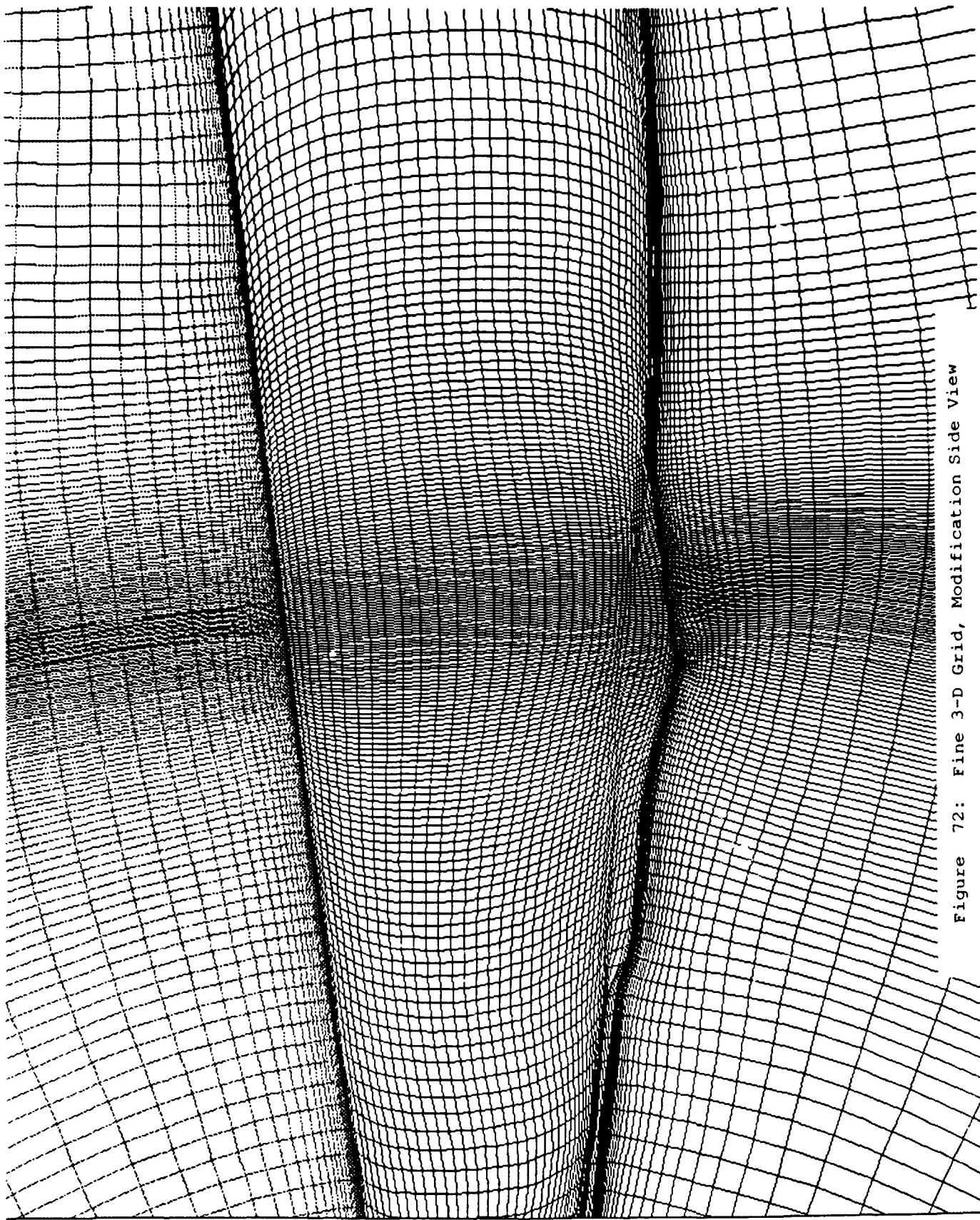
Figure 72: Fine 3-D Grid, Modification Side View

95

edges were formed by intentionally skewing the adjacent line to the upper corners. Separate patches with the skewed panels were smoothed out separately to minimize any errors in the solution. This new approach enabled the hyperbolic grid generation, and saved at least 40 circumferential points (to pack along the window buttline walls) and 160 streamwise points (to pack the four station walls). This did not resolve all the physics involved in the corners, but did resolve enough of the corner flow dynamics to permit an accurate solution downstream because of the robustness of **NASTD**. Figure 73 shows the surface gridding and grid plane off the aircraft centerline in the vicinity of the pod used for this part of the study. Figure 74 depicts how the hyperbolic scheme was used with 90 deg. corners to avoid increasing the computational cost by a factor of 3.8.

The coarse 3-D **NASTD** results were interpolated onto the fine 3-D grid using the McDonnell Douglas Aircraft Company **FPRO** copy utility. This was after a tricubic method (Ref's 45 & 46) was shown to overshoot values worse than **FPRO** interpolation for the coarse onto the fine 3-D grids.

The fine 3-D case was halted after convergence was obtained with the Baldwin-Lomax modeling. Figures 75 to 78 present the convergence of the residuals for the four zones. Time and cost factors didn't permit proceeding with k–ε. Analysis of the Baldwin-Lomax solution, however, showed no need to proceed further. The code results predicted that the flow over the Open Skies pod barely reached sonic conditions, with a peak Mach number of 1.06 (Figures 79 and 80). Only a very small reverse flow region is evident (Figure 81). It is speculated that the reason an acceptable solution was obtained with Baldwin-Lomax modeling alone was that the region of recirculation was off the surface of the body. This was seen in the fine axisymmetric case using k–ε as well.

Ideally, a time accurate solution using a turbulence model that works well with separated flow would be utilized. It was determined that the schedule (at least 28 days clock time on the **Cray II**) and funding ($252K+) would not permit a time accurate solution. This was based on implementing a running total of the density RMS (no animation) on the whole fine 3-D grid. The cost assessment was made using clocked **GASP2.2** Cray II performance, coarse 3-D time increments adjusted to fine

Body

Symmetry Plane
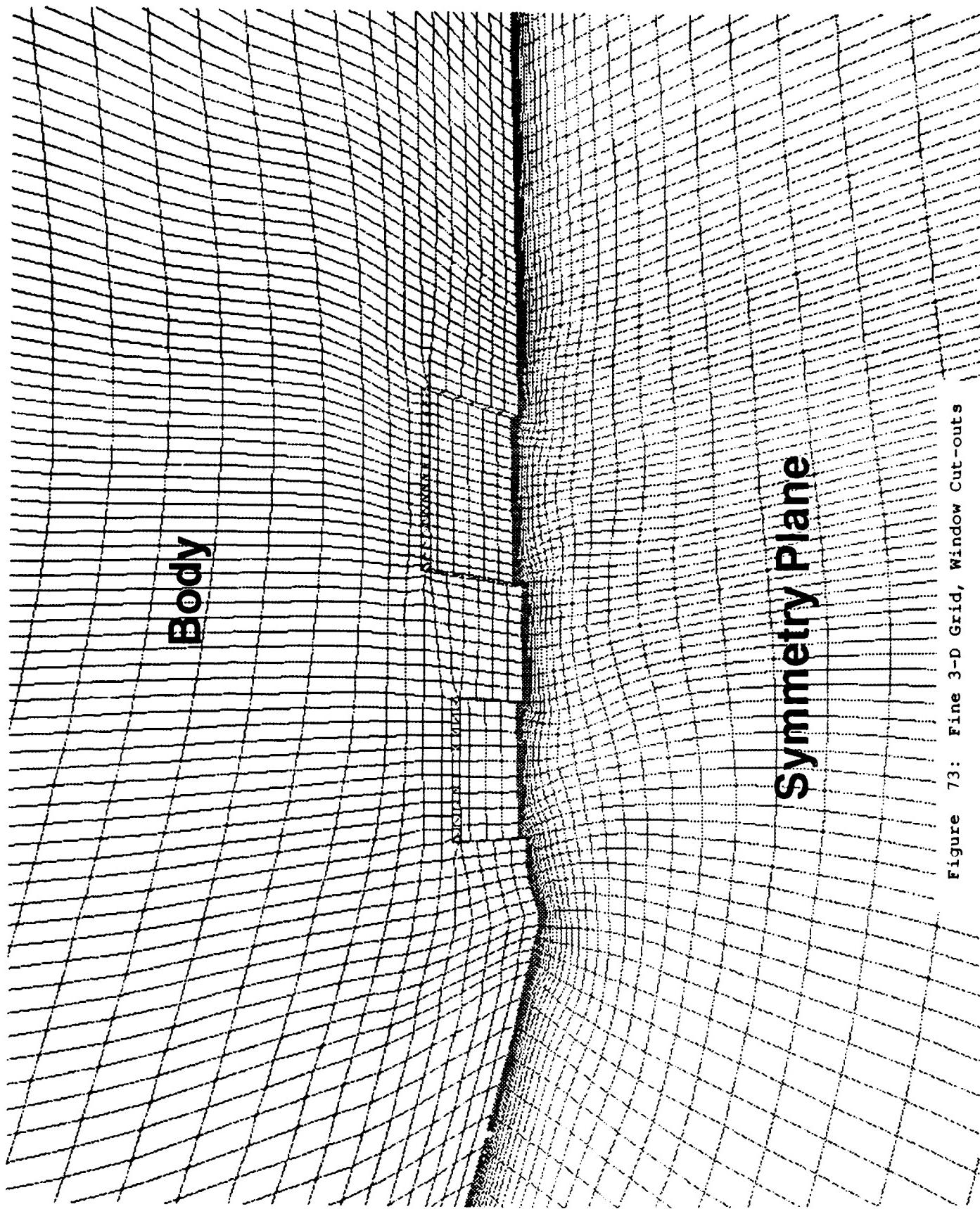
Figure 73: Fine 3-D Grid, Window Cut-outs
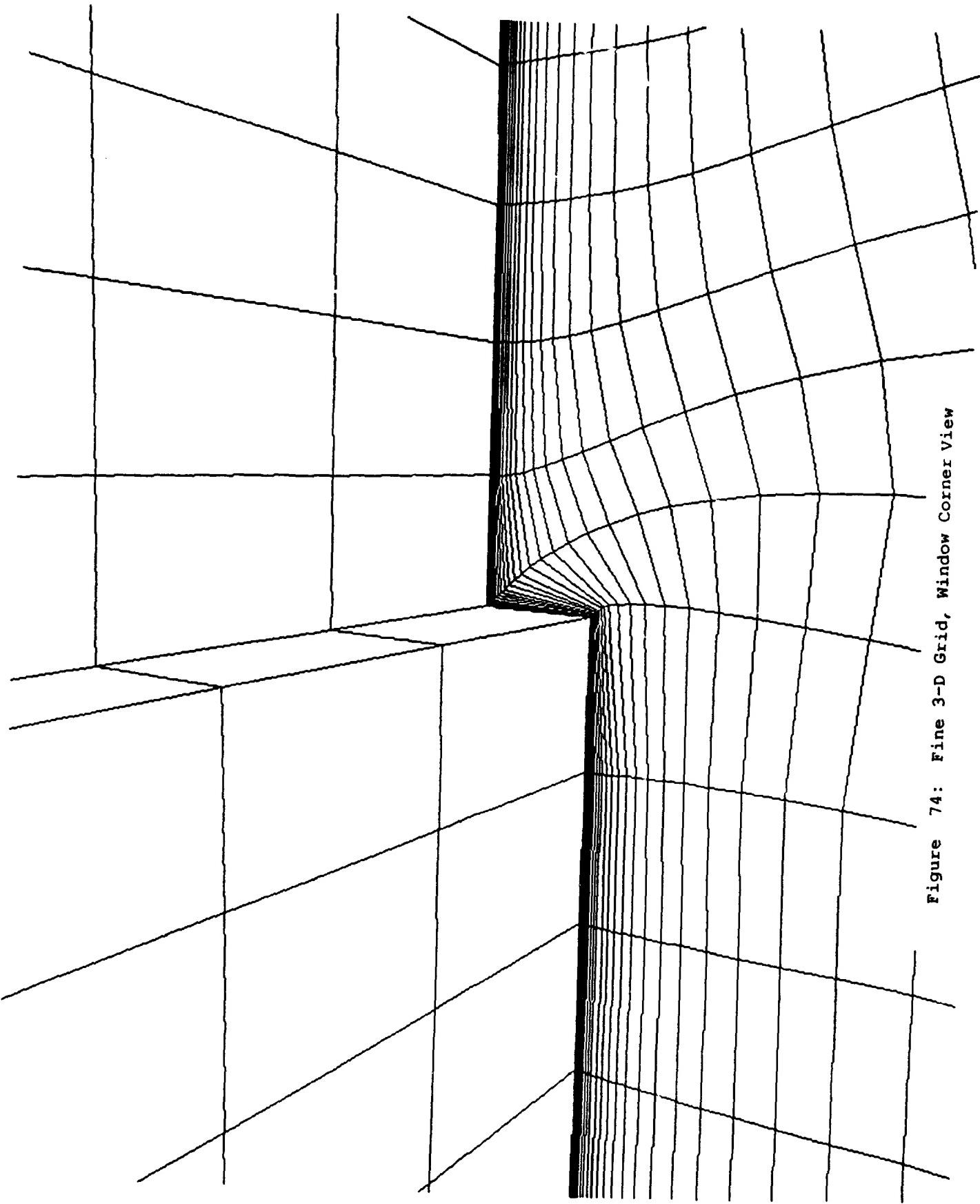
Figure 74: Fine 3-D Grid, Window Corner View

Convergence History for NASTD Fine 3-D Grid M=.84 AOA=1.4 Rn=60M
Full Navier-Stokes with B-L, 1st order Roe, Unlimited, Aft 4 Zones
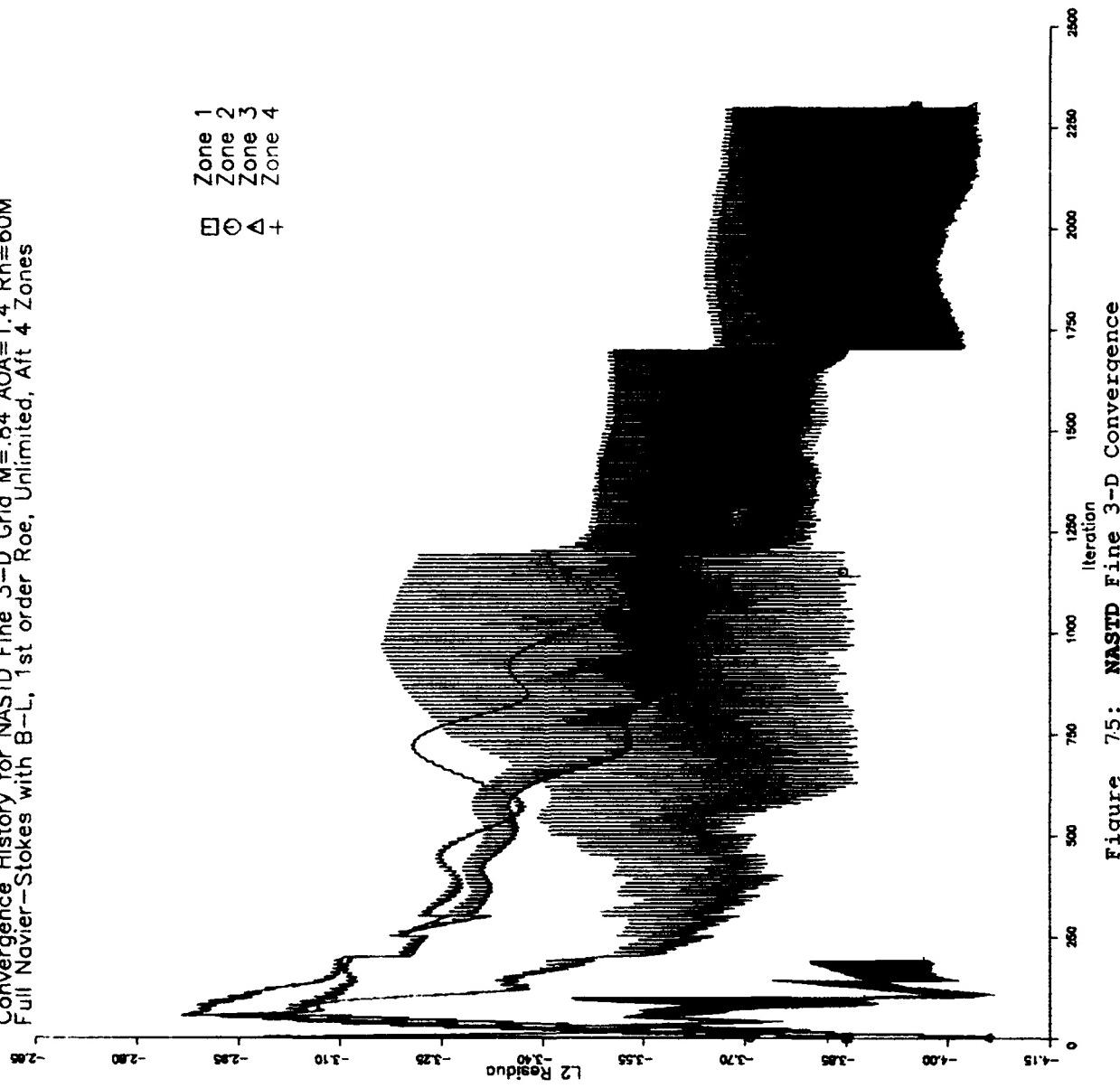
Figure 75: **NASTD** Fine 3-D Convergence

99
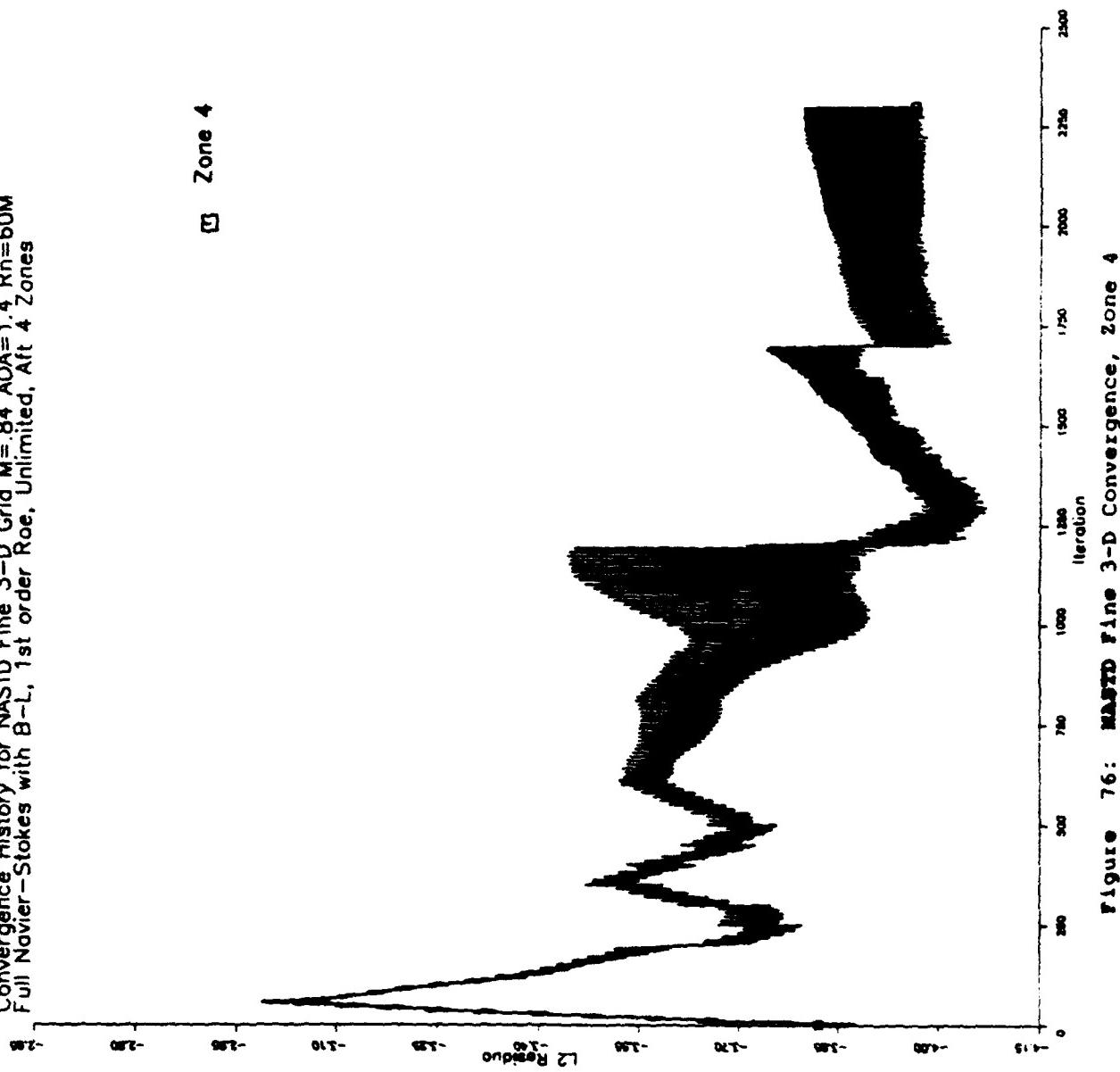
Figure 76: NASTD Fine 3-D Convergence, Zone 4
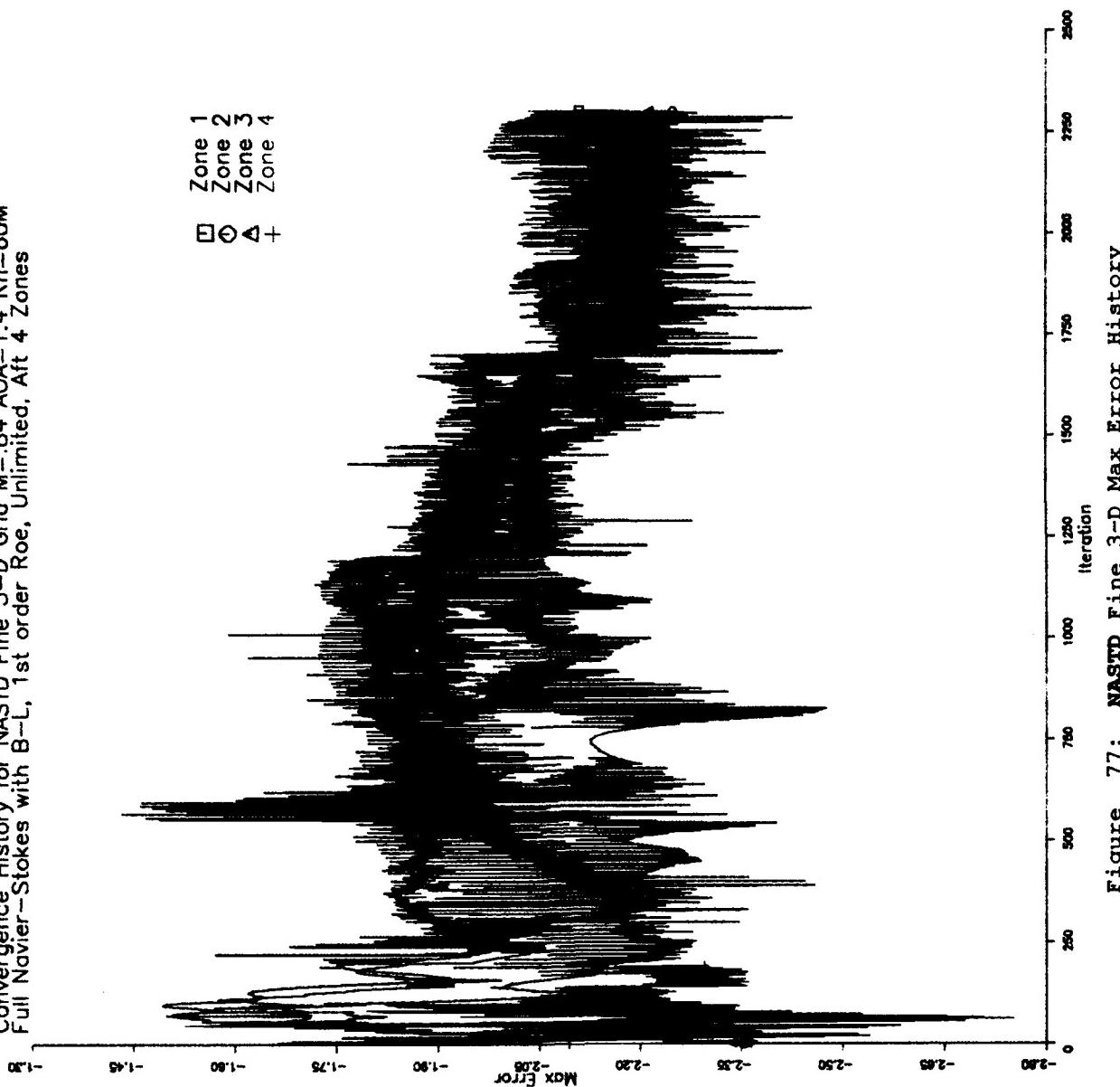
Figure 77: **NASTD** Fine 3-D Max Error History

101
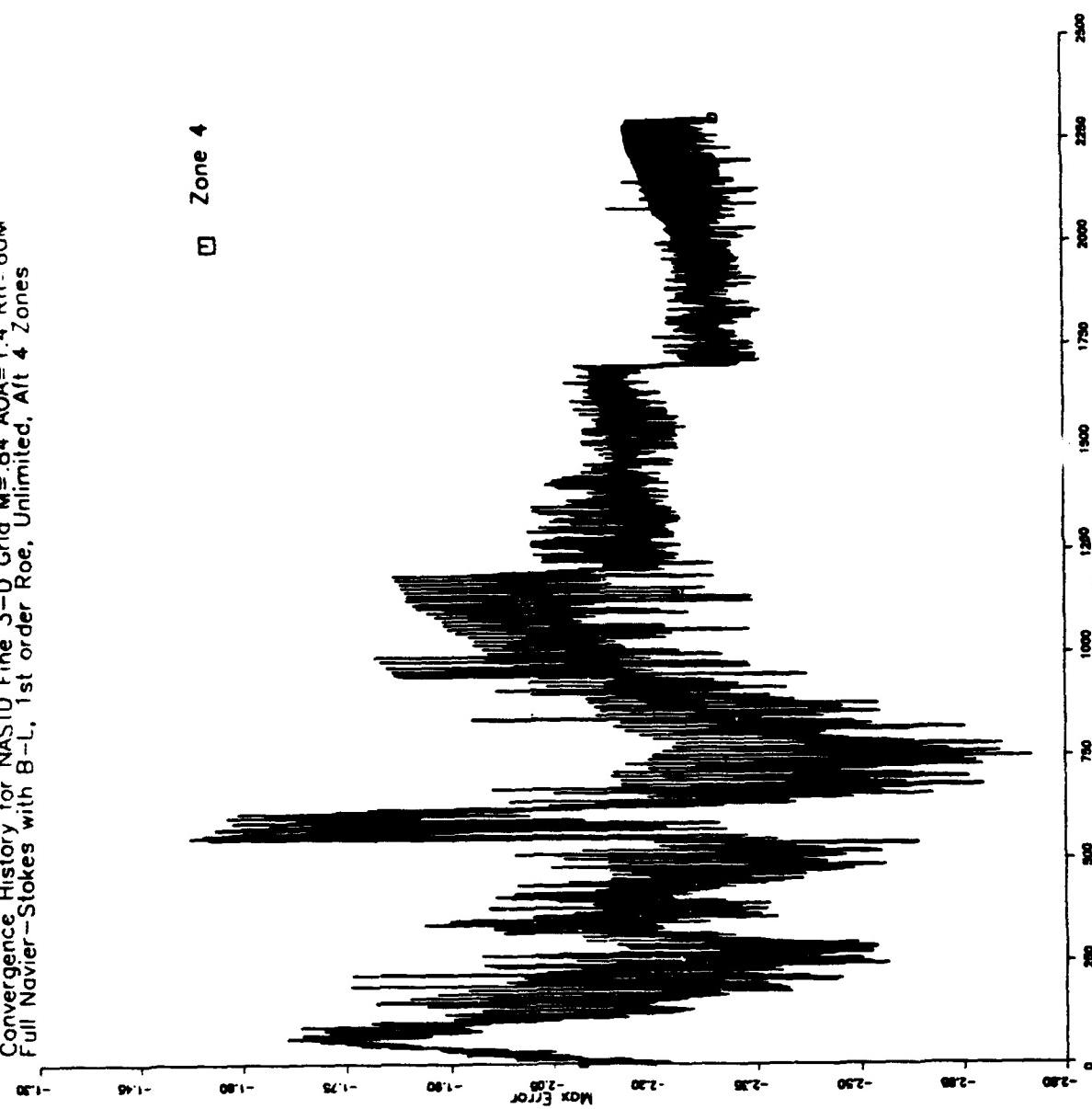
Figure 78: NASTD Fine 3-D Max Error History, Zone 4

102

Figure 50: NASTD -- Contour[..] Plot [..], Lower Surface 17 Plane

Cp

-1.20   -0.86   -0.52   -0.18   0.16   0.50
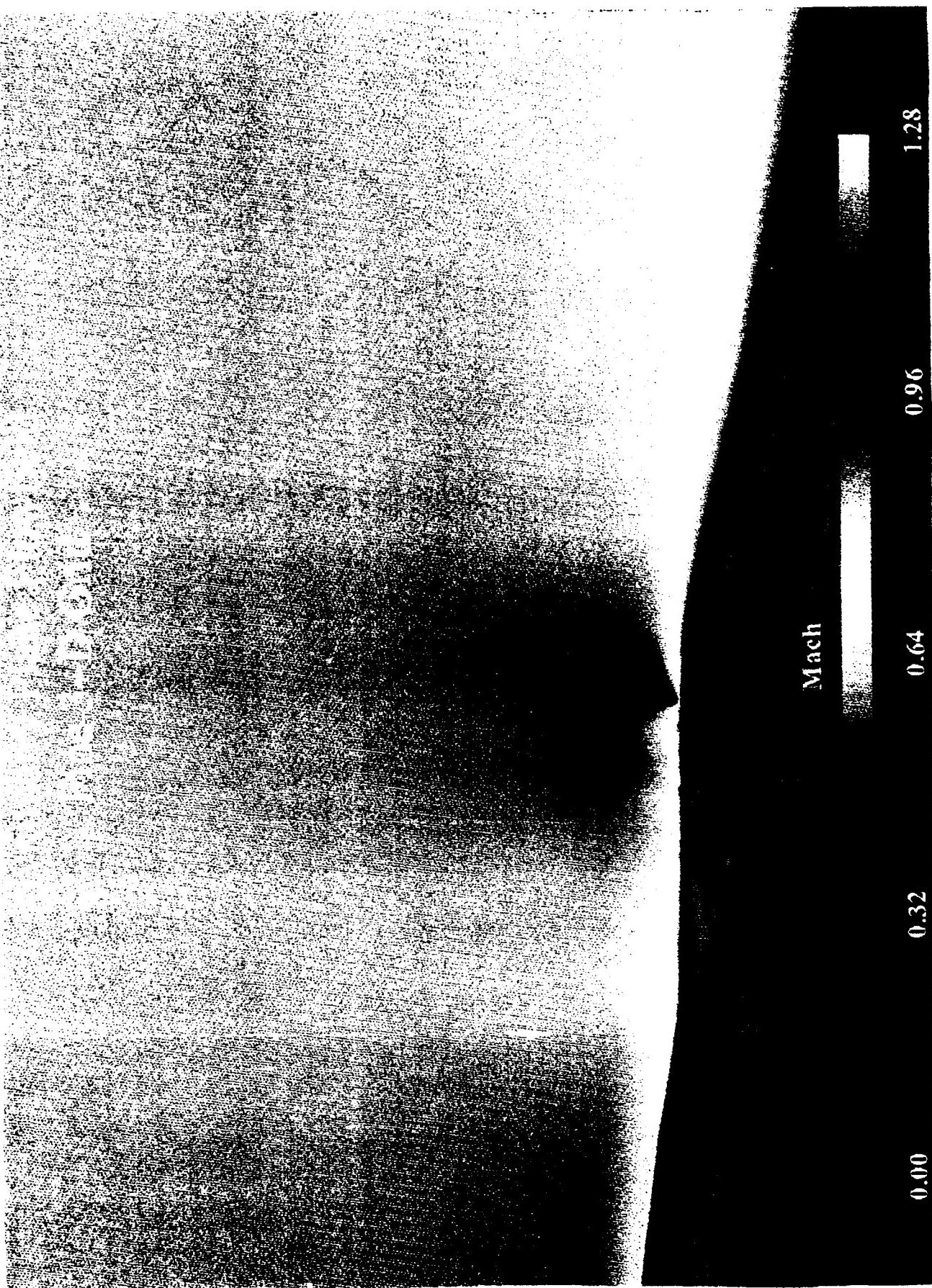
Figure 80: **NASTD** Mach Contours, Fine 3-D, Lower Symmetry Plane

3-D Fine Grid
Lower Symmetry Plane
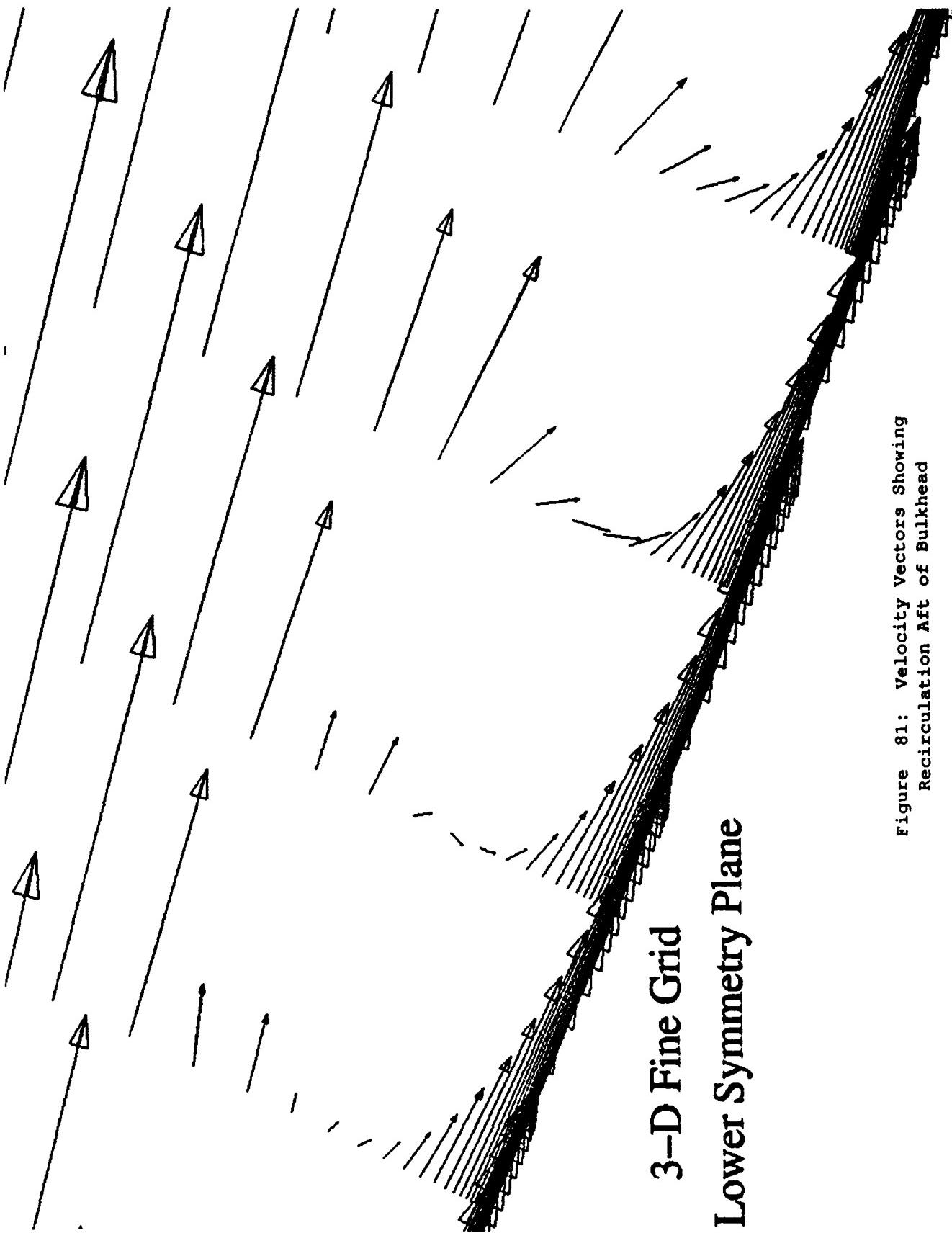
Figure 81: Velocity Vectors Showing
Recirculation Aft of Bulkhead

TLNS Baldwin-Lomax axisymmetric volumes, 17 characteristic time cycles (2.7549 seconds), and a KHz frequency (Ref. 47).

7.12 Postprocessing:

Solution contour postprocessing of the baseline design was performed using **Tecplot** (Ref. 48), Plot3D (Ref. 49), and FAST (Ref's 23 & 24). The line plots were created with Mr Slavey's **Freeplt** program, **Tecplot** and FAST. The key quantities plotted included pressure coefficient (C_p), Mach number (M), skin friction coefficient (C_f), turbulent kinetic energy (k), and turbulent dissipation rate (ε) contours.

7.13 Programmatic Interpretation of Results:

A comparison of the potential theory to viscous theory permitted quantification of the ΔC_p distributions, which provided a steady-state indication of the peak intensity of the recirculation region (Figure 82). The plot showed some viscous effects, but not severe.

For most cases the Jones-Launder model gives an accurate prediction. The Jones-Launder model uniquely among k-ε models usually underpredicts the pressure peak of separated regions (Ref. 33). Therefore, if a pressure rise problem due to separation is indicated by analysis, it is almost certain to be encountered in flight. If no difficulties are predicted, the analysis is slightly inconclusive. Given the barely supersonic local Machs, and a small recirculation off the surface, this problem was not judged to be an issue, and was demonstrated in flight. The turbulent variables k and ε give a qualitative indication of how much unsteady mixing and buffeting will occur. At this point of CFD development, even turbulence modeling experts don't have "a feel" for the interpretation of how the magnitudes correlate with buffet or flutter levels since unsteady parametric studies are too expensive and too time consuming to research. It is shown in Appendix B that k and ε can give indications as to the velocity and pressure average perturbation levels. However, since buffeting is inherently an unsteady phenomenon, it is frequency dependent. The analysis, therefore, of the high turbulence area aft of the bulkhead was inconclusive.
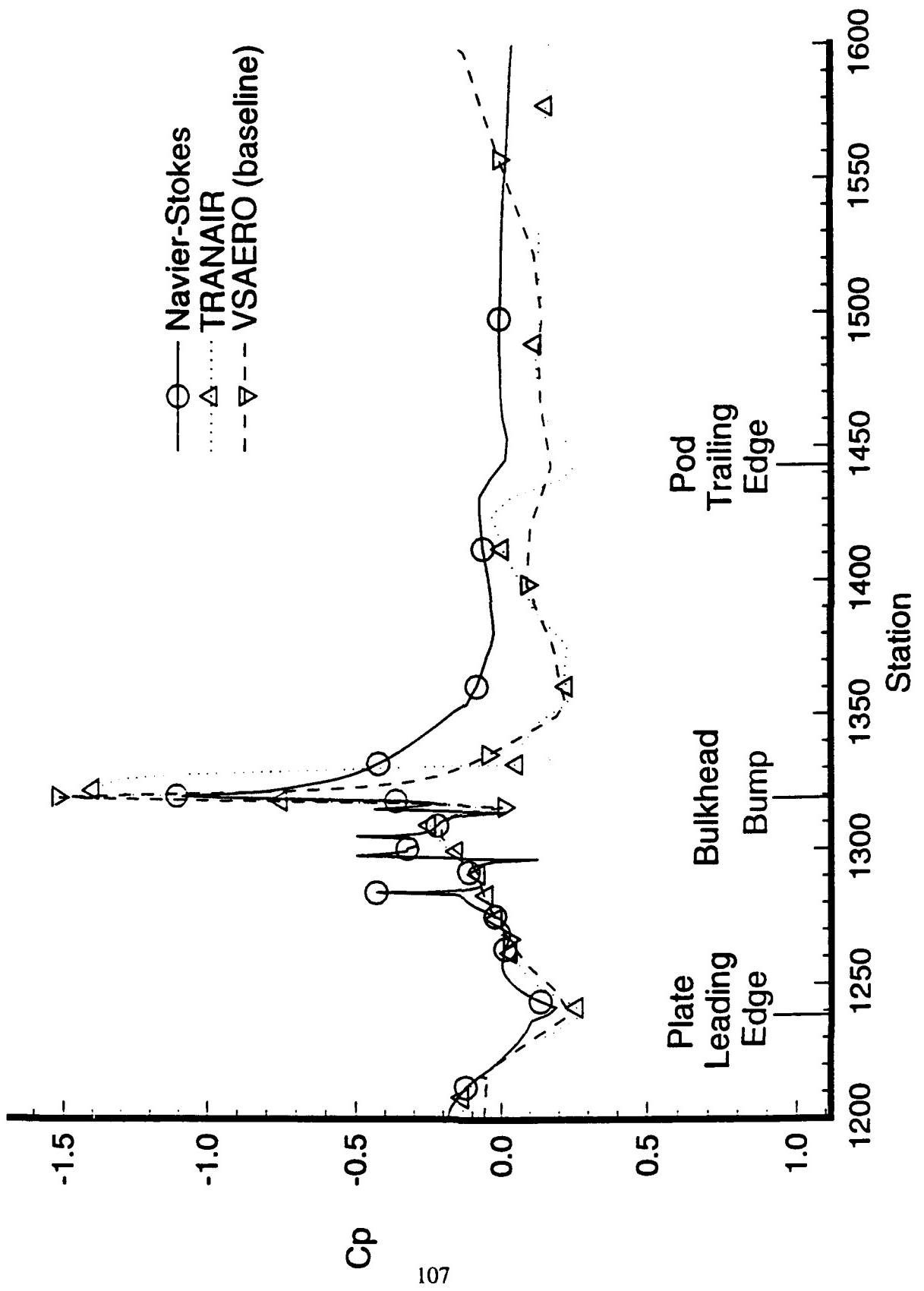
Figure 82: Comparison of NASTD, TRANAIR and VSAERO Predictions

107

The key result of the fine 3-D study was the prediction that there would be no shock over the Open Skies pod. Only when all the physics was included (3-D with compressibility and viscous effects) was no shock indicated (Table 3). The inability of the lower order codes to predict viscous effects forced the flow to continue accelerating over the back side of the pod. The viscous effects were able to at least partially mask the effects of the bulkhead for the higher order codes. The full 3-D effects were necessary for providing realistic crossflow and curvature relief around the pod.

Table 3: Open Skies Fine Grid CFD Predictions

Approach	Shock	Recirculation	Peak Mach
Panel Method (w/IBL)	Probable Shock. Possibly Strong	N/A	3.5
Full Potential (Inviscid)	Shock Possibly Strong	N/A	1.7
Axisymmetric FNS	Weak Shock	Small Recirculation	1.5
3-D FNS	No Shock	Smaller Recirculation	1.06

8. FLIGHT TEST RESULTS

A flight test program was conducted to establish the airworthiness and functionality of the Open Skies modifications (Ref. 50). Tufts were added around the pod prior to flight test to assist in identifying any potential aerodynamic problems. Initial flights were conducted for envelope clearance and flow visualization purposes on 21 and 23 May 1993. During the first day of testing the windows were covered by metal plates, and still photos were taken. The window covers were removed for the second test, and the flight was video taped from a chase plane providing data that was used for comparison with the pretest predictions. Accelerometers were also located inside the pod and surrounding area to measure vibration levels that could be compared to measurements taken on an unmodified aircraft.

The tufts indicated a recirculation region in the same vicinity as the 3-D fine Navier-Stokes results predicted (Figure 83). The associated region of high turbulent perturbations predicted by the fine axisymmetric computation were similar to tuft video results as well (Figure 66). As also indicated by the analysis, the recirculation was apparently not shock induced. This was evidenced by the fact that there was no associated significant increase in vibration levels in the aircraft. The alternate fairing was, therefore, deemed unnecessary and was not manufactured.

The ground condition of the tufts indicated there maybe an offset of turbulent intensity to the right of the centerline for some condition(s). This shift could have been caused by the pressure influence of the drain mast, or side slip effects. As mentioned previously, the mast was not modeled in the grids because it was thought to have minimal influence on the area of interest. Indeed for the flight test condition modeled, there was no clear indication of asymmetry.

Condition of Tufts after Flight Test
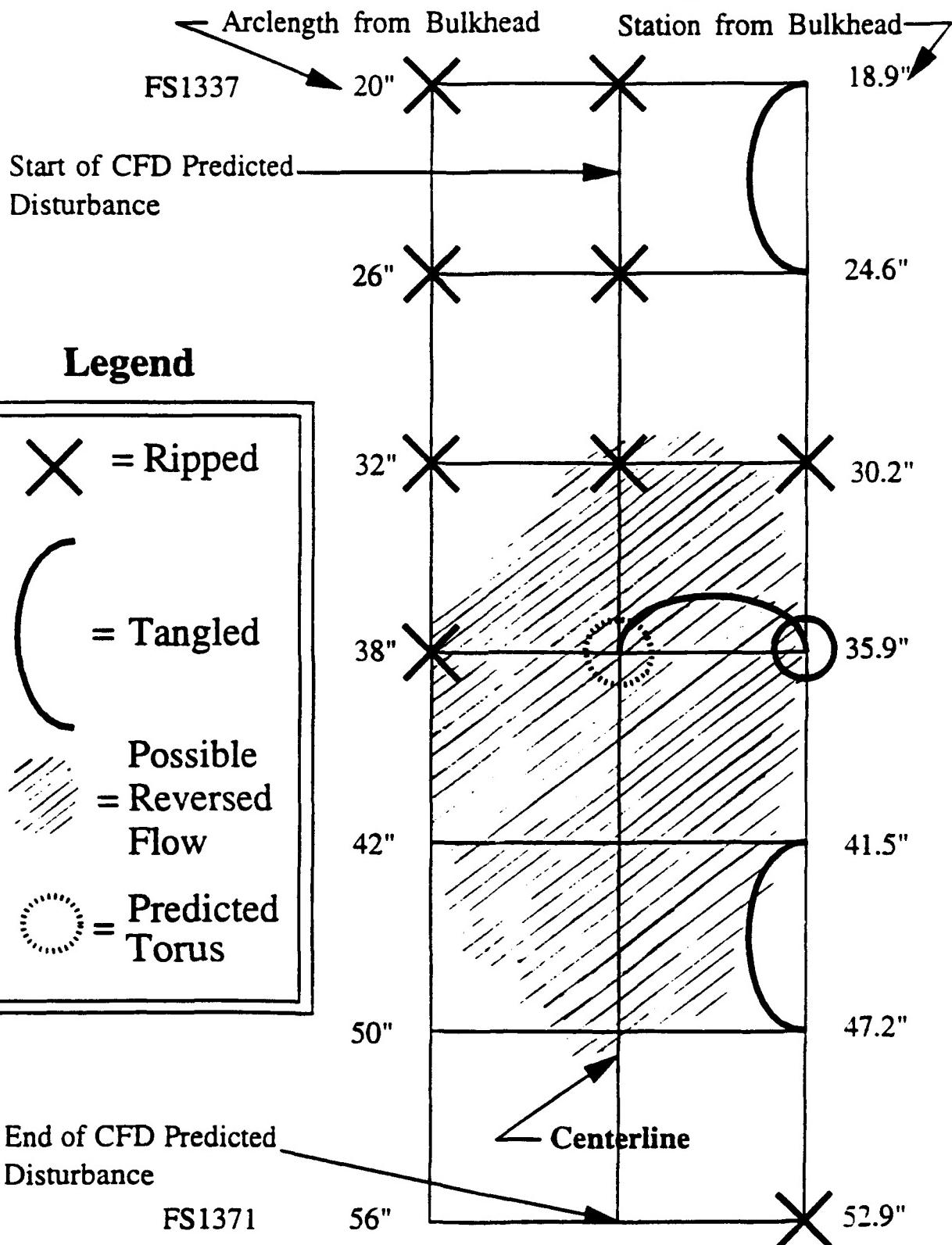
Figure 83: Comparison of Flight Test Tufts and CFD Predictions

110

9. CONCLUSIONS

Several different CFD analysis tools were utilized to analyze the flowfield over the Open Skies aircraft. The combined use of various levels of physics enhanced the usefulness of results over that which would have been obtained by using any one tool by itself. The panel method and full potential method provided early preliminary results and the opportunity for inexpensive trade studies and check runs. The axisymmetric studies provided more preliminary results with higher order physics, and provided trend indicators when compared to the lower order results. Innovative grid approaches were employed that greatly reduced the typical cost of FNS simulation. Finally, the fine 3-D Navier-Stokes analysis provided the complete answer to the problem. The alternative modification fairing was developed which should provide less recirculation extent but was deemed unnecessary based on flight test. The CFD study adequately predicted the flight test results, and alleviated pre-flight safety of flight and design concerns, bearing out the pragmatic worth of this recently matured technology.

The entire computational study took a half year to complete. It took four engineers a total of 272 man days and $35,952 of computational resources. Additional computer resources used included 280 hours on the **Crimson50**, plus five free **Cray XMP** hours on a nonpriority queue.

10. LIST OF REFERENCES

1   Boeing Co., Witchita Div., "Summary of the Stability Control and Flying Qualities Information for all the -135 Airplanes," D3-9090, Oct. 1973.

2.   Dvorak, F., "VSAERO A Computer Program for Calculating the Nonlinear Aerodynamic Characteristics of Arbitrary Configurations -- User's Manual Revision E.2," Analytical Methods, Inc., Oct. 1992.

3.   Nathman, J. K., "OmniPlot Plot File Format," AMI, Nov. 1991.

4.   Johnson, F. T., Samant, S. S., Bieterman, M. B., Melvin, R. G., Young, D. P., Bussoletti, J. E., Hilmes, C. L., "TRANAIR Computer Code (Theory Document)," BMAC (Boeing Military Airplane Company), 27 Nov. 1989.

5.   Johnson, F. T., Samant, S. S., Bieterman, M. B., Melvin, R. G., Young, D. P., Bussoletti, J. E., Hilmes, C. L., "TRANAIR Computer Code (User's Manual)," BMAC (Boeing Military Airplane Company), 27 Nov. 1989.

6.   Walters, R. W., Slack, D. C., Cinnella, P., Applebaum, M., and Frost, C., "A User's Guide to GASP," VPI&SU (Virginia Polytechnic Institute and State University), NASA/LRC (Langley Research Center), Nov. 1990.

7.   Walters, R. W., "GASP - version 1.3 Online User's Manual," VPI&SU (Virginia Polytechnic Institute and State University), NASA/LRC (Langley Research Center), 15 Jan. 1992.

8.   McGrory, W. D., Slack D. C., Applebaum, M. P., and Walters, R. W., "GASP - Version 2, The General Aerodynamic Simulation Program," June 1992.

9.   Bush, R. H., "User's Guide for Program NASTD," MDC (McDonnell Douglas Corporation) Proprietary, 29 July 1992.

10.   MDC Government Aerospace Systems-East CFD Group, "CFPOST Reference Manual," 6 Nov. 1992.

11.   Plested, R. I., "Portable Sideslip Gauge Flight Test Plan," 4950th Test Wing, 4950-FTP-92-04-01, unpublished, Feb. 1993.

12.   Boeing Military Airplane Co., "C-135A&B Flight Manual," pp. 5-13, T.O. 1C-135A-1, OC-ALC/MMEDT, Jan. 1989.

13.   Boeing Military Airplane Co.., "C-135B Flight Manual Performance Data, Appendix 1," Change 12, pp. 5-13, T.O. 1C-135B-1-1, OC-ALC/MMEDT, Feb. 1984.

14.   Boeing Witchita Co., "Substantiating Data Report for the C-135B, TF33-P5 Turbofan Engine-Aircraft Performance Flight Manual," D500-10209-1, Dec. 1982.

15. Emsley, H. T., "I3G VIRGO Interactive Graphics for Geometry Generation and Visual Interactive Rapid Grid Generation User's Manual," Wright Laboratory, WL-TM-91-316, June 1991.

16. Raj, P., Sikora, J. S., and Olling, C. R., "Three-dimensional Euler/Navier-Stokes Aerodynamic Method (TEAM) Volume III: Flow Analysis User's Manual," pp. 3-3 to 3-4, AFWAL-TR-87-3074 (Revised) Volume III, Lockheed Aeronautical Systems Co., Nov. 1988.

17. Chan, W. M., "User Guide for HYPGEN (Version 1.0)," NASA Ames, 25 Jan. 1991.

18. Jiang, M. Y., Remotigue, M., "Hands on EAGLE and EAGLEView Documentation," Mississippi State University Engineering Research Center (MSU/ERC), July 1992.

19. NSF ERC for CFS, "The EAGLE Papers," Mississippi State University, P.O. Drawer 6176, 1992.

20. Jiang, M. Y., "EAGLE - ese Documentation for the EAGLE Grid Generation System," MSU/ERC for CFS, June 1991.

21. Emsley, H. T., "PLuTO 3-D Grid Generator User's Manual," Wright Laboratory, WL-TM-91-312, June 1991.

22. Strang, W. Z., "QBERT: A Grid Evaluation Code," Flight Dynamics Laboratory, AFWAL-TM-88-193, July 1988.

23. Walatka, P. P., Clucas, J., McCabe R. K., and Plessel, T., "FAST User Guide, Beta 2.1," NASA Ames WAO and RND, June 1992.

24. Walatka, P. P., "FAST Maps, Beta 2.1," NASA Ames WAO and RND, June 1992.

25. Flight Technology Branch, "Results of an Aerodynamic Study on the Open Skies Pod," Internal Air Force letter to 4950 TESTW/FFX, 24 March 93.

26. Customer Support Branch, "Supercomputer Center Eglin AFB Facilities Guide," Eglin AFB, Mar. 1991.

27. Customer Support Branch, "SC-E (Supercomputer Center-Eglin)," Eglin AFB, 1993.

28. User Services Group, "Supercomputing at AFSCC-K, an Overview," PL/SCPR, Kirtland AFB, 1992.

29. TAI User Technical Services Group, "Vector View," Vol. 6, No.s 1-3, PL/SCU, Kirtland AFB, 1993.

30. User Services Group, "Introductory User Guide Phillips Laboratory Supercomputing Center," General Atomics Kirtland AFB, 1991.

31. AIAA 9th Computational Fluid Dynamics Conference, Buffalo, N.Y., Session 7--"Algorithms for Hypersonic Flows," talks given by Dr. D. P. Rizzetta, and Dr. R. W. Walters, June 13-15, 1989.

32. Ladd, J. A., and Kral, L. D., "Development and Application of a Zonal k–ε Turbulence Model for Complex 3-D Flowfields," AIAA 92-3176, July 1992.

33. Kuethe, A. M., and Chow, C. Y., "Foundations of Aerodynamics: Bases of Aerodynamic Design," Third Edition, pp. 348-409, John Wiley & Sons, 1976.

34. Outman, V. and Lambert, A. A., "Transonic Separation," pp. 671-674, Journal of the Aeronautical Sciences, Nov. 1948.

35. Coakley, T. J., and Huang, P. G., "Turbulence Modeling for High Speed Flows," AIAA 92-0436, Jan. 1992.

36. Johnson, D. A., "Transonic Separated Flow Predictions with an Eddy-Viscosity/Reynolds-Stress Closure Model," AIAA Journal, Vol. 25, No. 2, Feb. 1987.

37. Nichols, R. H., "A Two-Equation Model for Compressible Flows," AIAA-90-0494, Jan. 1990.

38. Jones, W. P. and Launder, B. E., "The Prediction of Laminarization with a Two Equation Model of Turbulence," International Journal of Heat and Mass Transfer, Vol. 15, pp. 301-305, 1972.

39. Jones, W. P. and Launder, B. E., "The Calculation of Low-Reynolds-Number Phenomena with a Two-Equation Model of Turbulence," Int. J. of Heat Mass Transfer, Vol. 16, pp. 1119-1130, 1973

40. Rizzetta, D. P. "Numerical Simulation of Slot Injection into a Turbulent Supersonic Stream," AIAA-92-0827, Jan. 1992.

41. Baldwin, B. S. and Lomax, H., "Thin Layer Approximation and Algebraic Model for Separated Turbulent Flows," AIAA 78-257, Jan. 1978.

42. Anderson, J. D., Jr., "Hypersonic and High Temperature Gas Dynamics," pp. 280-283, McGraw-Hill Bood Co., 1989.

43. Anderson, D. A., Tannehill, J. C., and Pletcher, R. H., "Computational Fluid Mechanics and Heat Transfer," pp. 132, 133, 197-208, Hemisphere Publishing Corp., 1984.

44. Schlichting, H., "Boundary-Layer Theory," Seventh Edition, McGraw Hill Book Co., 1979.

45. Yarrow, M. and Mehta, U., "Tri-Cubic Interpolations Between Generalized Coordinate Systems," Sterling Software and NASA Ames, 1989, unpublished.

46. Yarrow, M. and Mehta, U., "Multiprocessing on Supercomputers for Computational Aerodynamics," The International Journal of Supercomputer Applications, Vol. 5, No. 2, pp. 46-72, Summer 1991.

47. Purohit, S. C., Shang, J. S., and Hankey Jr., W. L., "Numerical Simulation of Flow Around a Three-Dimensional Turret," AIAA Journal Vol. 21, No. 11., Nov. 1983.

48. Amtec Engineering, Inc., "Tecplot Version 5, from Amtec," Bellevue, WA, Jan. 1992.

49. Walatka, P. P., Buning, P. G., Pierce, L., and Elson P. A., "Plot3D User's Manual," NASA Ames, NASA-TM-101067, March 1990.

50. Confer, M. D., Eager, K. E., and Trent, T. T., "Open Skies Flight Test Report," 4950-FTR-93-02, 22 December 1993.

51. White, F. M., "Viscous Fluid Flow," Second Edition, pp. 369-393, 413, McGraw Hill, Inc., 1991.

52. John, J. E. A., "Gas Dynamics," Second Edition, pp. 283, 284, Allyn and Bacon, Inc., 1969.

APPENDIX A
Transition Prediction

The lower surface (and most of the fuselage) of the WC-135B has no curvature aft of the short nose section, so a flat plate (zero pressure gradient) approximation is appropriate. This is supported by the KC-135 Euler simulations performed by WL/FIMC. To include the most significant factors in transition, a few of the correlations described in White's Viscous Flow (Ref. 51) text were combined. Wazzan's method was used for a basic flat plate transition number including the effects of shape factor, and Reynolds number:

$$Re_{X_{tr}} = 10.^{(a+bH+cH+dH)} = 4.753 \times 10^{+6} \text{ for flat plate}$$

a, b, c, and d in the above are just coefficients (Ref. 51). Then to factor in the effect of freestream turbulence (T), Driest's method was selected:

$$\mathcal{F} = -1.+(1.+132,500.T^2)^{0.5} / 39.2T^2 / \lim_{T \to 0} D(T)$$

T=0.006 was selected to represent a "quiet" atmospheric day value and gives a Driest factor of 1/3, so $Re_{X_{tr}} = 1.584 \times 10^{+6}$, $Re_{X_{tr}}/L = 2.988 \times 10^{+6}$ ft^{-1} ($9.839 \times 10^{+6}$ m^{-1}) which from the laminar boundary layer growth equations gives a station of 0.53' or 6.36" aft of the nose curvature. Next Gibbing's 2-D lateral roughness criteria was employed:

$$Re_k = (u_c k)/\nu \cong 850$$

this implies $k_{tr} = 284.5\mu\text{ft} \cong 1/4$ mil. Panel gaps do not occur until farther back on the fuselage, so this transition mechanism is not a factor. Then Whitfield and Iannuzzi's 3-D protuberance criteria was utilized to check the effects of the rivets and antennas:

116

$$Re_k = (u(k)\ k)/v \cong 600$$

this implies $k_{tr} = 0.200$ mil. Within the 1/2 foot of the nose tip there are no such protuberances. Finally, Feindt's distributed roughness criteria was used to assess any possible effect of the paint. This method requires an equivalent sand-grain roughness height. From working tables, 320.μin (F-104/FTF Test Surfaces, Gunship camouflage gray polyurethane MIL-C-83286 color 36118 measurement) appeared to be the most realistic.

$$Re_k = (uk)/v \cong 120$$

This gives $Re_k = 79.67986$ so for the given conditions this will never be a factor. Taking all the above factors into consideration, the body was set fully turbulent in the analysis.

Table A1: Transition Models Considered

Method	Approach
2-Step Method of Granville	Find instability point based on White-Thwaites shape factor correlation. Then integrate Thwaites parameter until the location that exceeds the criteria
Michel's Method	Use Thwaites Method to compute Re_θ until it exceeds a power function of Re_x
eMalik 3-D Program	Descendent of COSAL, uses linear stability theory of compressible 3-D boundary layers to compute
Cebeci and Smith's Relation	Compute Re_θ until it exceeds a complex power function of Re_x
Wazzan's Method	Transition occurs when Re_x (H) crosses 10. to a cubic polynomial of H
Freestream Turbulence Plot	Wind tunnel data of Re_x as a function of T, used in simple factoring of results
Driest and Blumer's Method	Gives transition Re_x as a rational function of T
Dunham's Formula	Re_θ as a rational function with exponentials T, and Thwaites parameter
Mack's mod of e^9	N is a linear function of ln(T), for input to WT interpolation data or a linear stability code

Special Case Method	Approach
Gibbing's 2-D Lateral Roughness Criteria	A Re_k critical value
Whitfield and Iannuzzi's 3-D Protuberance Criteria	A Re_k critical value
Feindt Distributed Roughness Criteria	A Re_k critical value

APPENDIX B
Pressure Fluctuation Derivation

The derivation of the standard coefficient of pressure (C_p), as a function of local Mach number for isentropic flow (Ref. 52) was modified to show that the average turbulent kinetic energy (k) can be used to calculate the average pressure fluctuations (C_p''), for subsonic flow. The isentropic assumption breaks down for boundary layers and strong shocks. For the fine axisymmetric case, the entropy increase across the shock was small (Figure 65), therefore, the derivation was acceptable through this region. The boundary layer edge perturbations transmit through the boundary layer normal to the vehicle surface.

Each turbulence model differs more in turbulent quantities than in flow quantities (Ref. 38); however, the trends are the same. This result still has the pragmatic effect of directly comparing the pressure fluctuations of one design to another design. When combined with previous flight test information, buffeting levels can be inferred.

In the following derivation, the mass averaged mean quantities have a tilde overscore and the mass averaged fluctuation quantities are double primed.

Definition:

$$C_p = \frac{P - P_\infty}{0.5\varrho_\infty V_\infty^2} \approx \frac{\frac{P}{P_\infty} - 1}{0.5\gamma M_\infty^2} \tag{1}$$

Perfect Gas Assumption:

$$C_p T_\infty + \frac{V_\infty^2}{2} = C_p\left(\tilde{T} + T''\right) + \frac{\left(\tilde{V} + V''\right)^2}{2} \tag{2}$$

Isentropic Energy Equation: (Assuming T'' small)

$$T_\infty - \tilde{T} = \frac{\left(\tilde{V} + V''\right)^2 - V_\infty^2}{2C_p} \tag{3}$$

119

Collect like terms:

$$\frac{\tilde{T}}{T_\infty} = 1 - \left(\frac{\gamma - 1}{2}\right)M_\infty^2 \frac{\left(\tilde{V} + V''\right)^2 - V_\infty^2}{V_\infty^2} \tag{4}$$

$$\frac{P}{P_\infty} = \left(\frac{\tilde{T}}{T_\infty}\right)^{\frac{\gamma}{\gamma - 1}} \tag{5}$$

then at the boundary layer edge and beyond:

$$C_p = \frac{\left[1 - \left(\frac{\gamma-1}{2}\right)M_\infty^2\left[\left(\frac{\tilde{V}+V''}{V_\infty}\right)^2 - 1\right]\right]^{\frac{\gamma}{\gamma-1}} - 1}{0.5\gamma M_\infty^2} \tag{6}$$

Approximate the velocity perturbation as:

$$V'' = (2k)^{0.5} \tag{7}$$

Fluctuation = Instantaneous – Steady State Value:

$$C_p'' = C_p - \tilde{C}_P \tag{8}$$